AD-754 241

THE ELASTIC PLASTIC RESPONSE OF LONG SLENDER RODS SUBJECTED TO IMPULSIVE TYPE LOADINGS

Massey B. Valentine, et al

Air Force Armament Laboratory
Eglin Air Force Base, Florida

June 1972

AD754241

THE ELASTIC PLASTIC RESPONSE

OF

LONG SLENDER RODS

SUBJECTED TO IMPULSIVE TYPE LOADINGS

STRIKE PROCESS STUDIES BRANCH
WEAPON SYSTEMS ANALYSIS DIVISION

TECHNICAL REPORT AFATL-TR-72-124

JUNE 1972

NAT'...'AL TE HNICAL
INF ...AT ... FRVICE

AIR FORCE ARMAMENT LABORATORY

AIR FORCE SYSTEMS COMMAND & UNITED STATES AIR FORCE

141

EGLIN AIR FORCE BASE, FLORIDA

UNCLASSIFIED

DOCUMENT CONTROL DATA - R & D

(Security classification of title, body of abstract and indexing annotation must be entered when the overall report is classified)

1. ORIGINATING ACTIVITY *(Corporate author)*	2a. REPORT SECURITY CLASSIFICATION
Weapon Systems Analysis Division Air Force Armament Laboratory Eglin Air Force Base, Florida 32542	Unclassified
	2b. GROUP N/A

3. REPORT TITLE

THE ELASTIC PLASTIC RESPONSE OF LONG SLENDER RODS SUBJECTED TO IMPULSIVE TYPE LOADINGS

4. DESCRIPTIVE NOTES *(Type of report and inclusive dates)*

Final Report (January 1971 - May 1972)

5. AUTHOR(S) *(First name, middle initial, last name)*

Massey B. Valentine
Gerald D. Whitehouse

6. REPORT DATE	7a. TOTAL NO. OF PAGES	7b. NO. OF REFS
June 1972		9

8a. CONTRACT OR GRANT NO.	9a. ORIGINATOR'S REPORT NUMBER(S)
b. PROJECT NO	AFATL-TR-72-124
c.	9b. OTHER REPORT NO(S) *(Any other numbers that may be assigned this report)*
d.	

10. DISTRIBUTION STATEMENT

Approved for public release; distribution unlimited.

11. SUPPLEMENTARY NOTES	12. SPONSORING MILITARY ACTIVITY
Available in DDC	Air Force Armament Laboratory Air Force Systems Command Eglin Air Force Base, Florida

13. ABSTRACT

Experimental and analytical results are presented for the elastic plastic deformation of a slender rod subjected to impulsive loading that occurs during the impact of a rod against a rigid plate. Particular emphasis is given to the lateral or flexure buckling mode shapes that occur during the impact. The transient response and resulting deformation were recorded with the aid of high speed photography and flash X-rays. A frame-by-frame record of the impact phenomena gives the displacement of a particle on the rod and the plastic wave propagation position. Also presented are three distinct failure modes that result, dependent primarily upon impact geometry. For a pure orthogonal impact, a helical mode shape results. For a near orthogonal impact of approximately 1 to 3 degrees off the normal, all lateral motion is confined to a single plane resulting in a sinusoidal mode shape. Impacts from 4 to 6 degrees off the orthogonal result in a spiral mode shape. A derivation for the equations of motion is given, considering axial, lateral, and rotational inertia for the case where the lateral motion is confined to a single plane. The coupling between the differential equations of motion introduced by the nonlinear stress-strain relation is solved by allowing the axial equation to predominate. Two analytical techniques are presented for solving the differential equations of motion and material behavior. The Galerkin technique and the method of finite differences are used to obtain numerical solutions to the partial differential equations. A comparison between the analytical and experimental results is presented showing good agreement between the finite difference technique and the experimental results.

DD FORM 1473 (1 NOV)

- i -

14 KEY WORDS	LINK A		LINK B		LINK C	
	ROLE	WT	ROLE	WT	ROLE	WT
Slender Rods						
Elastic Plastic Deformation						
Flexure Buckling Mode Shape						
Wave Propagation						
Impact Phenomena						

The Elastic Plastic Response

of

Long Slender Rods

Subjected to Impulsive Type Loadings

Massey B. Valentine
Gerald D. Whitehouse

-iii-

FOREWORD

The work reported herein is a summary of both experimental and analytical work dealing with the elastic-plastic buckling of a slender rod impacting rigid plates. The experimental work was initiated during August 1970 and was completed during June 1971, with the analytical work starting during January 1971 and being completed during May 1972.

This is a jointly prepared report with Dr. Gerald D. Whitehouse of Louisiana State University serving as the advisor, and Mr. Massey B. Valentine of the Air Force Armament Laboratory, Strike Process Studies Branch, conducting most of the analyses. This report contains the results of a dissertation submitted by Mr. Valentine to the Mechanical Engineering Department at Louisiana State University.

The authors would like to express their appreciation to Mr. Leonard L. Wilson (DLRD) of the Air Force Armament Laboratory for supporting the experimental work described in this report. Appreciation is also acknowledged to Mr. Clyde E. Wallace (DLRD) of the Air Force Armament Laboratory for his assistance in conducting the test firings.

This technical report has been reviewed and is approved.

Thomas P. Christie
THOMAS P. CHRISTIE, Director
Weapon Systems Analysis Division

-IV-

TABLE OF CONTENTS

LIST OF FIGURES

LIST OF FIGURES (Continued)

LIST OF FIGURES (Continued)

LIST OF FIGURES (Continued)

LIST OF FIGURES (Concluded)

LIST OF TABLES

(The reverse of this page is blank)

LIST OF SYMBOLS

A   cross sectional area of rod

D   rod diameter

E   elastic modules of elasticity, Young's Modulus

e   equation residual or error used in Galerkin's method for lateral motion

F   force acting on rod

F_x force acting on rod along x coordinate

F_y force acting on rod along y coordinate

h   distance between nodal points for finite difference technique

I   moment of inertia of rod cross section about the neutral axis

I_1 moment of inertia of the rod cross section above the neutral axis

I_2 moment of inertia of the rod cross section below the neutral axis

K   parabola coefficient. A constant that is a function of the material

L   rod length

M   moment

N   order of system of differential equations

m   rod mass

P   axial force

R   equation residual used in Galerkin's method for axial motion

t   time

u   displacement of a particle along axial direction

$\dot{u}$ velocity of a particle along axial direction

$\ddot{u}$ acceleration of a particle along axial direction

v   rigid body rod velocity

W   total work produced by bending moment, axial force, applied forces, and inertia forces

LIST OF SYMBOLS (Concluded)

W_T work produced by inertia forces

x coordinate along axial direction

y displacement of a particle on rod in lateral direction

y_0 an amplitude factor

y_1 an amplitude factor

$\dot{y}$ velocity of a particle on rod in lateral direction

$\ddot{y}$ acceleration of a particle on rod in lateral direction

$\bar{y}_1$ static moment of rod cross section above neutral axis

$\bar{y}_2$ static moment of rod cross section below neutral axis

β plastic modulus or slope of stress-strain curve

γ assumed lateral displacement function for Galerkin's technique

δ symbol denoting virtual as used in virtual displacement denoted by δu, δy, $\delta \psi$

ε strain, $\frac{\partial u}{\partial x}$

ε_0 strain at yield

η_1 distance from neutral axis of rod to perimeter of upper section

η_2 distance from neutral axis of rod to perimeter of lower section

λ wavelength

ρ material density

σ stress in rod at neutral axis

σ_0 yield stress

τ time function

ϕ assumed axial displacement function for Galerkin's technique

ψ rotation angle of an element of rod, $\frac{\partial y}{\partial x}$

ω displacement function, used by Abrahamson

$[\ ]$ matrix notation

$\{\ \}$ vector notation

SECTION I

INTRODUCTION

An investigation was conducted into the elastic plastic response of
a slender rod subject to impulsive type loads, such as an impact of a
rod against a rigid plate. In this section, the work of other investi-
gators will first be considered, followed by a discussion of the appli-
cable work currently in progress. Then, to provide some background of
the rod impact problem, a short discussion of elastic and plastic stress
waves in a rod is presented followed by a brief statement of the problem
to be studied and solved.

1. PRIOR WORK

In the nineteenth century, Stokes, Poisson, Rayleigh, Kelvin, and others
developed the theory of elastic wave propagation in solids, primarily as an
extension of the theory of elasticity as applied to vibrating bodies.
During the first quarter of the twentieth century, the subject of wave
propagations was neglected; later, however, interest in the subject began
to increase. During the World War II era, the problem of plastic wave
propagation in solids was considered, with the first work being independ-
ently reported by Taylor, Von Karman, and Rakhmatulin. One of the first
investigations was concerned with longitudinal plastic waves propagating
along a rod. Von Karman and Rakhmatulin treated this problem with the
aid of Lagrangian coordinates, while Taylor used Eulerian coordinates.
The fundamental result of this work is that the wave velocity for long-
itudinal waves propagating along a bar is given by the relationship

$$C_0 = \sqrt{\beta/\rho} \tag{1}$$

where β is the slope of the stress-strain relationship (elastic or plastic),
and ρ is the material density.

1

More recently, elastic and plastic stress wave propagations, both longitudinal and flexural, have been studied by Abramson, Plass, and Ripperger (Reference 1). Also, Kolsky studied wave propagations and the analytical and experimental results are presented in Reference 2. Abramson's work was devoted to rods and beams, and the solution to an elastic plastic flexure wave propagation problem was presented for a beam assumed supported by a pin attached to a rigid base. A lateral impulsive load was applied to the beam, and the results showed that zones of plastic flow occurred only near the impact region and in a thin zone near the bending wave front. The remainder of the beam was found to behave elastically.

The most recent work dealing with flexure buckling due to impact loading was conducted by Abrahamson and Goodier (Reference 3), who obtained experimental results similar to those presented in this report. However, the results were only reported for lateral deformation confined to a single plane. Also the analytical work presented was limited to the prediction of the flexure wave wavelength.

During 1963, Grabarek and Ricchiazzi presented experimental results (Reference 4) for long rod impacts of mild steel rods impacting a finite target of like material. For some of the impacts, the impact velocity was such that penetration and perforation of the target plate occurred. At the lower striking velocities, the rod deformation of the impacted end was obtained as a function of time. Grabarek and Ricchiazzi presented the longitudinal plastic wave propagation velocities and the impact duration; however, due primarily to the length-to-diameter ratio of the rods, no flexure deformation was obtained from the experimental results.

A great deal of work has been conducted and is in progress using general purpose large scale elastic-plastic-hydrodynamic codes for solving

2

impact and impulsive loading problems. These large scale models employ the governing differential equations of motion, wave mechanics, and thermophysical properties of the materials, and are essentially outgrowths of work supported by the Atomic Energy Commission (Reference 5). These techniques have been successfully applied to predict the dynamic response of materials as applied to problems in penetration mechanics. Sedgwick (References 6 and 7) has also used the general purpose hydrodynamic codes to predict the deformation for short axi-symmetric cylinders, with ogive noses, penetrating target plates. The analytical model, CRAM, used by Sedgwick is very similar to the code described in Reference 5. These codes have met with little application outside of Government laboratories because of the large scale computers and extensive running times required for typical problem solutions.

Problems of symmetry dealing with the dynamic response of materials can be modeled quite accurately using the hydrodynamic codes; however, the results are no better than simple knowledge of the equation of state or stress-strain relation of the materials. This may also be generalized to include any theoretical technique used to predict the dynamic response of materials. In an effort to determine the dynamic stress-strain relation for several materials, Bell (Reference 8) used diffraction grating experimental techniques which permitted the optical determination of the stress-time detail of finite amplitude wave fronts propagating into crystalline solids whose prior history was known. These experimental diffraction grating studies lead to the discovery that a generalized stress-strain function results for the 27 crystalline solids considered. This stress-strain relation for the plastic region is parabolic and of the form

3

$$\sigma = K\sqrt{\varepsilon} \qquad\qquad\qquad (2)$$

where K is a constant that varies as a function of the material.

2. CURRENT WORK BEING PERFORMED

Current work is in progress to determine the dynamic response of materials subjected to impulsive loadings. Within the Air Force Armament Laboratory, analytical techniques are under development for predicting fracture and spall off the back side of target plates subjected to impact and other impulsive loads. A variation of the two-dimensional hydrodynamic code CRAM is being used for this purpose. Additional work is being performed in the area of dynamic crack propagation and stress wave propagations in ogive cylinders.

3. ELASTIC AND PLASTIC WAVES IN A ROD

Now, consider a rod of finite length that suddenly experiences an impact load. If the load is sufficient to compress the material beyond its elastic limit and the stress is maintained for a specified period, an elastic wave of compression will travel along the rod toward the other end. This elastic wave will be followed by a plastic wave which travels more slowly. When the compressive stress is removed, the resulting wave of unloading is a wave of tension and travels along the rod toward the free end. The elastic wave travels at a higher velocity than the plastic wave and when it overtakes the plastic wave, it reduces the amplitude of the plastic wave. When the elastic wave that is leading the plastic wave front reaches the free end of the rod, the elastic compression wave is reflected off the free end of the rod as an elastic wave of tension. When this reflected tensile wave interacts with the oncoming compressive plastic wave, the amplitude of the plastic wave is reduced, and unloading is accomplished. If the opposite end from the impacted end of the rod were fixed to a rigid body, the elastic compressive wave would reflect

4

off the fixed end as a compressive plastic wave. The fixed end situation is well represented by the driving of a spike in a hard media.

Figure 1 may be used to visualize the wave propagation. Along the front, OA, the stress is at yield. In the region OAB, the rod is in a plastic state. The region OBC is in the unloading region, and the elastic unloading relations apply. When the load is released, the tensile wave of unloading travels from the impacted end with the velocity of the elastic wave and meets the plastic wave at some region (as illustrated by 1 in Figure 1). The elastic wave bounces back and forth from the impacted end to the plastic wave, initiating a complicated unloading procedure. The time space domain in which permanent deformation occurs is the region of OAB.

Another type of wave motion is also present when a rod is impacted against a rigid surface. Flexure waves develop near the impacted end and propagate toward the free end of the rod at a velocity dependent upon the wavelength. The elastic flexure wave velocity, or phase velocity, is less than the logitudinal wave velocity and will never exceed the value 0.5764 $\sqrt{E/\rho}$ regardless of a wavelength. This important property will be discussed later and applied to the rod impact problem.

When the impact velocity of the rod is sufficiently large and the elastic limit of the material is exceeded, plastic buckling will occur. The plastic buckling that occurs due to the axial compressive stress will be confined within the axial plastic compression wave. This lateral motion that results in the plastic buckling can be induced by any one of several factors such as:

    a. A non-orthogonal impact.

    b. A bent rod.

5
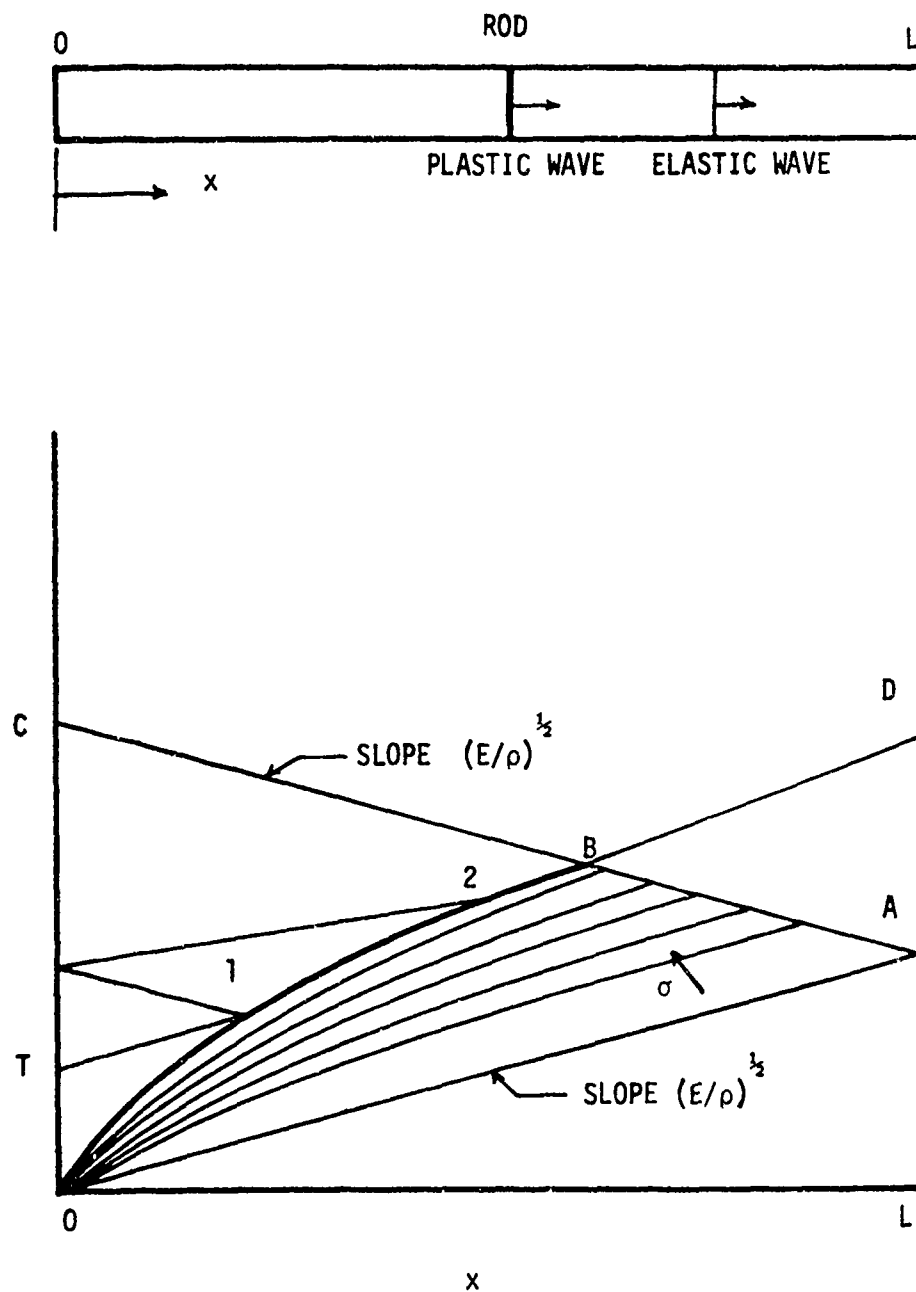
Figure 1. Time Position Domain of Elastic and Plastic Wave Fronts.

c. Non-isotropic material propert...s.

d. Stress pulses in rod induced by gun firing.

In the problem considered in this work, the lateral motion will be induced by a moment resulting from a small obliquity at impact.

4. STATEMENT OF THE PROBLEM

The objective of the work presented in this work is to predict the buckling mode shapes that occur when a slender rod impacts a rigid plate. Emphasis is placed on the lateral or flexure buckling, but in order to solve this problem, a solution of the axial deformation is necessary. Of course, analytical work is confirmed and validated only when supported by experimental work. An experimental program was conducted and is discussed in the following chapter.

SECTION II

EXPERIMENTAL RESULTS

A program was conducted to obtain an experimental data base for comparisons with analytical techniques for predicting the buckling mode shapes as a function of time for a slender rod impacting a rigid plate. The objectives of the experimental work were (a) to obtain the buckling mode shapes, (b) to relate the displacement of a particle on the rod as a function of time during the impact time, and (c) to obtain permanent strain profiles from the impacted rod. Hence, the major effort of the experimental work was directed toward capturing the rod motion during the impact sequence for observation of the buckling mode shapes during impact. These data were obtained with the use of high-speed photography and flash X-ray photography, the only experimental techniques available. Other techniques that could have been used to measure the displacement of a particle along a rod during impact include a split Hopkinson's Bar (Reference 2).

1. TEST PROCEDURES

One-quarter inch and 7/16 inch diameter aluminum rods (Type 6061 T-6) were purchased and tested using a tensile tester to determine if any anomalies existed and to determine if any variation existed in the yield of the material for each purchase lot. A sample test specimen was obtained from each 20 foot rod section and was pulled to failure on a tensile tester to establish a static stress-strain relation as well as the yield conditions. Type 6061 T-6 aluminum was chosen primarily for the invariance of the strain rate sensitivity property of the material.

The stress-strain relation obtained from the specimens pulled on the tensile tester is shown in Figure 2. On the figure, the stress-strain
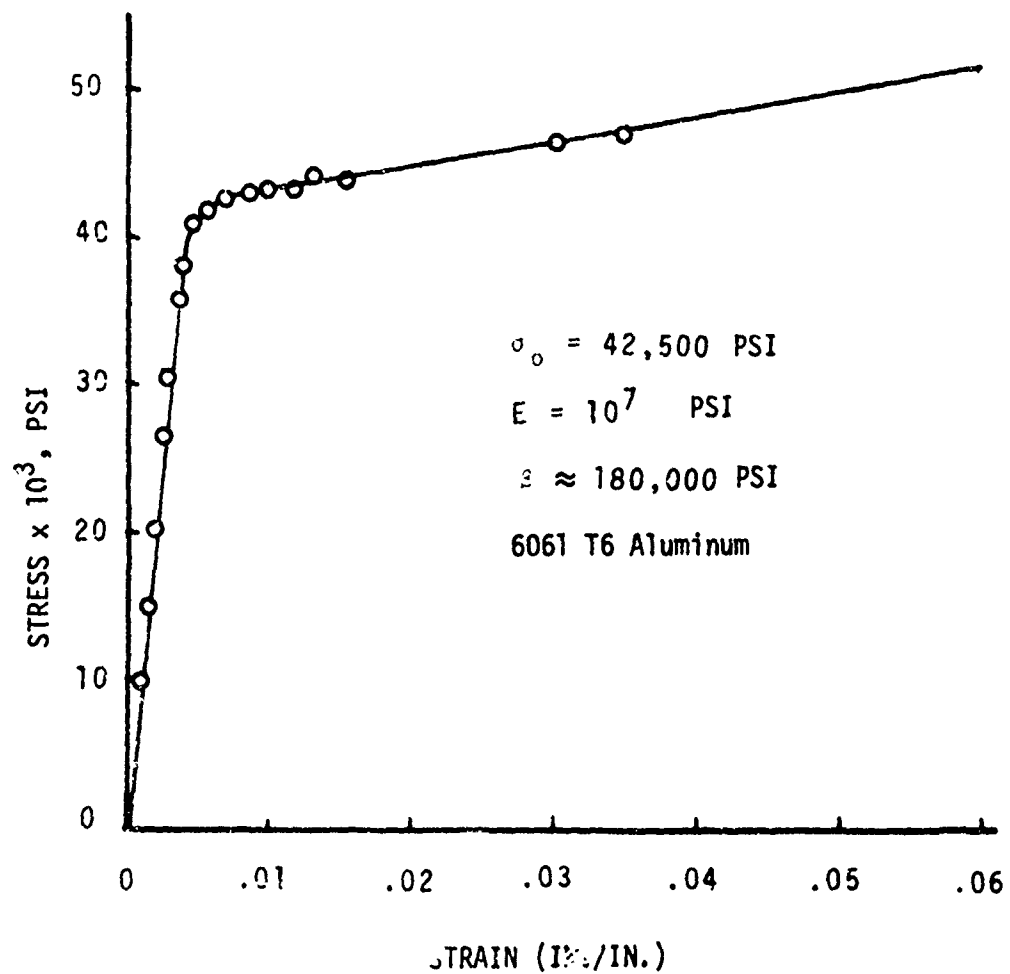
Figure 2. Static Stress-Strain Relation.

9

relation is essentially bilinear, with a linear elastic portion, a linear plastic section, and possibly some curvature near the yield point. A yield stress of 42,500 psi was established, and a slope in the plastic region of approximately 180,000 psi was determined.

Several of the aluminum rods (Figure 3) were scribed 80 lines per inch with a fine machine tool on a lathe. These reference marks were used to determine the plastic surface strain as a function of position along the rod. In addition to the scribed rods, some of the 7/16 inch diameter rods were anodized and then machined with circular rings at 1/4 inch intervals at a depth of 0.002 to 0.003 inch. These circular rings provided reference marks for tracking with high-speed cameras during the impact process.

Figure 4 shows the test setup and equipment. A powder chamber was used to fire the rods from a smooth bore Mannbarrel of caliber 0.30 for the 1/4 inch rods and of caliber 0.50 for the 7/16 inch rods. A plastic pusher plug and a Celotex®gas seal were used to push the rod along the barrel. The rod velocity was controlled by adjusting the amount and type of powder used during firing. Several types of cameras were used to capture the impact phenomena: A quarter-frame Nova camera with a nominal framing rate of 15,000 frames per second and a half-frame Fastex with a nominal framing rate of 15,000 frames per second. The cameras were placed orthogonal to each other as indicated in Figure 4. The orthogonal geometry was necessary to resolve the impact geometry. A B&W 192 framing camera was also used which has a variable framing rate ranging from 96,000 to 1,200,000 frames per second. Test samples utilizing the B&W camera were limited to four shots because of the light problems. An argon candle was utilized for the light source; however, the peak light intensity necessary to illuminate the rod sufficiently for exposure on the film was

10

Figure 3. Rod Section Scribed with 80 Lines Per Inch
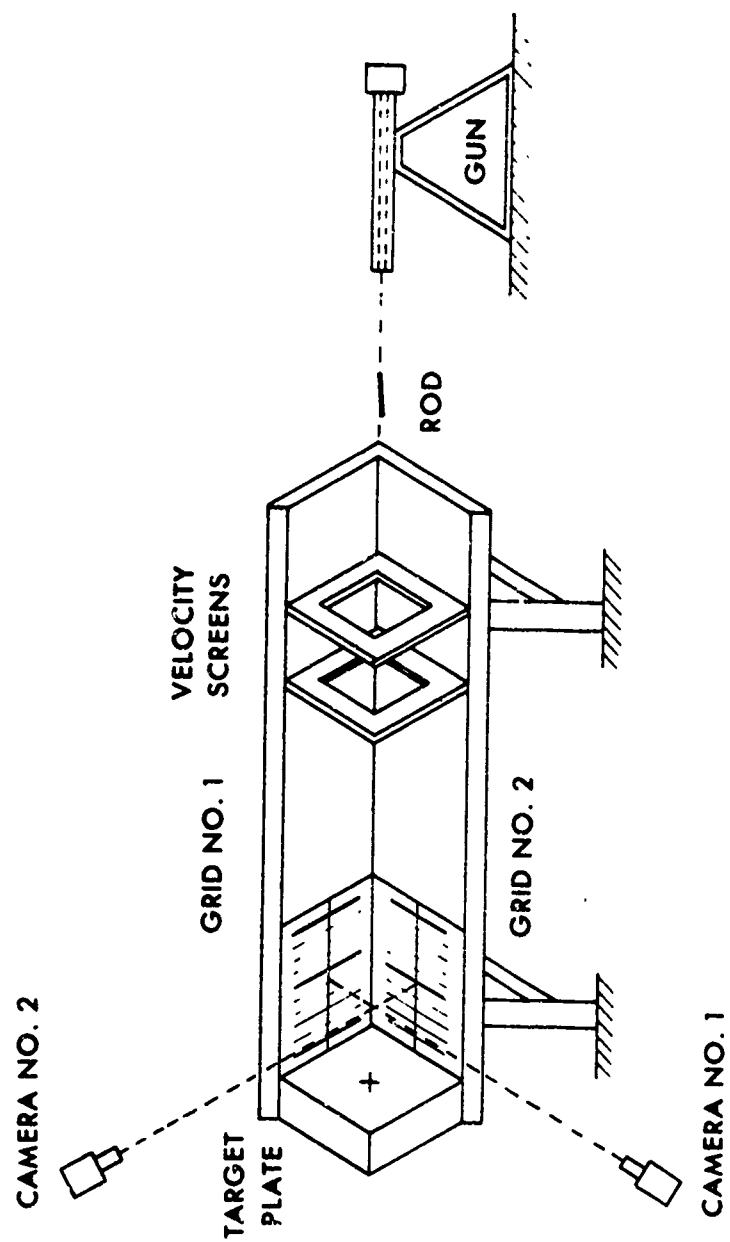
Figure 4. Schematic of Test Setup and Apparatus

12

not of sufficient duration to cover the impact duration. In addition, the film strip is limited to 72 frames. The limited film strip, coupled with the lighting problems, does not allow observation of the rod before, during, and after impact.

As shown on Figure 4, a grid was placed in the background of each camera's field of view to provide reference lines for the film reader in determining the displacement, impact angle, and velocity measurements. For those shots in which X-ray photography was desired, the grid (Figure 4) was covered with the X-ray film, and the X-ray tubes were placed in the positions occupied by the cameras.

Due to the time required for the cameras to reach the peak framing rate, a delay system was constructed using the camera signal to fire the gun. The gun was placed about 15 feet from the target plate to allow the angle of impact to vary from the orthogonal position so as to observe the effect of impact angle on rod deformation. Initially, some difficulty was experienced in stabilizing the rod during flight, but this was over-come by proper gun placement and using a pusher plug behind the rod.

2. FINAL MODE SHAPES

Figures 5, 6, and 7 show some typical final mode shapes obtained for 6, 12, and 18 inch rods that had impacted a rigid plate at various veloc-ities at or near orthogonal impact geometries. The impact geometry and velocity control the type of mode shape obtained from the tests. Three distinct types of mode shapes were obtained: sinusoidal, helical, and spiral.

For a pure orthogonal impact of sufficient velocity, a helical mode shape results (Figure 8). The words "of sufficient velocity" are signif-icant because some near orthogonal impacts at low velocity did not result in the helical mode shape. If the impact velocity had been higher, a

13
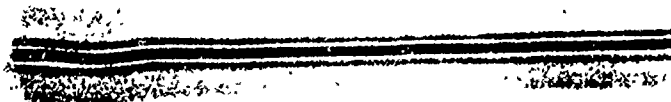
UNDEFORMED ROD

IMPACT VELOCITY 368 fps
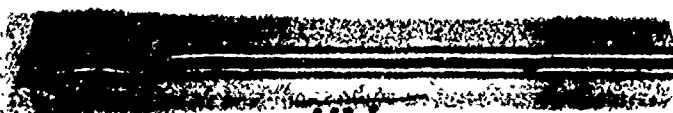
461 fps

819 fps

1217 fps

Figure 5. Final Mode Shapes for 6 Inch Aluminum Rods of 1/4 Inch Diameter

UNDEFORMED ROD

IMPACT VELOCITY 240 fps
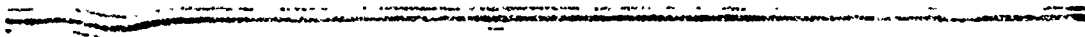
387 fps
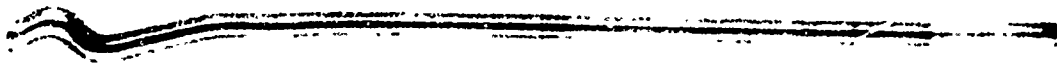
487 fps
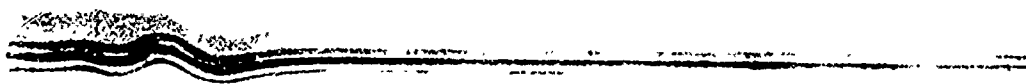
586 fps

Figure 6. Final Mode Shapes for 12 Inch Aluminum Rods of 1/4 Inch Diameter

15

Figure 7.   Final Mode Shapes for 18 Inch Aluminum Rods of 1/4 Inch Diameter

UNDEFORMED ROD

IMPACT VELOCITY   222 fps

450 fps

605 fps

16

Figure 8. Final Mode Shape for a 6 Inch Rod Having Impacted Orthogonally at 1006 fps Exhibiting a Helical Mode Shape

17

helix would probably have resulted. The neighborhood of the transition from the single plane deformation to the helical mode shape in terms of impact velocity is not known; however, the helical mode shape is believed to be velocity or stress dependent as well as geometry dependent.

For a near orthogonal impact of about 1 to 3 degrees off the orthogonal, a sinusoidal mode shape (Figure 9) results with the lateral deformation confined to a single plane. The 1 to 3 degree obliquity from the normal impact seems to be sufficient to impose a moment sufficiently large to prejudice the lateral motion to a single plane. Some of the impacts of high obliquity resulted in a hook shape with considerable bending of the rod near the impacted end. However, as shown on Figure 10, sinusoidal motion can be seen superimposed on the bending.

If the proper combinations of impact geometry and velocity occur, a spiral mode shape will result (Figure 11). Two spiral mode shapes were obtained with obliquity angles of about 4 degrees. These mode shapes were obtained for the 12-inch long rods of 1/4 inch diameter for impact velocities of 750 fps and 567 fps.

3. TRANSIENT MODE SHAPES

Figure 12 shows a single frame approximately 45 microseconds after impact taken from an impact sequence with the B&W 192 framing camera using a framing rate of 292,000 frames per second. The test specimen is a 7/16 inch diameter rod, 6 inches long, with machined rings on an anodized surface. One feature to observe from the impact (Figure 12) is the radial expansion of the rod near the impacted end; the longitudinal plastic wave (shown by the arrow) has advanced approximately 1.25 inches. Immediately behind the compression wave is the development of the plastic flexure wave that can be seen in the initial stages. The observed fact that the

18

Figure 9. Final Mode Shape for a 12 Inch Rod Exhibiting Sinusoidal Mode Shape with Lateral Deformation Confined to Single Plane

19

Figure 10. Final Mode Shape for a 12 Inch Rod of 7/16 Inch Diameter Having Impacted at Approximately 4 Degrees Obliquity with Sinusoidal Mode Shape Superimposed on Bending
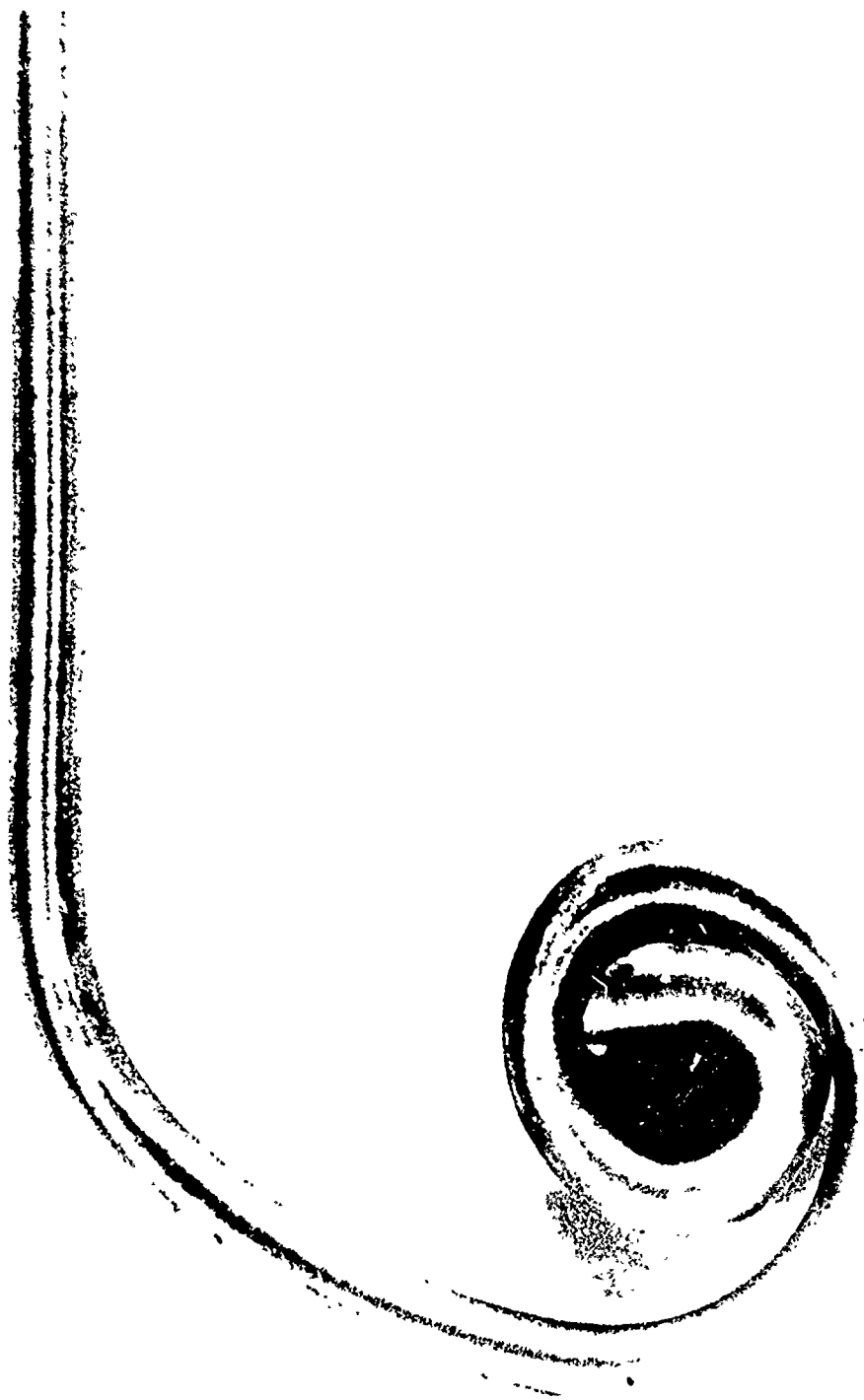
Figure 11. Spiral Mode Shape Obtained at 750 fps and 4 Degree Obliquity

PLASTIC WAVE POSITION
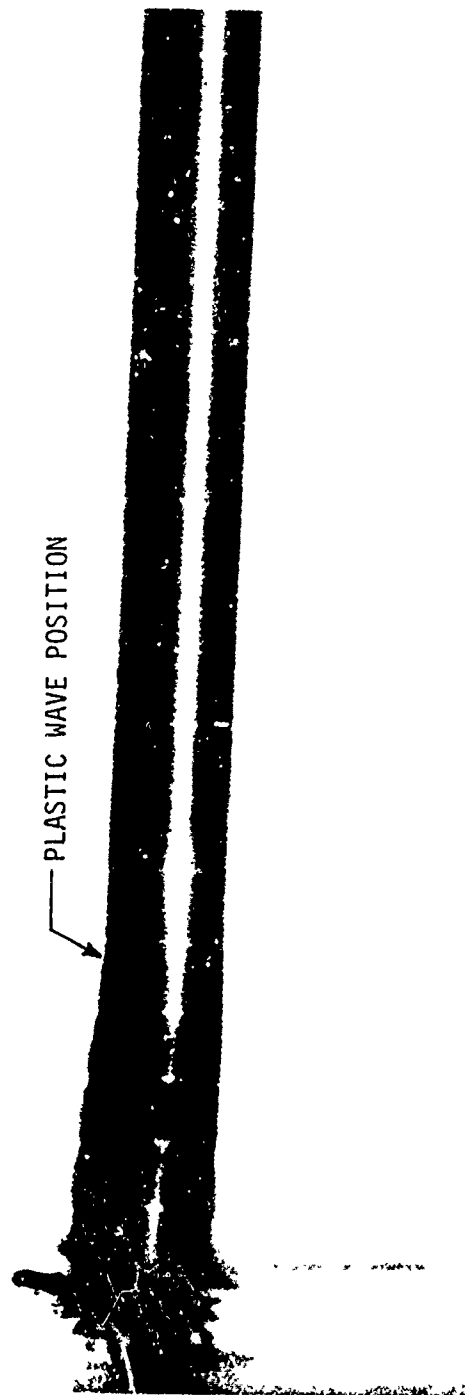
Figure 12. Impact of 6 Inch Rod of 7/16 Inch Diameter 45 Microseconds After Contact

22

plastic flexure wave is contained within the plastic compression wave allows a coupled system of differential equations of motion to be solved by letting the axial equation of motion control the material flow. Since the plastic compression wave dominates, the axial equation of motion is first solved to determine the state of strain at the neutral axis. Using the computed strain, the position on the stress-strain relation is then determined, and subsequently, the slope of the stress-strain relation is used in the lateral equation of motion for each time interval during the solution.

Figure 13 shows a high speed film sequence of a 12 inch long rod (1/4 inch diameter) impacting a rigid target plate at an impact velocity of 611 fps. The vertical lines on the film sequence are the reference marks placed in the background grid for the test setup shown in Figure 2. A white card was placed in the lower right portion of the grid to record the shot number, type rod, length, and other test conditions. The large cross or "x" on the left side of the film sequence is the desired impact point on the rigid target plate. For this particular sequence, the time between frames is 70.5 microseconds. The earlier frames show a sinusoidal mode shape developing, and after about 210 microseconds, the deformation becomes more gross due to the inertia of the rod and no longer resembles the familiar sinusoidal type observed earlier.

Figure 14 shows a flash X-ray photograph of the sinusoidal mode shape obtained during the impact. Superimposed shadows exhibiting transient mode shapes and deformations can be seen for three distinct time intervals during the impact.

Figure 15 shows a sequence of high-speed photographs exhibiting a helical mode shape for the orthogonal or near orthogonal impacts. This

23
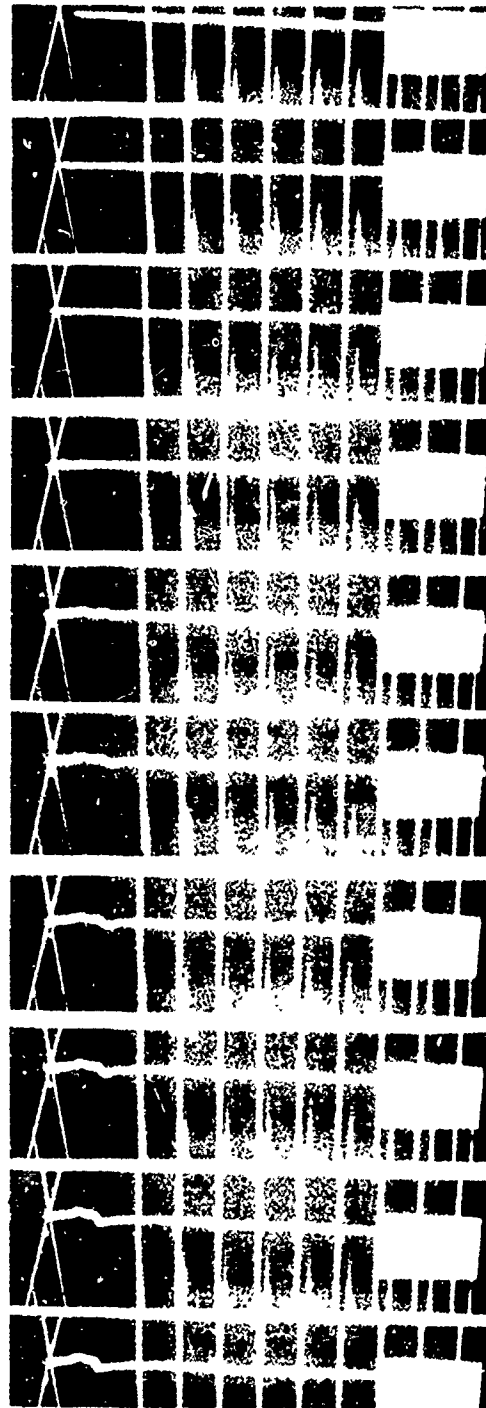
Figure 13. Sequence of High Speed Photographs Showing Predominate
Sinusoidal Mode Shape During Initial Frames, Developing
Later into More Grossly Deformed Shape. Time Between
Frames is 70.5 µsecond for 12 Inch Rod Impacting at
611 fps

24
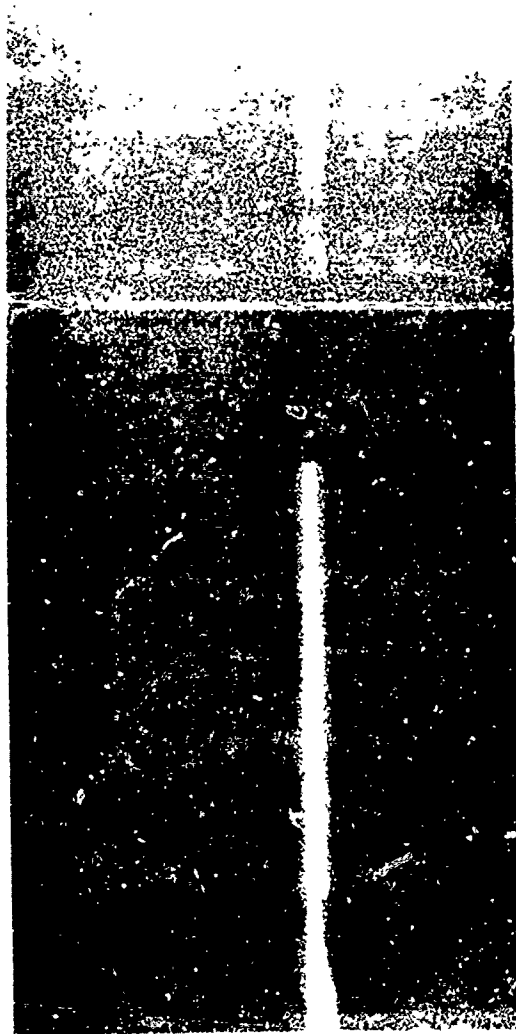
Figure 14. Sequence of Superimposed X-Ray Shadowgraphs of 6 Inch Rod Impacting at 697 fps

Figure 15. Sequence of Photographs Showing 12 Inch Rod Impacting at 632 fps and Exhibiting a Helical Mode Shape. Time Between Frames is 64 μseconds

26

particular 12 inch long rod impacted at 632 fps and near the orthogonal position.

A spiral mode shape occurs when the rod impacts at a obliquity angle of about 4 degrees as shown by the sequence of photographs on Figure 16. The impact velocity for this rod was 750 fps, and the time between frames is 65 microseconds.

4. ROD FAILURES

Rod breakup as typified by Figure 17 was experienced when the rod impact velocity was high (on the order of 850 fps and greater) and the angle of obliquity was greater than 2 degrees. A shear failure caused by the excessive axial inertial load is experienced immediately behind the first flexural wave. Table I gives the failure conditions obtained.

TABLE I

ROD FAILURE CONDITIONS FOR 1/4 INCH DIAMETER ALUMINUM RODS

Shot No.	Rod Length (Inches)	Impact Velocity (fps)	Obliquity Angle (Deg)
2	12	1008	4
3	18	895	4
4	18	1051	3
5	12	845	2
6	6	1000	3
16	6	1030	10

5. AXIAL DEFORMATION

The length of the rod has been obtained as a function of time by tracking the free end of the rod during the impact process with the aid of a film reader. These transient axial deformation data are shown in Figures 18, 19, and 20 for 6, 12, and 18 inch long rods (1/4 inch diameter). The instantaneous rod length L is normalized with the original

27
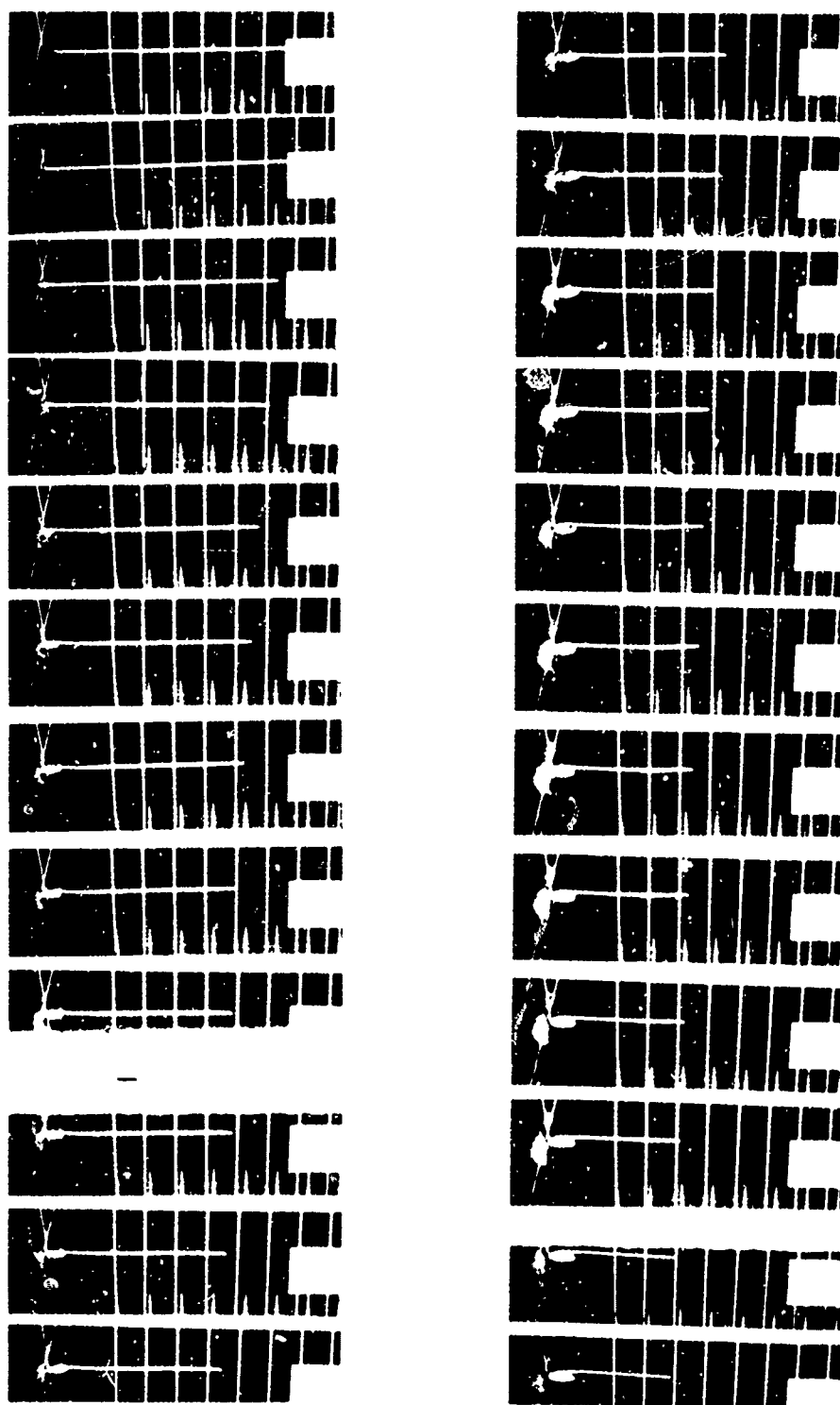
Figure 16.   Sequence of High Speed Photographs Showing 12 Inch Rod
             Impacting at 750 fps at a 4 Degree Obliquity. Time
             Between Frames is 65 μSeconds

Figure 16. Concluded

Figure 17. Example of Rod Breakup Caused by Combination of High Velocity Impact and Oblique Impact. Impact Occurred at 845 fps and 2 Degrees Obliquity.
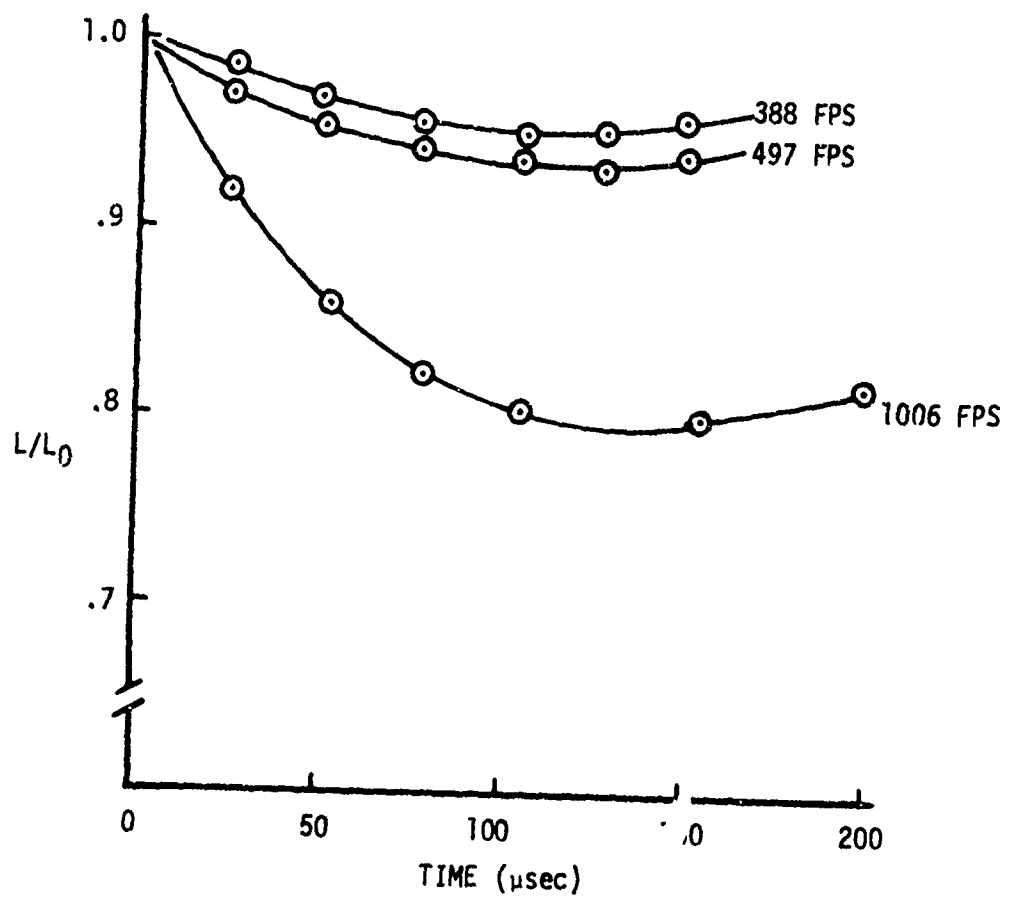
Figure 18. Instantaneous Rod Length for 6 Inch Rods of 1/4 Inch Diameter.
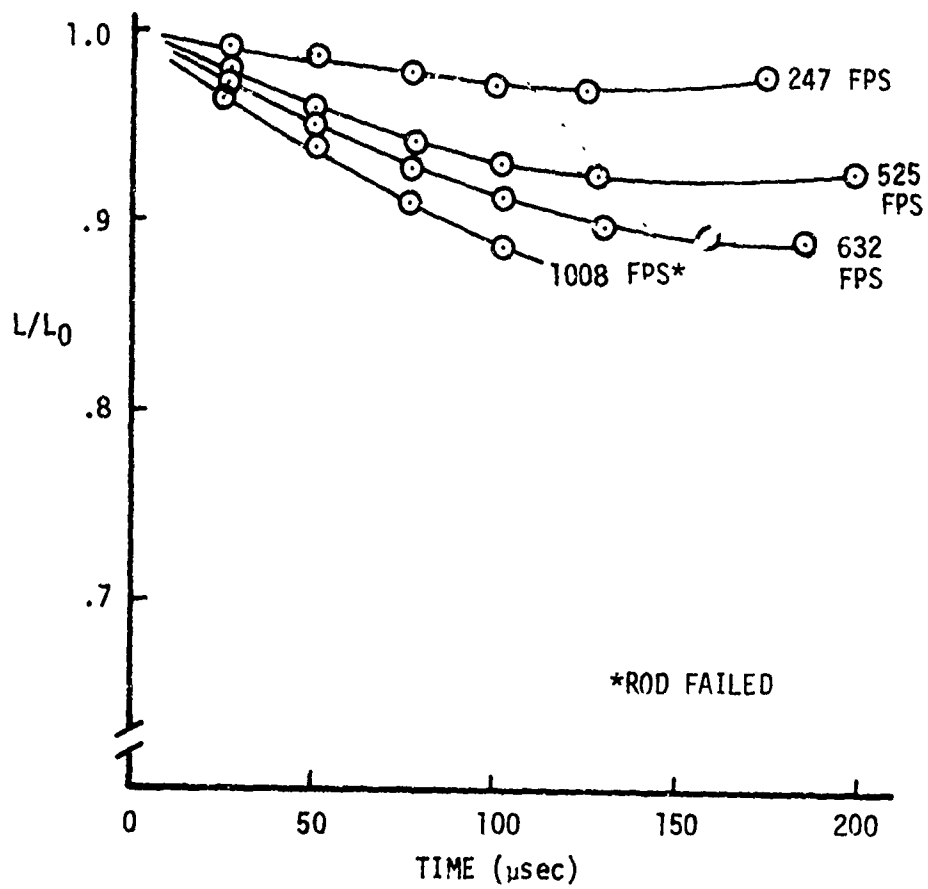
Figure 19. Instantaneous Rod Length for 12 Inch Rods of 1/4
Inch Diameter.

32
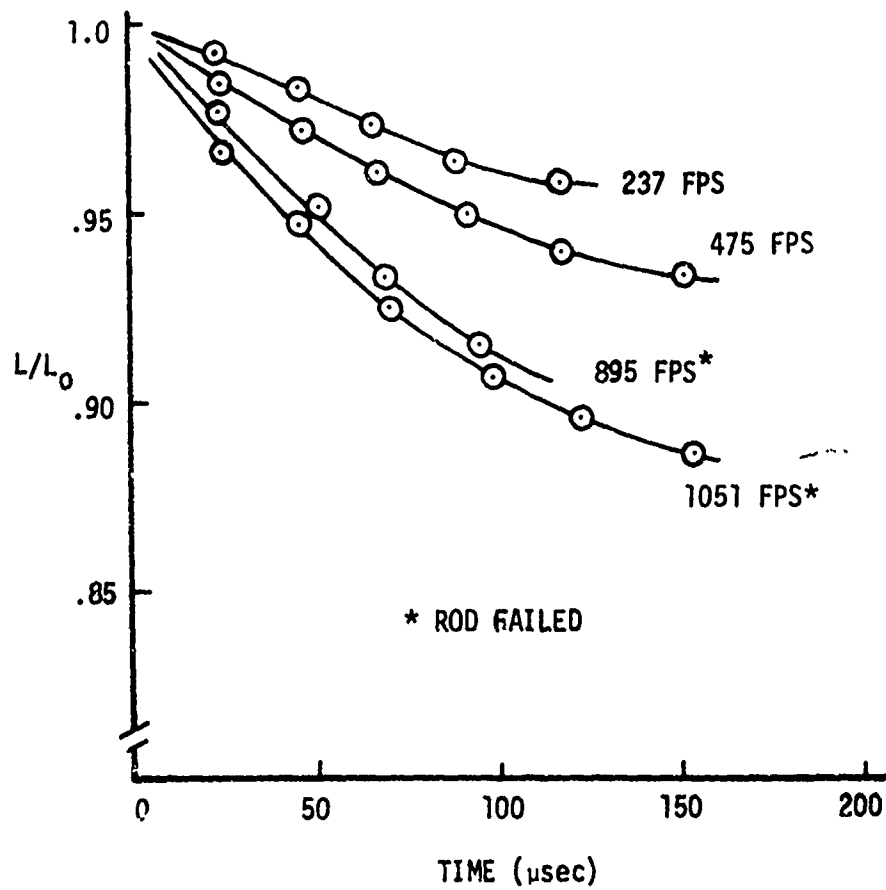
Figure 20. Instantaneous Rod Length for 18 Inch Rods of 1/4 Inch Diameter.

rod length L_0 and is plotted as a function of time. On Figure 18, the point of zero slope represents the time at which plastic deformation is arrested; note that the plastic deformation ceases after 75 to 100 microseconds, depending upon impact velocity. The theoretical plastic loading time is not easily computed, but if the loading time is assumed to be the time required for the elastic wave to reach the free end of the rod and return to the impacted end, this time is 61.5 microseconds. This compares to a loading time of 75 microseconds for a 388 fps impact velocity as determined by observing the film. Figure 18 also shows a slight increase in the rod length at the latter times, indicating the rod is bouncing back from the plate. Figures 19 and 20 show the length of the rod as a function of time for 12 and 18 inch rods, respectively. The plastic loading time is more difficult to obtain from Figures 19 and 20, but for the 12 inch rods, this time ranges from 110 microseconds to 155 microseconds, depending upon impact velocity.

In most instances, the exact time at which impact occurred is difficult to obtain. Most frequently, the impact occurred between frames, and in order to establish the impact time, the terminal velocity and framing rates must be known. Hence, some error is introduced in establishing the time at which impact occurs, as well as errors introduced by the position of the particle from the film reader. Indications are that the accuracy of the film reader is approximately 0.02 inch; however, due to the motion of the particular particle under consideration, the resolution of the particle on the film introduces another error.

The permanent axial deformation for all the 1/4 inch diameter aluminum rods fired is given in Figure 21. Note that beyond an impact velocity of approximately 670 fps the curve should be restricted to the 6 inch rod impacts.

34
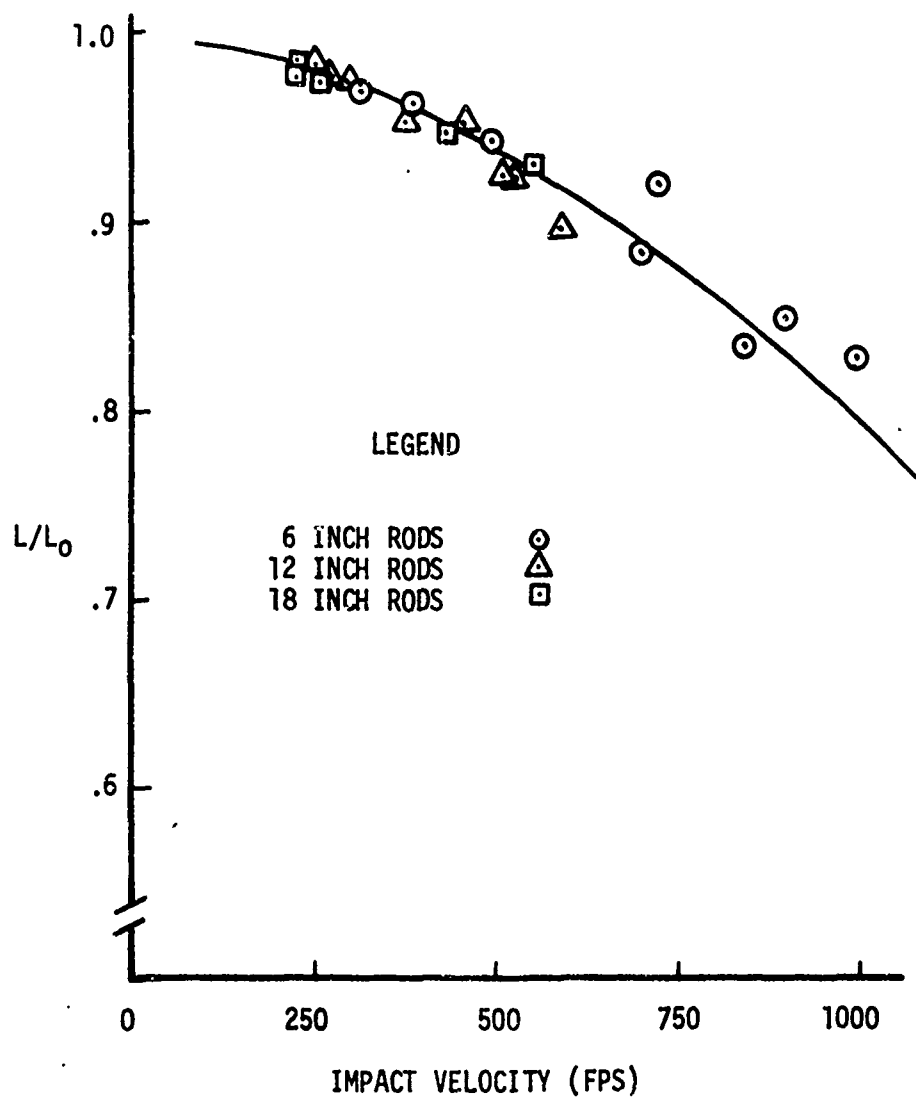
Figure 21. Permanent Axial Plastic Deformation as a Function
of Impact Velocity of 1/4 Inch Diameter Rods.

6. PLASTIC WAVE PROPAGATION

Figures 22, 23, and 24 show the longitudinal plastic wave position as a function of time for the 1/4 inch diameter aluminum rods. From the film, frame-by-frame measurements were made of the longitudinal wave front as it propagates toward the free end. With the aid of a film reader, a radial plastic deformation is evident during the initial stage of the impact. The flexure buckling occurs later in the impact and appears to be contained within the axial or longitudinal plastic front. This deformation was previously seen in Figure 12 where the plastic wave propagates up the rod. The plastic wave velocity may be obtained as the slopes of the curves presented in Figures 22, 23 and 24. Figure 22 shows that the wave velocity is higher for the lower impact velocities, particularly during the initial phases of the impact. This phenomenon can be due to one of two factors; (1) the material could be strain rate sensitive or other than bilinear (perhaps parabolic as suggested by Bell in Reference 8), thus denoting a change in the stress-strain slope as a function of strain rate or (2) the rod material could merely be stacking at the impacted end for the higher impact velocities. The latter factor seems to be more plausible since the plastic wave front was measured from the plate. Another important observation indicates the plastic wave front velocity appears to be independent of the rod length during the initial impact times, but is a function of the rod impact velocity.

7. AXIAL SURFACE STRAINS

Figures 25 and 26 show the permanent plastic strain measured axially on 6 and 12 inch aluminum rods, respectively. Prior to firing the rod, lines were scribed at 80 lines per inch along the rod. With the aid of an optical comparator using a magnification of 20 power, the surface strain

36
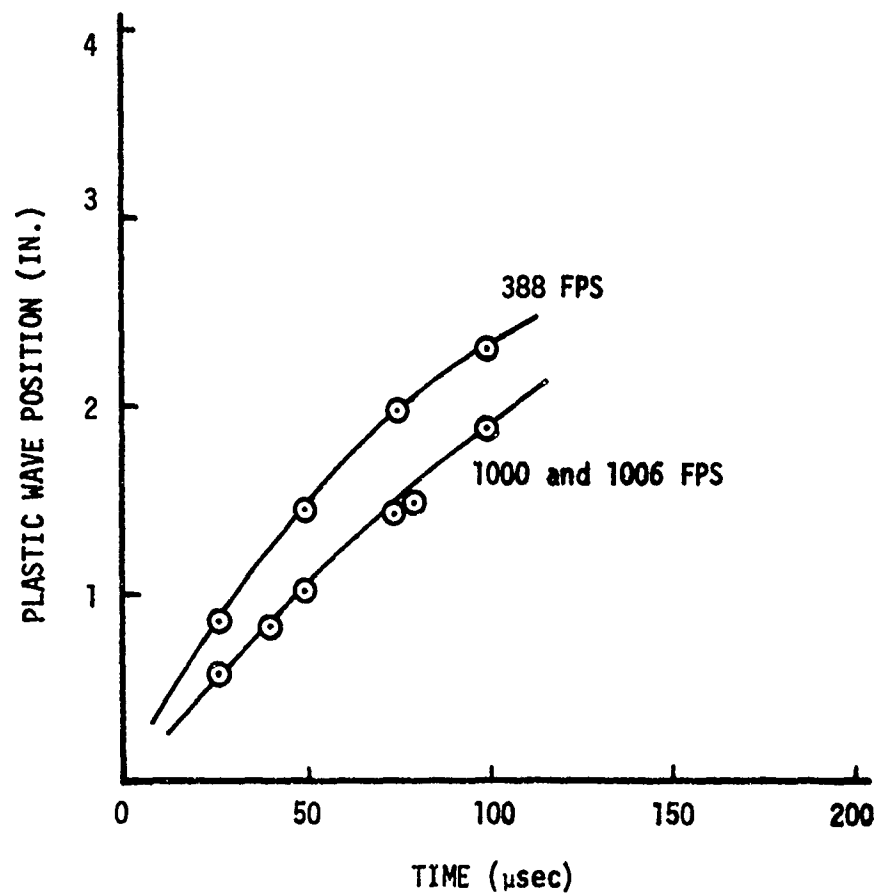
Figure 22.   Plastic Wave Position for 6 Inch Rods of 1/4
Inch Diameter.
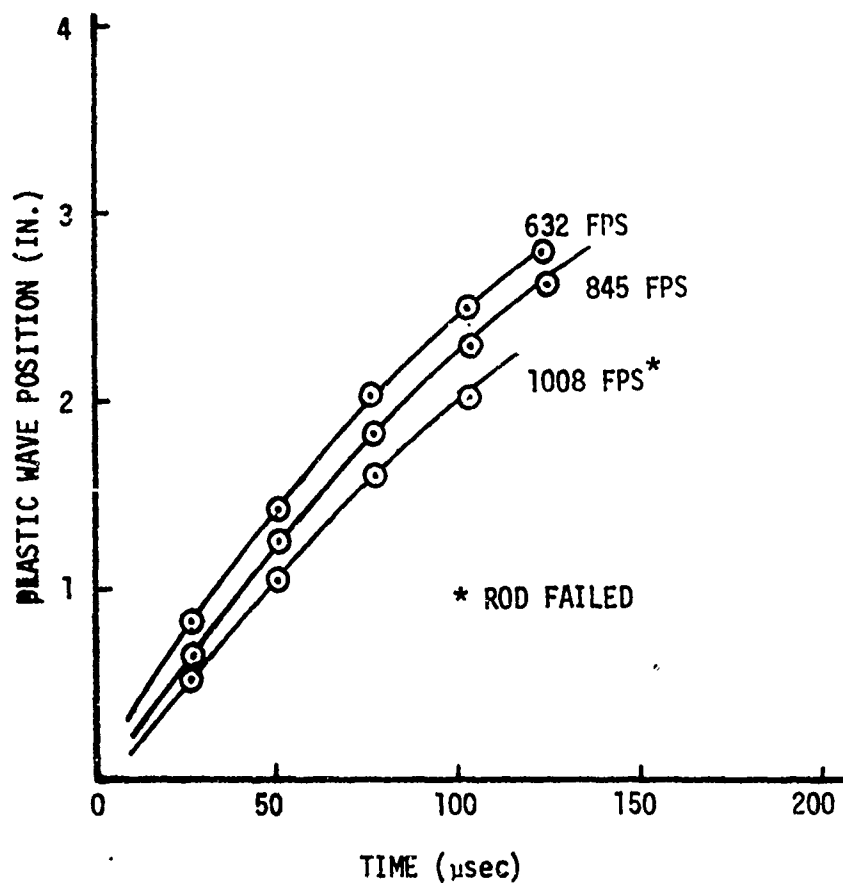
Figure 23. Plastic Wave Position for 12 Inch Rods of 1/4
Inch Diameter.
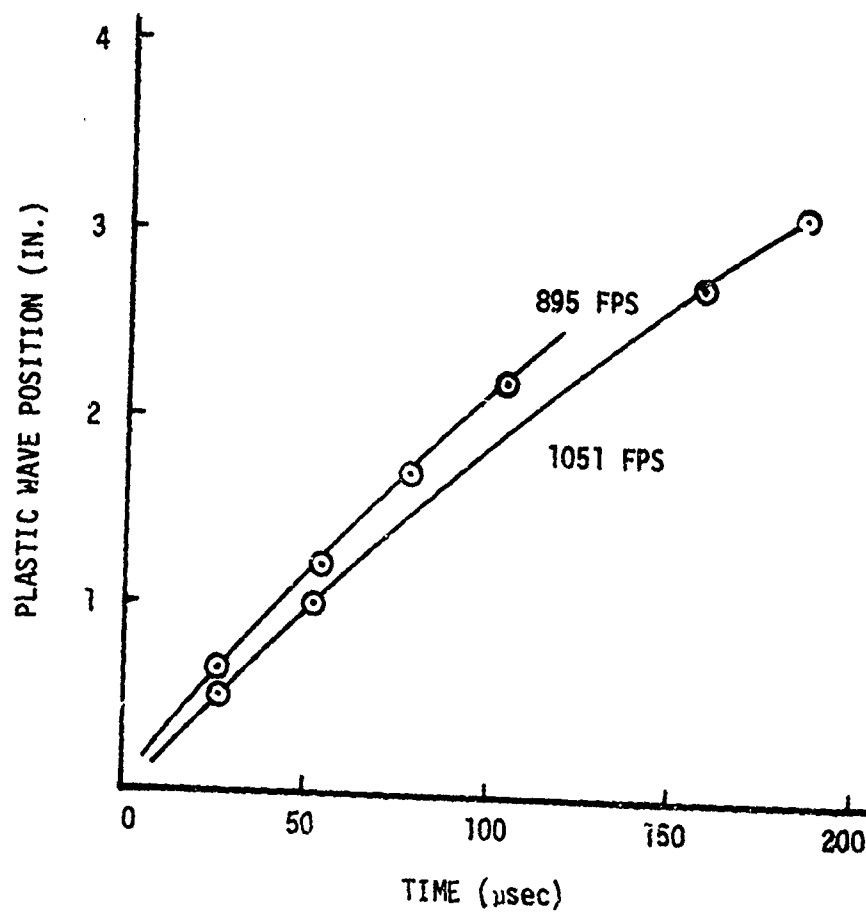
Figure 24. Plastic Wave Position for 18 Inch Rods of 1/4 Inch Diameter.
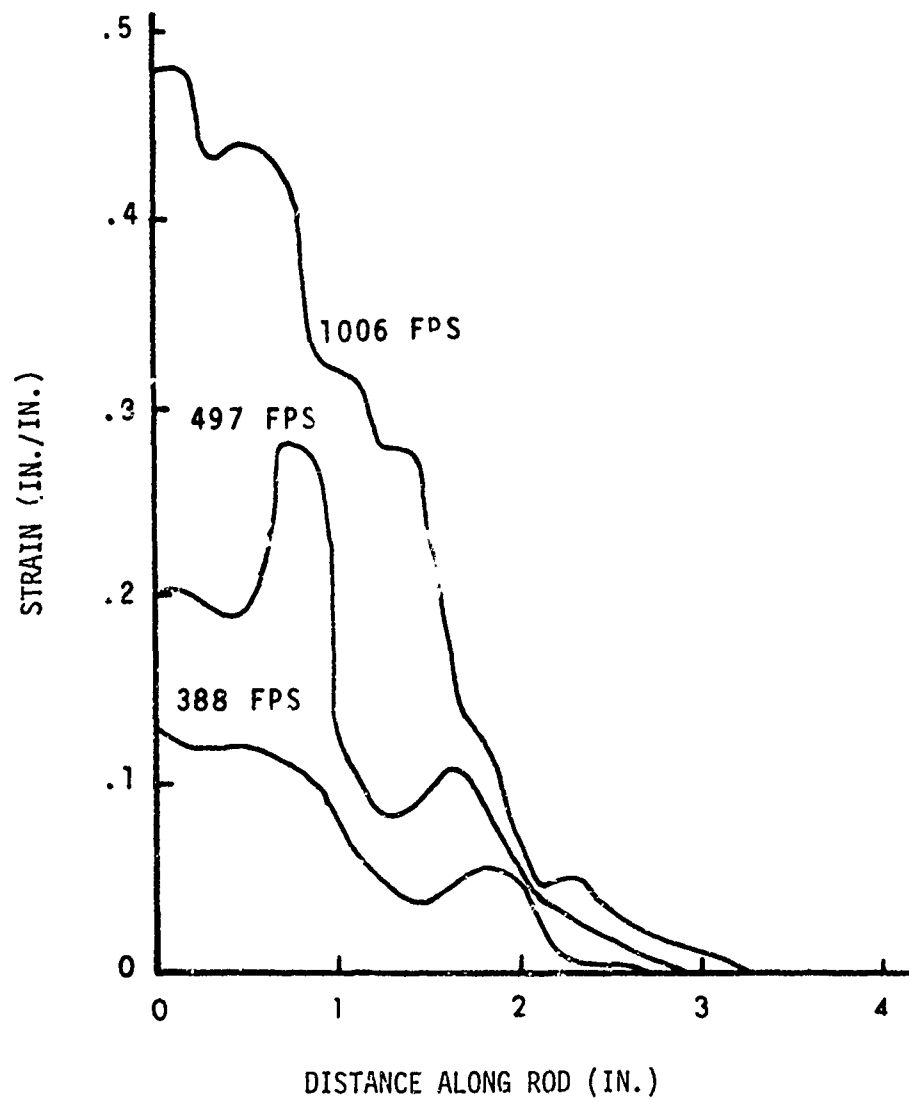
Figure 25. Axial Surface Strains for 6 Inch Rods of 1/4 Inch Diameter.
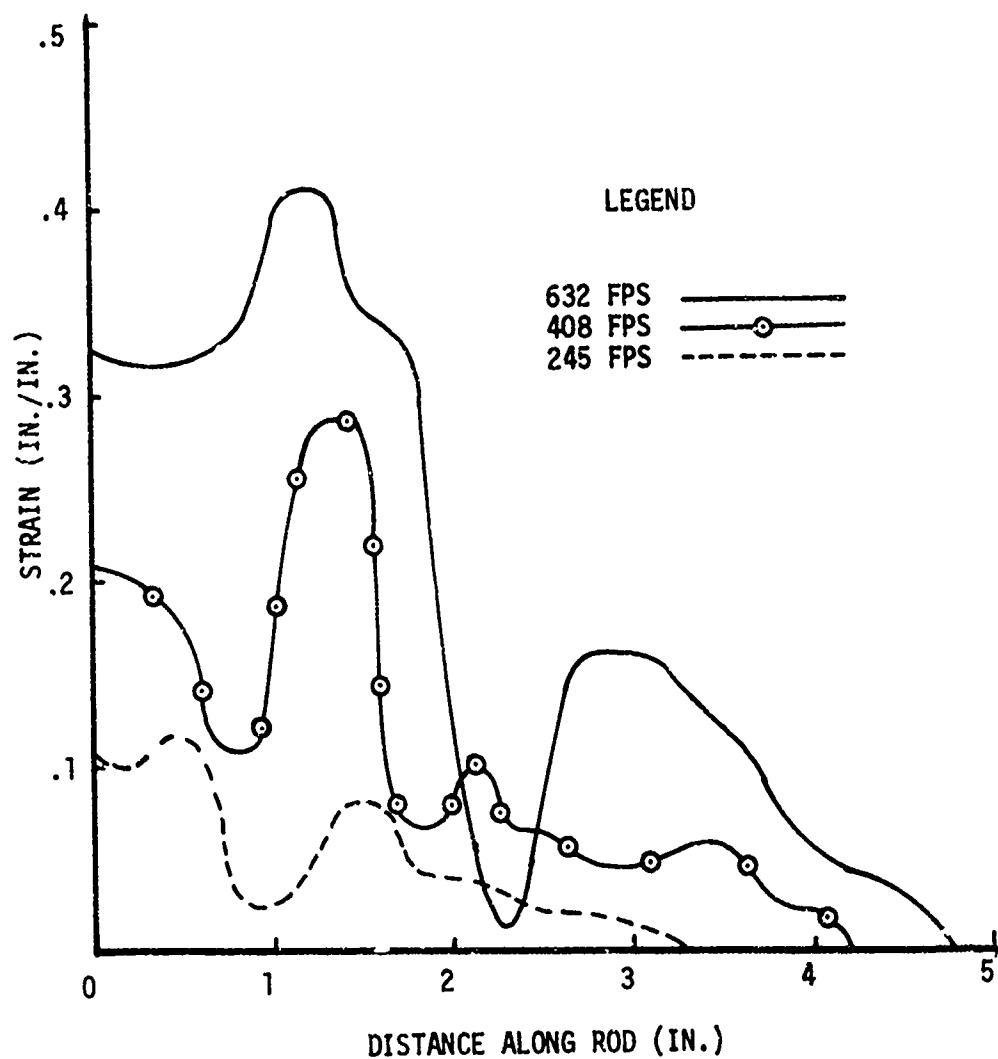
Figure 26. Axial Surface Strains for 12 Inch Rods of 1/4 Inch Diameter

was measured along each rod. Using 20-line increments, corresponding to 0.25 inches for the undeformed rod, the rod length per 20-line increment was measured and the deformation was determined per each 20-line increment.

Initially, the most impressive feature is the gross variations of strain along the rod. However, it should be realized that the surface strain in a single axial direction has been measured. If the rod were rotated about its neutral axis and the strains were recorded by several axial readings and averaged, a smoother curve would result; this will be shown later when the average strain at the neutral axis is compared to the analytical results. Actually, the curves shown in Figures 25 and 26 show a large amount of quantitative information about the rod. The peaks, or points of relative maximum strain, occur where the axial compressive strain due to the axial inertia load is reinforced by the bending moment produced by the flexural wave. The points of relative minimum strain represent the peak of the mode shape where the compression due to the axial inertia is relieved by the tensile bending moment produced by the flexural wave. The intersection of the strain curves with the axis gives the arrest position of the plastic wave.

8. SUMMARY OF EXPERIMENTAL RESULTS

The experimental work conducted provided the following conclusions:

(1) High-speed photography is the most effective method of obtaining dynamic data concerning the transient mode shapes, plastic wave propagation velocities, and displacements.

(2) The associated flash X-ray technique provides an excellent technique for observing the deformation at a maximum of three discrete time intervals. But the technique does not provide continuous observation over the entire impact duration.

42

(3) Impact geometry plays an important role in determining the deformation mode shapes. An orthogonal impact with impact velocities greater than approximately 750 fps yields a helical mode shape. If there is a slight obliquity of 1 to 3 degrees at impact, the lateral deformation is confined to a single plane with a sinusodal type mode shape resulting. For oblique impacts on the order of 3 to 6 degrees, a spiral mode shape can occur for a rod having a high length-to-diameter ratio and for impact velocities greater than approximately 500 fps.

SECTION III

DEVELOPMENT OF THE EQUATIONS OF MOTION AND MATERIAL BEHAVIOR

In this section, the principle of virtual work will be used to develop the equations of motion to include axial, lateral, and rotary inertia for a material whose stress-strain relation is nonlinear. Acting on the rod is an axial force P and a bending moment M. Figure 27 illustrates the forces and moments acting on a differential element of the rod along with the displacements and the rotation of the element.

1. THE PRINCIPLE OF VIRTUAL WORK

Consider a system which has been reduced to a finite number of degrees of freedom. Further assume the applied forces vary continuously with system displacements and that all differential equations describing the system constraints can be integrated. For such a system, the principle of virtual work states that a necessary and sufficient condition for equilibrium is:

$$\delta W = 0. \tag{3}$$

The principle of virtual work ($\delta W = 0$) yields the conclusion that, for a mechanical system to be in equilibrium, the components of the generalized force must vanish.

Referring to Figure 27, consider a displacement u in the axial direction, a displacement y in the lateral direction, and a rotation of the differential element through an angle ψ. For a differential element dx, the differential work produced by the bending moment M and the axial force P is:

$$dW = M \, d\psi + P \, du \tag{4}$$

44
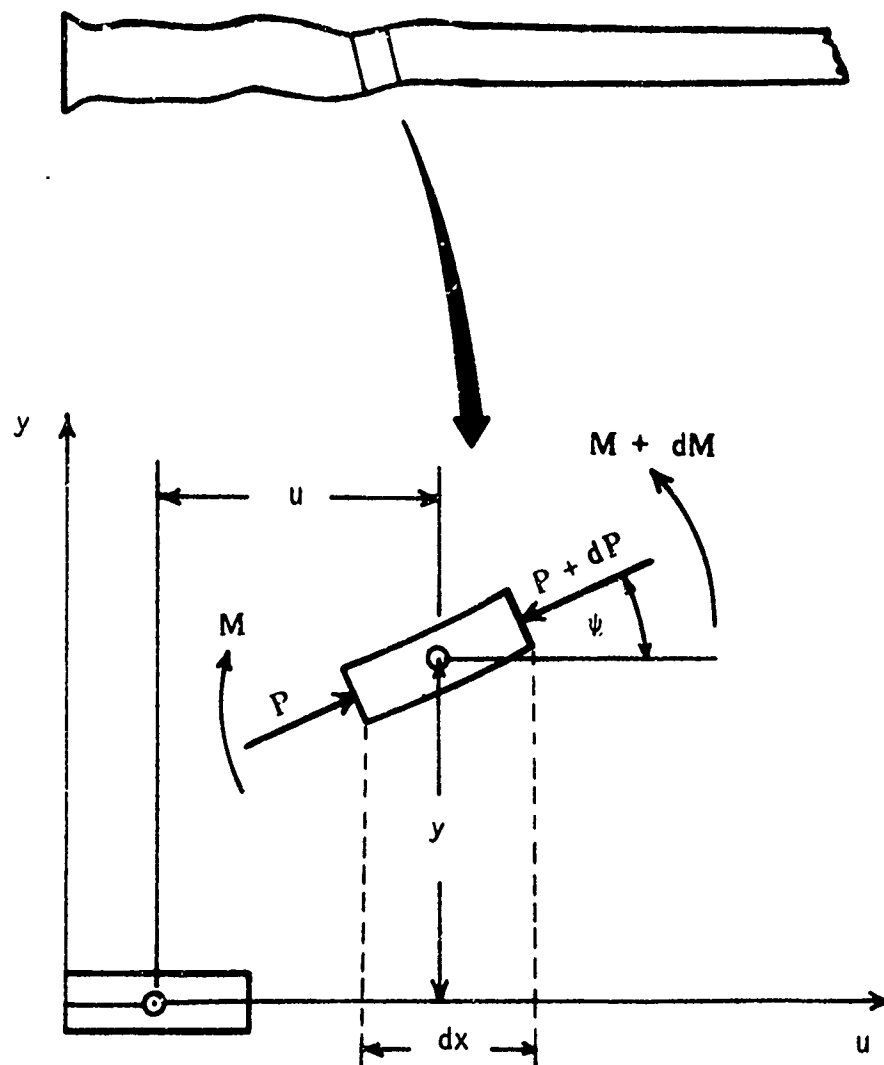
Figure 27.   Differential Element of Rod Showing Displacements,
Forces, and Moment

The work produced by the inertia forces is:

$$dW_T = \rho A\left(\frac{\partial^2 u}{\partial t^2} u + \frac{\partial^2 y}{\partial t^2} y\right) + \rho I \frac{\partial^2 \psi}{\partial t^2} \psi \tag{5}$$

The work produced by the external forces that are assumed to act on the impacted end of the rod is:

$$W_F = - F_y \dot{y}(0) - F_x u(0) \tag{6}$$

Integrating over the total length of the rod, the energy expression becomes:

$$W = \int_0^L \left(M\frac{\partial \psi}{\partial x} + P\frac{\partial u}{\partial x} + \rho A\left(\frac{\partial^2 u}{\partial t^2} u + \frac{\partial^2 y}{\partial t^2} y\right)\right) dx +$$

$$\int_0^L \rho I \frac{\partial^2 \psi}{\partial t^2}\psi \, dx - F_y \, y(0) - F_x \, u(0) \tag{7}$$

Now, denoting the derivatives with respect to x as primes and considering virtual displacements, the following expression results:

$$\delta W = \int_0^L \left[M\delta\psi' + P\delta u' + \rho A\left(\frac{\partial^2 y}{\partial t^2} \delta y + \frac{\partial^2 u}{\partial t^2} \delta u\right)\right] dx +$$

$$\int_0^L \left[\rho I \frac{\partial^2 \psi}{\partial t^2}\delta\psi\right] dx - F_y \, \delta y(0) - F_x \, \delta u(0) \tag{8}$$

Intergrating Equation (8) and applying the principle $\delta W = 0$, the following expression for the virtual work results:

$$\delta W = M\delta y'(L) - M\delta y'(0) + \left(\frac{\partial M}{\partial x} - \rho I \frac{\partial^3 y}{\partial t^2 \partial x} + F_y\right) \delta y(0) +$$

$$\left(- \frac{\partial M}{\partial x} + \rho I \frac{\partial^3 y}{\partial t^2 \partial x}\right) \delta y(L) + (P - F_x) \, \delta u(0) + P \, \delta u(L) +$$

$$\left[\int_0^L \left(\frac{\partial^2 M}{\partial x^2} - \rho I \frac{\partial^4 y}{\partial t^2 \partial x^2} + \rho A \frac{\partial^2 y}{\partial t^2}\right) dx\right] \delta y +$$

46

$$\left[\int_0^L \left(\rho A \frac{\partial^2 u}{\partial t^2} - \frac{\partial P}{\partial x} \right) dx \right] \delta u = 0 \tag{9}$$

For the expression in Equation (9), the components of the generalized forces must vanish independently, resulting in the equations of motion and the boundary conditions.

In the interior of the rod, the following equations of motion hold:

$$\frac{\partial^2 M}{\partial x^2} - \rho I \frac{\partial^4 y}{\partial t^2 \partial x^2} + \rho A \frac{\partial^2 y}{\partial t^2} = 0 \tag{10}$$

$$\rho A \frac{\partial^2 u}{\partial t^2} - \frac{\partial P}{\partial x} = 0 \tag{11}$$

At the boundary $x = 0$, the impacted end, the boundary conditions are:

$$M = 0 \tag{12}$$

$$P - F_x = 0 \tag{13}$$

$$\frac{\partial M}{\partial x} - \rho I \frac{\partial^3 y}{\partial t^2 \partial x} + F_y = 0 \tag{14}$$

At the boundary $x = L$, the free end, the boundary conditions are:

$$M = 0 \tag{15}$$

$$P = 0 \tag{16}$$

$$\frac{\partial M}{\partial x} - \rho I \frac{\partial^3 y}{\partial t^2 \partial x} = 0 \tag{17}$$

Note that in Equations (10) through (17), the equations of motion and boundary conditions for the rod, that the bending moment M and the axial force P appear. The boundary conditions are those of a free rod and allow deflections and rotations at both the impacted end and

47

the free end. The moment vanishes at both boundaries. At the impacted
end, the axial force in the rod is balanced by the axial forcing function,
and the rotational forces are balanced by the lateral forcing function.
At the free end both the axial and rotational forces vanish.

2. RELATING THE AXIAL FORCE P TO A DEFLECTION u

The relating of the axial force in the rod to an axial deflection
is quite straightforward. Since a bilinear stress-strain relation was
obtained from the tensile tests, the relation shown in Figure 2 will be
utilized. However, the theory developed herein is easily applied to
any stress-strain relation. Consider the equations for the stress-strain
relation as follows:

$$\sigma = E\varepsilon \qquad \text{for } \varepsilon < \varepsilon_0 \qquad (18)$$

$$\sigma = E\varepsilon_0 + \beta(\varepsilon - \varepsilon_0) \qquad \text{for } \varepsilon \geq \varepsilon_0 \qquad (19)$$

By definition $\varepsilon = \frac{\partial u}{\partial x}$ and since $\sigma = P/A$ the following relations
result:

$$P = AE \frac{\partial u}{\partial x} \qquad \text{for } \varepsilon < \varepsilon_0 \qquad (20)$$

$$P = [E\varepsilon_0 + \beta (\frac{\partial u}{\partial x} - \varepsilon_0)] A \qquad \text{for } \varepsilon \geq \varepsilon_0 \qquad (21)$$

Also, the following derivatives hold:

$$\frac{\partial P}{\partial x} = AE \frac{\partial^2 u}{\partial x^2} \qquad \text{for } \varepsilon < \varepsilon_0 \qquad (22)$$

$$\frac{\partial P}{\partial x} = A\beta \frac{\partial^2 u}{\partial x^2} \qquad \text{for } \varepsilon \geq \varepsilon_0 \qquad (23)$$

Equations (22) and (23) differ only by the relations E and β, the
slopes of the elastic and plastic portions of the stress-strain

48

relation. Equation (23) can be taken as the general expression relating the axial force to an axial deflection; in which case, β merely becomes the slope of the stress-strain relation for both elastic or plastic deformation and for any general stress-strain relation.

3. RELATING THE MOMENT TO A LATERAL DEFLECTION y

To relate the bending moment M to a lateral deflection y, a bilinear stress-strain relation is employed. In addition to the stress-strain relation, the assumption is made that the plastic buckling occurs within the axial plastic compression waves. Assuming the rod has failed due to the axial plastic compression, now consider the superimposition of a bending moment. Figure 28 shows a cross-section and a stress profile of the rod. Also shown is the compressive stress σ_c at the neutral axis which is the excess stress beyond the yield stress σ_o. The rod section is considered in two sections; above and below the neutral axis X-X. When a positive moment is applied, an additional plastic stress is experienced in the upper section of the rod and increases with slope β. The lower section of the rod unloads elastically with slope E. The problem becomes one of finding the neutral axis X-X that satisfies the condition of equilibrium as follows:

$$\int \sigma \, dA = 0 \tag{24}$$

Now

$$\sigma = \frac{\sigma_1}{\eta_1} \eta \text{ and } \sigma = \frac{\sigma_2}{\eta_2} \eta \tag{25}$$

From the equation of equilibrium (Equation 24),

$$\frac{\sigma_1}{\eta_2} \int_0^{\eta_1} \eta \, dA = \frac{\sigma_2}{\eta_2} \int_0^{\eta_2} \eta \, dA \tag{26}$$

49
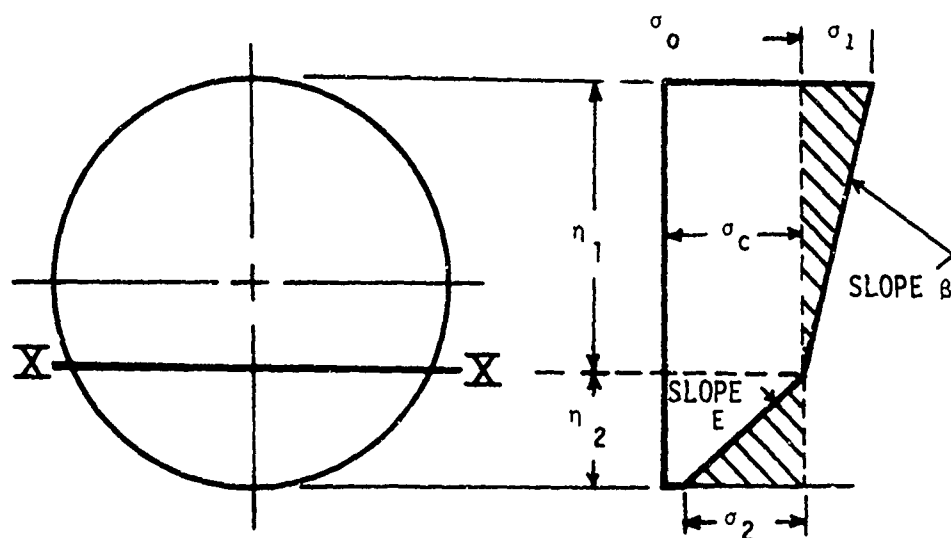
Figure 28.   Rod Cross Section Showing Stress Profile for Bending
Moment Superimposed on Plastic Compression.

$$E\overline{y}_2 = \beta\overline{y}_1 \tag{27}$$

Equation (27) is essentially a statement of static equilibrium, which states that there is an axis X-X, in which the stresses do not change. Also, the moment of inertia about X-X is as follows:

$$I = I_1 + I_2 \tag{28}$$

The bending moment becomes

$$M = \int \sigma\eta d\eta = \frac{\sigma_1 I_1}{\eta_1} + \frac{\sigma_2 I_2}{\eta_2} \tag{29}$$

The radius of curvature $\frac{\partial^2 y}{\partial x^2}$, is introduced:

$$M = \frac{\partial^2 y}{\partial x^2}(\beta I_1 + E I_2) \tag{30}$$

Equation (30) holds for the elastic as well as the plastic moment. For the elastic motion, β becomes the elastic modulus E and $I_1 + I_2$ equals I, where I is the moment of inertia about the gravity axis.

4. THE EQUATIONS OF MOTION

Substituting the expressions for the axial load P and the moment M into Equations (10) through (17), the following equations of motion and boundary conditions result:

(a) In the interior of the rod,

$$(EI_2 + \beta I_1)\frac{\partial^4 y}{\partial x^4} - \rho I \frac{\partial^4 y}{\partial x^2 \partial t^2} + \rho A \frac{\partial^2 y}{\partial t^2} = 0 \tag{31}$$

$$\beta \frac{\partial^2 u}{\partial x^2} - \rho \frac{\partial^2 u}{\partial t^2} = 0 \tag{32}$$

51

(b) At the boundary $x = 0$,

$$\frac{\partial u}{\partial x} = - \frac{F_x}{A\beta} \qquad \text{(STRAIN)} \tag{33}$$

$$\frac{\partial^2 y}{\partial x^2} = 0 \qquad \text{(MOMENT)} \tag{34}$$

$$(EI_2 + \beta I_1) \frac{\partial^3 y}{\partial x^3} - \rho I \frac{\partial^3 y}{\partial t^2 \partial x} - F_y = 0 \tag{35}$$

(c) At the boundary $x = L$,

$$\frac{\partial u}{\partial x} = 0 \tag{36}$$

$$\frac{\partial^2 y}{\partial x^2} = 0 \tag{37}$$

$$(EI_2 + \beta I_1) \frac{\partial^3 y}{\partial x^3} - \rho I \frac{\partial^3 y}{\partial t^2 \partial x} = 0 \tag{38}$$

The axial and lateral equations of motion are coupled through the
dynamic stress-strain relationship which involves the variable β, which
is the slope of the stress-strain relationship for both the elastic and
plastic wave propagations. Equations (31) and (38) must be solved as a
system, along with the equations of material behavior. Since the state
of stress is a uni-axial state and the plastic buckling is contained
within the plastic compression wave, the axial equation of motion will be
used to determine the axial strain, stress, and hence the slope of the
stress-strain relation β.

5. MATERIAL BEHAVIOR

Transverse shear was not included in the equations of motion, and
though it could have been easily introduced the inclusion would cause
the plasticity theory to be more complicated. Therefore, in the
interest of obtaining a solution within a specified time, this shear

has been omitted; however, the work could be extended to include the addition of transverse shear.

Figure 29 illustrates the flow theory that was utilized. Consider a uni-axial state of stress. The stress-strain relation may be expressed as

$$\varepsilon = \sigma/E + \varepsilon_p + \Delta\varepsilon_p \tag{39}$$

Where ε is the total strain, ε_p is the plastic strain, and $\Delta\varepsilon_p$ is the plastic strain increments due to the current increment of loading for a specified small increment of time Δt. The plastic strain increments are related to the stresses through the yield criterion and the associated flow rule. For the uni-axial state of stress, the Prandtl-Ruess flow rule can be avoided, and the partial differential equations of motion with the boundary conditions along with the stress-strain relation and the yield criterion form the necessary relations. In addition, the constant volume theory for plastic strain holds, which implies the material flows radially.

The problem solutions are carried out in increments of time as small as 10^{-7} second. First, the differential equations of motion are solved with the appropriate boundary condition having an assumed stress-strain slope β. Of course, to start the problem, the elastic slope is used for each position evaluated along the rod. From Equation (32) and the boundary conditions, an axial displacement u is computed for each particle along the rod. Then, a strain and a stress are computed. A test is made to determine whether the yield stress is exceeded for each particle along the rod, and if not, the elastic modulus E is used for the next increment of time Δt. If the yield stress is exceeded, the slope of the stress-

53
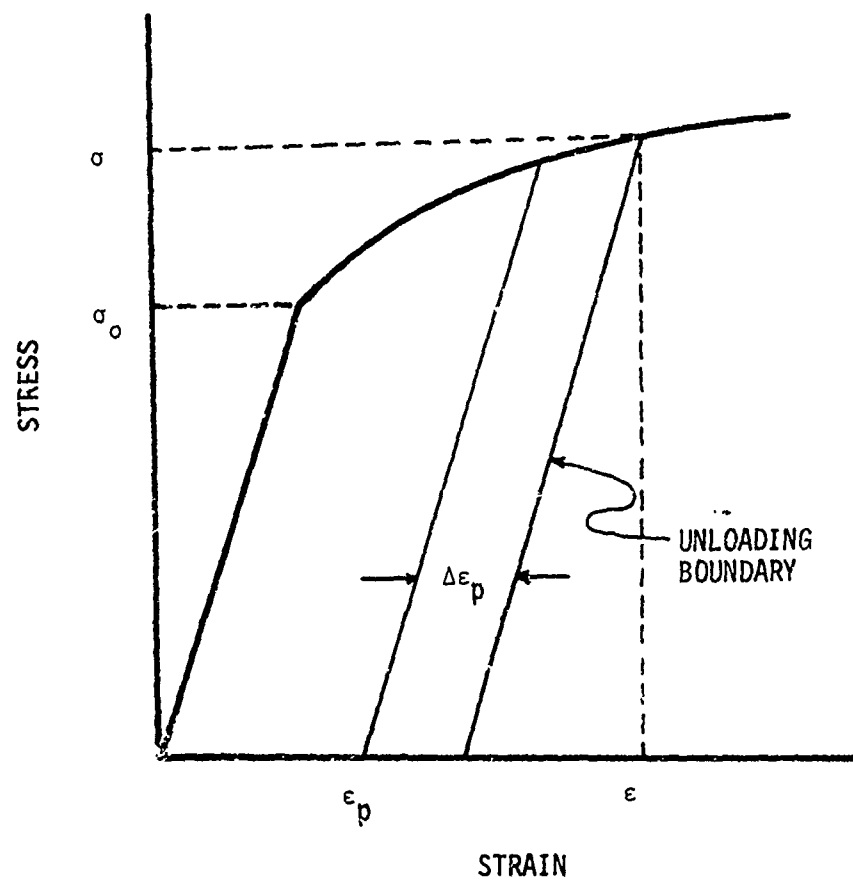
Figure 29.   The Elastic-Plastic Stress-Strain Relation

54

strain relation is then determined and used in the equations of motion
for the next increment of time.

6. SUMMARY

The elastic-plastic problem for buckling of long slender rods has
been formulated. The material characteristics will be utilized by
the stress-strain curve and applied by utilizing both elastic and
plastic regions subject to the plasticity flow rule and constant
volume cited previously. The following section will illustrate the
technique used for solution of this problem.

SECTION IV

NUMERICAL TECHNIQUES

Two numerical techniques were utilized to solve the equations of motion and material behavior. The finite difference method and Galerkin's method were used to provide solutions to the system of Equations (31) and (39). Galerkin's method provides a somewhat "continuous" solution along the spatial coordinate. In contrast, the finite difference technique offers a discrete solution in which the rod is treated as a system of discrete nodal points with the solutions being determined for each nodal point.

1. THE FINITE DIFFERENCE TECHNIQUE

The rod continuum is represented by a discrete number of nodal points (Figure 30) and solutions are sought for each nodal point for each time interval. The deflections at each nodal point must be considered as well as other parameters normally assumed to be constant for a pure elastic problem but which are also changing. Also the strain, stress, slope of the stress-strain relation, rod cross sectional area, and moment of inertia must be determined for each nodal point and at each time interval. Thus, another degree of nonlinearity is introduced into the problem; however, these changes in the geometric and mechanical properties of the rod can be handled effectively by a finite difference technique. It should be noted that the solutions for the deflections at the nodal points are interpreted to be deflections at the neutral axis of the rod.

In preparation for replacing the differential equations with finite difference approximations, forward, backward, and central difference relations were investigated for each disc.ate nodal point. Due to the boundary conditions, the most direct approach for obtaining a solution

56
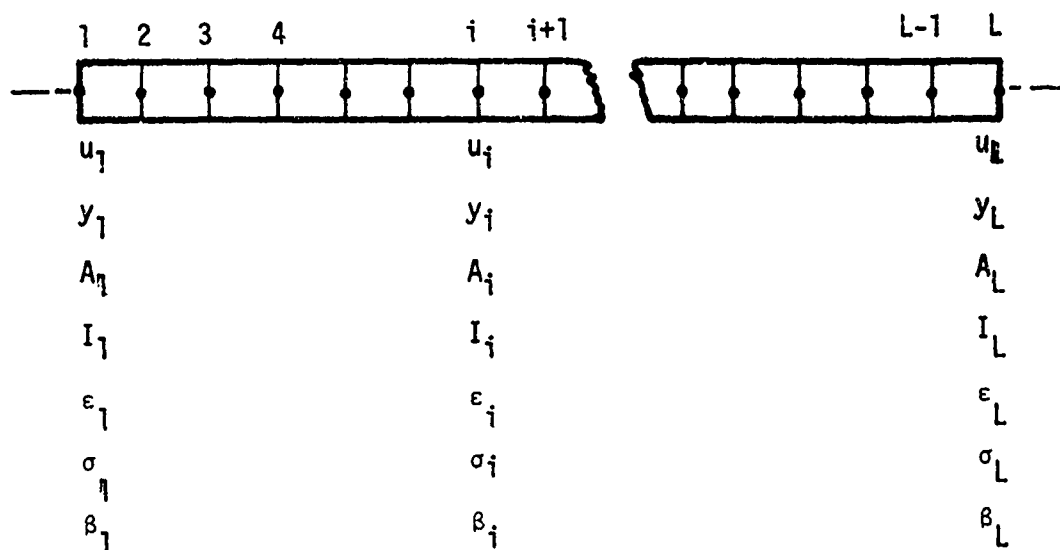
Figure 30. A Discrete Model of the Rod Showing Nodal Point Locations.

results when a mixture of forward, backward, and central differences are used, depending upon the nodal point under consideration. At the boundary point x = 0, forward differences were used to approximate each derivative with the exception of the second partial of the lateral deflection y with respect to x. At the interior nodes, central differences are used exclusively to obtain accuracy on the order of h^2. For the remaining boundary point x = L, the partial derivatives are approximated with backward differences with the only exception being the second partial derivative of the lateral deflection y with respect to x. Consideration was given to the possibility of using central differences only at all nodal points in order to maintain accuracy of the order h^2, but after the resulting expressions were examined, it was discovered that the resulting underconstrained system of differential equations gave more unknowns than equations. Solution of the underconstrained system could be obtained by "shooting methods;" that is, make an assumption of the value of the variables that lie outside the domain and the boundary of the rod and iterate until the assumed values satisfy the finite difference expressions. In essence, a boundary value problem is avoided by the proper selection of an approximating expression for the partial derivatives at the boundary points.

Now, consider approximations to the partial derivatives in Equations (31) through (39) at each nodal point in Figure 30. Defining the distances between the nodal points as h results in the forward difference expressions:

$$\left.\frac{\partial y}{\partial x}\right)_i \approx \frac{y_{i+1} - y_i}{h} + O(h) \tag{40}$$

$$\left.\frac{\partial^2 y}{\partial x^2}\right)_i \approx \frac{y_{i+2} - 2 y_{i+1} + y_i}{h^2} \tag{41}$$

$$\frac{\partial^3 y}{\partial x^3}\Big)_i \approx \frac{y_{i+3} - 3\,y_{i+2} + 3\,y_{i+1} - y_i}{h^3} \tag{42}$$

$$\frac{\partial^4 y}{\partial x^4}\Big)_i \approx \frac{y_{i+4} - 4\,y_{i+3} + 6\,y_{i+2} - 4\,y_{i+1} + y_i}{h^4} \tag{43}$$

Using central differences results in the following approximations:

$$\frac{\partial y}{\partial x}\Big)_i \approx \frac{y_{i+1} - y_{i-1}}{2h} + O(h^2) \tag{44}$$

$$\frac{\partial^2 y}{\partial x^2}\Big)_i \approx \frac{y_{i-1} - 2\,y_i + y_{i+1}}{h^2} \tag{45}$$

$$\frac{\partial^3 y}{\partial x^3}\Big)_i \approx \frac{-\,y_{i-2} + 2\,y_{i-1} - 2\,y_{i+1} + y_{i+2}}{2h^3} \tag{46}$$

$$\frac{\partial^4 y}{\partial x^4}\Big)_i \approx \frac{y_{i-2} - 4\,y_{i-1} + 6\,y_i - 4\,y_{i+1} + y_{i+2}}{h^4} \tag{47}$$

The backward difference expressions are given as follows:

$$\frac{\partial y}{\partial x}\Big)_i \approx \frac{y_i - y_{i-1}}{h} + O(h) \tag{48}$$

$$\frac{\partial^2 y}{\partial x^2}\Big)_i \approx \frac{y_i - 2\,y_{i-1} + y_{i-2}}{h^2} \tag{49}$$

$$\frac{\partial^3 y}{\partial x^3}\Big)_i \approx \frac{y_i - 3\,y_{i-1} + 3\,y_{i-2} - y_{i-3}}{h^3} \tag{50}$$

$$\frac{\partial^4 y}{\partial x^4}\Big)_i \approx \frac{y_i - 4\,y_{i-1} + 6\,y_{i-2} - 4\,y_{i-3} + y_{i-4}}{h^4} \tag{51}$$

Similar expressions may be obtained for the derivatives involving the deflection u. Now consider the equations describing the motion at the boundary and interior. Finite difference expressions for these equations are obtained with the aid of forward, central, and backward difference expressions.

a. Axial Motion

Now to express finite difference relations for the axial equation of motion, the following is repeated.

At the boundary $x = 0$, or nodal point 1, the equation is

$$\frac{\partial u}{\partial x} = -\frac{F_x}{A\beta} \tag{52}$$

When forward differences are used, Equation (52) becomes:

$$\frac{u_2 - u_1}{h} = -\frac{F_x}{A_1\beta_1} \tag{53}$$

At interior point 2, the expression is

$$-\beta\frac{\partial^2 u}{\partial x^2} + \rho\frac{\partial^2 u}{\partial t^2} = 0 \tag{54}$$

Using central differences, Equation (54) becomes:

$$-\beta_2(u_1 - 2u_2 + u_3)/h^2 + \rho\ddot{u}_2 = 0 \tag{55}$$

Rearranging Equation (55) and eliminating u_1 with Equation (53), gives

$$\ddot{u}_2 = \frac{\beta_2}{\rho h^2}\left(\frac{F_x h}{A_1\beta_1} - u_2 + u_3\right) \tag{56}$$

60

At all other interior points, except L-1, the value for u_i is

$$\ddot{u}_i = \frac{\beta_i}{\rho h^2} (u_{i-1} - 2u_i + u_{i+1})$$ (57)

At the boundary point $x = L$, the strain vanishes, so

$$\frac{\partial u}{\partial x} = 0$$ (58)

Using backward differences, the result is

$$u_L = u_{L-1}$$ (59)

Now at the interior point L-1, the following holds:

$$\ddot{u}_{L-1} = \frac{\beta_{L-1}}{\rho h^2} (u_{L-2} - u_{L-1})$$ (60)

Where u_L has been eliminated with the aid of Equation (59).

The result is L-2 differential equations with L-2 unknowns which can be evaluated by numerical methods. The deflections at the boundary points $x = 0$ and $x = L$ may be determined from the algebraic expressions at $x = 0$ and $x = L$, respectively.

b. Lateral Motion

Applying the same procedure for the lateral motion as for the axial, at the boundary $x = 0$ or at node 1 the following partial differential equations apply:

61

$$\frac{\partial^2 y}{\partial x^2} = 0 \tag{61}$$

$$(EI_2 + \beta I_1)_1 \frac{\partial^3 y}{\partial x^3} - \rho I \frac{\partial^3 y}{\partial t^2 x} - _\cdot y = 0 \tag{62}$$

Applying central differences to the moment equation:

$$y_0 - 2 y_1 + y_2 = 0 \tag{63}$$

Now applying forward differences to the derivative $\frac{\partial^3 y}{\partial x^3}$ and central differences to $\frac{\partial y}{\partial x}$ in the force balance Equation (62), the following expression holds:

$$(EI_2 + \beta I_1)_1 (y_4 - 3_{y3} + 3_{y2} - y_1) - \rho I_1 \frac{\partial^2}{\partial t^2} \frac{(y_2 - y)}{2h} - $$

$$F_y = 0 \tag{64}$$

Eliminating y_0 from Equation (64) with the use of Equation (63), the following expression holds:

$$\ddot{y}_2 - \ddot{y}_1 = - \frac{F_y h}{\rho I_1} + \frac{(EI_2 + \beta I_1)}{h^2 \rho I_1} 1 (y_4 - 3y_3 + 3y_2 - y_1) \tag{65}$$

At the node 2, the following holds:

$$\frac{\rho I_2}{h^2} (\ddot{y}_1 - 2\ddot{y}_2 + \ddot{y}_3) + \rho A_2 \ddot{y}_2 = $$

$$\frac{(EI_2 + \beta I_1)}{h^4} 2 (y_0 - 4y_1 + 6y_2 - 4y_3 + y_4) \tag{66}$$

Eliminating y_0 with the aid of Equation (63), the following differential equation of motion results for node 2.

$$- \frac{\rho I_2}{h^2}(\ddot{y}_1 - 2\ddot{y}_2 + \ddot{y}_3) + \ddot{y}_2 =$$

$$- \frac{(EI_2 + \beta I_1)}{\rho A_2 h^4}2(- 2y_1 + 5y_2 - 4y_3 + y_4) \qquad (67)$$

Now, at all other nodal points, except node L-1, the following finite difference expression holds:

$$\frac{I_i}{A_i h^2}(\ddot{y}_{i-1} - 2\ddot{y}_i + \ddot{y}_{i+1}) - \ddot{y}_i =$$

$$\frac{(EI_2 + \beta I_1)_i}{\rho A_i h^4} \quad (y_{i-2} - 4y_{i-1} + 6y_i - 4y_{i+1} + y_{i+2}) \qquad (68)$$

At the nodal point L-1, the following holds:

$$\frac{I_{L-1}}{A_{L-1} h^2}(\ddot{y}_{L-2} - 2\ddot{y}_{L-1} + \ddot{y}_L) - \ddot{y}_{L-1} =$$

$$\frac{(EI_2 + \beta I_1)}{\rho A_{L-1} h^4}_{L-1}(y_{L-3} - 4y_{L-2} + 5y_{L-1} - 2y_L) \qquad (69)$$

At the boundary $x = L$, the moment equation $y_{L-1} - 2y_L + y_{L+1} = 0$ is used to eliminate y_{L+1} in the force balance equation giving:

$$\ddot{y}_L - \ddot{y}_{L-1} = \frac{(EI_2 + \beta I_1)_L}{\rho I_L h^2}(y_L - 3y_{L-1} + 3y_{L-2} + y_{L-3}) \qquad (70)$$

63

Now L second-order coupled differential equations result with L unknowns, and with the use of numerical techniques, the lateral deflections at each nodal point may be determined. In matrix notation the system may be represented by the following:

$$[A] \{\ddot{y}\} = [B] \{y\} + \{F_y(t)\} \tag{71}$$

In Equation (71) the [A] matrix is a tri-diagonal matrix, with the [B] matrix containing four non-zero elements in each row and four non-zero elements in each column, except the first and last column.

2. GALERKIN'S METHOD

Galerkin's method is based on the idea of minimization of errors by orthogonalizing with respect to a selected set of trial functions. The first step is to choose a trial solution which contains undetermined parameters or functions. For the rod impact problem, trial solutions of the following form are selected:

$$u(x,t) = \sum_{k=1}^{N} f_k(t) \, \phi_k(x) \tag{72}$$

$$y(x,t) = \sum_{k=1}^{N} g_k(t) \, \gamma_k(x) \tag{73}$$

Where $\phi_k(x)$ and $\gamma_k(x)$ are known functions and $f_k(t)$ and $g_k(t)$ are functions to be determined. The trial functions must satisfy the forced boundary conditions at $x = 0$ and $x = L$. If some of the end conditions are natural or free, as is the case for the impact problem, the boundary terms must be added to the minimization. Defining an equation residual as $R(x,t)$ and applying Galerkin's technique give

$$\int_0^L R_k(x,t)\phi_k(x)dx + B_0 = 0 \tag{74}$$

64

Where $R(x,t)$ is obtained by substituting the trial solutions into the equation of motion (Equation 32) and equating the result to $R(x,t)$:

$$R(x,t) = (\beta \frac{\partial^2}{\partial x^2} - \rho \frac{\partial^2}{\partial t^2}) u(x,t)$$

B_0 represents the boundary terms. An equation residual is likewise obtained for the lateral equation of motion and may be expressed:

$$e(x,t) = [(EI_2 + \beta I_1) \frac{\partial^4}{\partial x^4} - \rho I \frac{\partial^2}{\partial x^2} \frac{\partial^2}{\partial t^2} + \rho A \frac{\partial^2}{\partial t^2}] y(x,t)$$

Now, consider the boundary terms. For the axial equation, the minimization leads to the following expression:

$$\int_0^L R(x,t)\phi_k(x)dx + A\beta\phi_k(x)\frac{\partial}{\partial x}u(x,t)\Big|_0^L - F_x\phi_k(0) = 0 \qquad (75)$$

Adding the boundary terms to the lateral equation gives

$$\int_0^L e(x,t)\gamma_k(x)dx + (EI_2 + \beta I_1) [\frac{\partial \gamma_k}{\partial x} \frac{\partial^2 y}{\partial x^2} - \frac{\partial^3 y}{\partial x^3} \gamma_k(x)] \Big|_0^L +$$

$$\rho I \frac{\partial^2}{\partial t^2}(\frac{\partial y}{\partial x} \gamma_k(x)) \Big|_0^L - F_y\gamma_k(0) = 0 \qquad (76)$$

Performing the indicated integrations and other operations for Equations (75) and (76), a coupled system of second order ordinary differential equations result and can be expressed in matrix form as

$$[C] \{\ddot{f}\} = [D] \{f\} + \{F_x(t)\} \qquad (77)$$

65

$$[F] \{\ddot{g}\} = [G] \{g\} + \{F_y(t)\} \tag{78}$$

Where the matrixes [C], [D], [F] and [G] are N by N, with N being the number of terms in the finite series approximations for $u(x,t)$ and $y(x,t)$. The two systems given by Equations (77) and (78) appear to be independent at first notice, but they are coupled through the stress-strain relation, and the numerical technique used to solve for the solution components for $f_k(t)$ and $g_k(t)$ must consider the coupling effects. Once the $f_k(t)$ and $g_k(t)$ are determined, the deflections are obtained from Equations (72) and (73). One might note that the strain at a point of interest may be obtained by merely taking the partial derivative of u with respect to x. Also the velocity components of the particles are obtained from the solutions for $g_k(t)$ and $f_k(t)$ by using $\dot{f}_k(t)$ and $\dot{g}_k(t)$.

The selection of the appropriate trial functions for $\phi_k(x)$ and $\gamma_k(x)$ present problems for the rod impact problem because of the boundary conditions. Observing the experimental results obtained, the first choice for a trial function would obviously involve a sine or cosine function. Several trial functions were investigated with varying degrees of success. The most successful trial function for the axial motion was determined to be

$$\phi_k(x) = 1 + (-1)^k \sin [(2k - 1) \pi x/2L] \tag{79}$$

Equation (79) satisfies all of the free boundary conditions. The properties of $\phi_k(x)$ are such that $\frac{\partial \phi}{\partial x}$ vanishes at $x = L$, implying the strain vanishes at the free end, and $\frac{\partial \phi}{\partial x}$ does not vanish at $x = 0$ where the strain is a maximum. Also, $\phi_k(x)$ does not vanish at $x = 0$ and $x = L$, thus implying

66

the rod is free to move axially at the impacted end as well as the free end, hence satisfying the free boundary conditions.

The proper choice of a trial function for the lateral deflections proved to be troublesome, with the free boundary conditions being the most difficult to satisfy. Finally, the trial function as given by the following equation offers a limited degree of acceptability:

$$\gamma_k(x) = 1 - y_0 x/L + y_1 \sin (k\pi x/L) \tag{80}$$

Where y_0 and y_1 are amplitude constants. Note that $\gamma_k(x)$ vanishes at the boundary $x = L$ for $y_0 = 1$, implying the lateral deflection is zero, therefore, a violation of the free boundary condition occurs at this point. However, this violation is minor, considering the fact that the only deflection at the free end is elastic. Another trial function used with some success, but again a violation of the free condition at $x = 0$, the impacted end, is

$$\gamma_k(x) = y_0 \sin \left[\frac{(2k - 1)}{2L} \pi x \right] \tag{81}$$

Where y_0 is still an amplitude constant. The function given in Equation (81) performed nicely about two diameters from the impacted end. For the orthogonal impact, the function given by Equation (81) would be preferred since no lateral deflections are possible at the impacted end.

In addition to the conditions on $\phi_k(x)$ and $\gamma_k(x)$, there are conditions on $f_k(t)$ and $g_k(t)$ that must be satisfied. So far, no restrictions have been placed on $f_k(t)$ and $g_k(t)$; that is, $u(x,t)$ and $y(x,t)$ satisfy the boundary conditions through $\phi_k(x)$ and $\gamma_k(x)$ for all t. Since the following initial conditions hold:

67

$$u(x,0) = \dot{u}(x,0) = 0 \tag{82}$$

$$y(x,0) = \dot{y}(x,0) = 0 \tag{83}$$

The implications are,

$$f(0) = \dot{f}(0) = 0 \tag{84}$$

$$g(0) = \dot{g}(0) = 0 \tag{85}$$

Equations (84) and (85) state that the deflections and the velocities of a particle along the rod are zero initially when the forcing function is applied. When the problem is considered as a pure impact problem, the forcing function is not applied, but each particle in the rod is given an initial velocity equal to the impact velocity. Thus, the initial conditions become,

$$\dot{u}(x,0) = v_0 \tag{86}$$

$$\dot{y}(x,0) = v_0 \sin\theta \tag{87}$$

Where θ is the obliquity angle at impact.

3. FORCING FUNCTIONS

By application of Newton's Law for a force acting on a particle, the forcing functions can be determined for any desired shape. Newton's Law simply reduces to the statement that the time rate of change of linear momentum is equal to the impulse, thus

$$\int_0^T F(t)dt = \int_0^{v_0} m\frac{dv}{dt}\, dt = mv_0 \tag{88}$$

Where T is the impact duration, and v_0 is the impact velocity. The

assumption is made that the velocity component resulting from the elastic bounce-back from the plate may be ignored.

Four types of forcing functions were considered as illustrated in Figure 31. The trapezoid, rectangular, and parabolic forcing functions were used with the finite difference technique, and the sinuscidal forcing function was used with Galerkin's technique along with the other three forcing functions. Since the area under each of the curves in Figure 31 is the change in momentum, or simply the product $m\ v_o$, the forcing functions may be determined by application of Equation (88).

The best overall results for predicting the displacement of a particle as a function of time was obtained by using the trapezoidal forcing function. However, during the initial time after impact, the rectangular forcing function gave the better results. A comparison between the forcing functions is presented later in this report, when the comparisons between the analytical and experimental results are discussed.
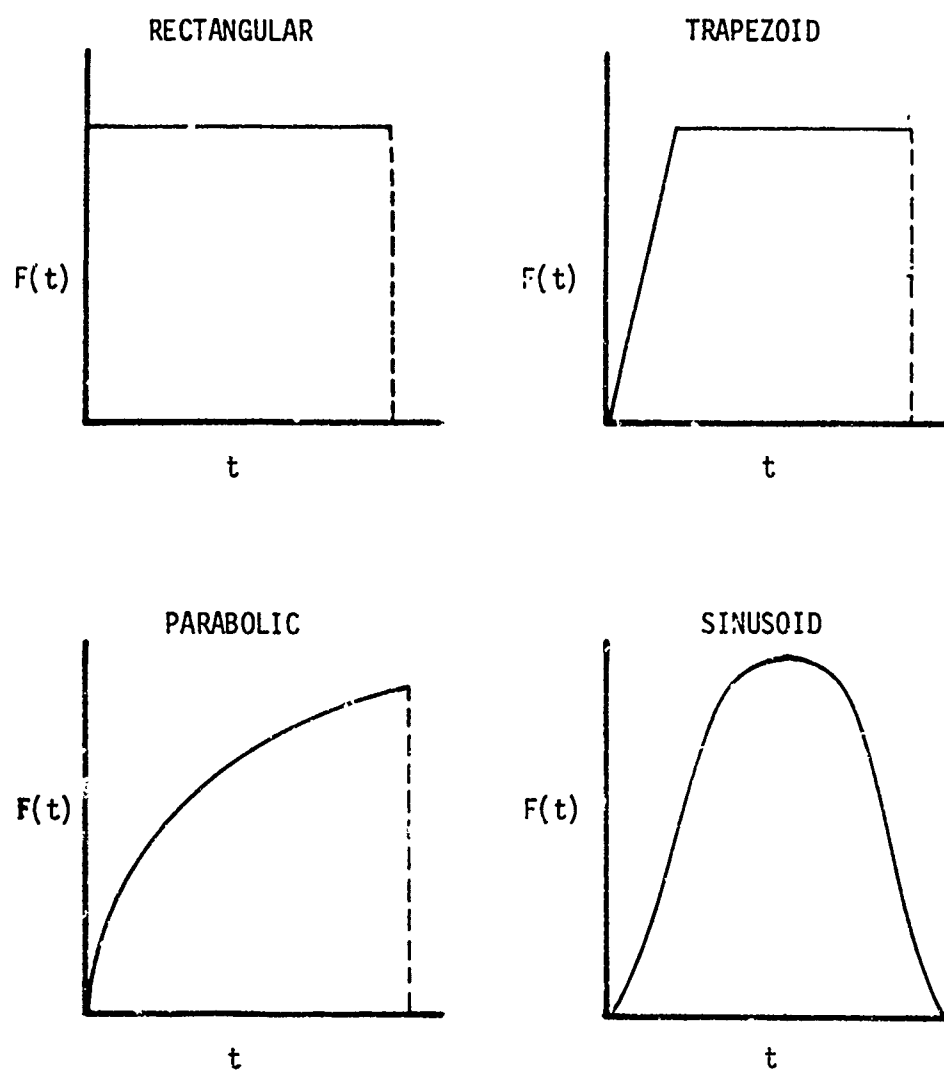
Figure 31. Forcing Function used in Analysis.

SECTION V

THE COMPUTER PROGRAMS

Two computer programs were written, one for the Galerkin's technique and one for the finite difference method. An algorithm was first written for Galerkin's method, but the results using the method did not meet with the desired expectations, so the finite difference technique was employed with better results. Basically, the two algorithms are similar with each having an integration, a derivative, and a linear system subprogram in common.

1. ALGORITHM FOR FINITE DIFFERENCE TECHNIQUE

Figure 32 shows the program flow for the finite difference technique. The computer program contains a main program; a Runge-Kutta, or predictor corrector, integration algorithm; a derivative subroutine; a linear simultaneous equation subprogram to solve for u and y using gaussian elimination; and an output subroutine.

The main program is divided into two parts (Figure 32). The first part of the program reads the input data, such as rod length, diameter, impact velocity, angle, etc., and initializes all variables. Then the Runge-Kutta integration subprogram (RUNKUT) is called to integrate the equations of motion. RUNKUT in turn, calls a program (DERIVY) to obtain derivatives for the algorithm, but since a coupled system of differential equations is involved, the values of y for each nodal point must be determined. So DERIVY develops a linear system of the for.

$$[A] \ \{x\} = \{C\} \tag{89}$$

where the {x} values are the {ÿ} values, and then DERIVY calls a program

71
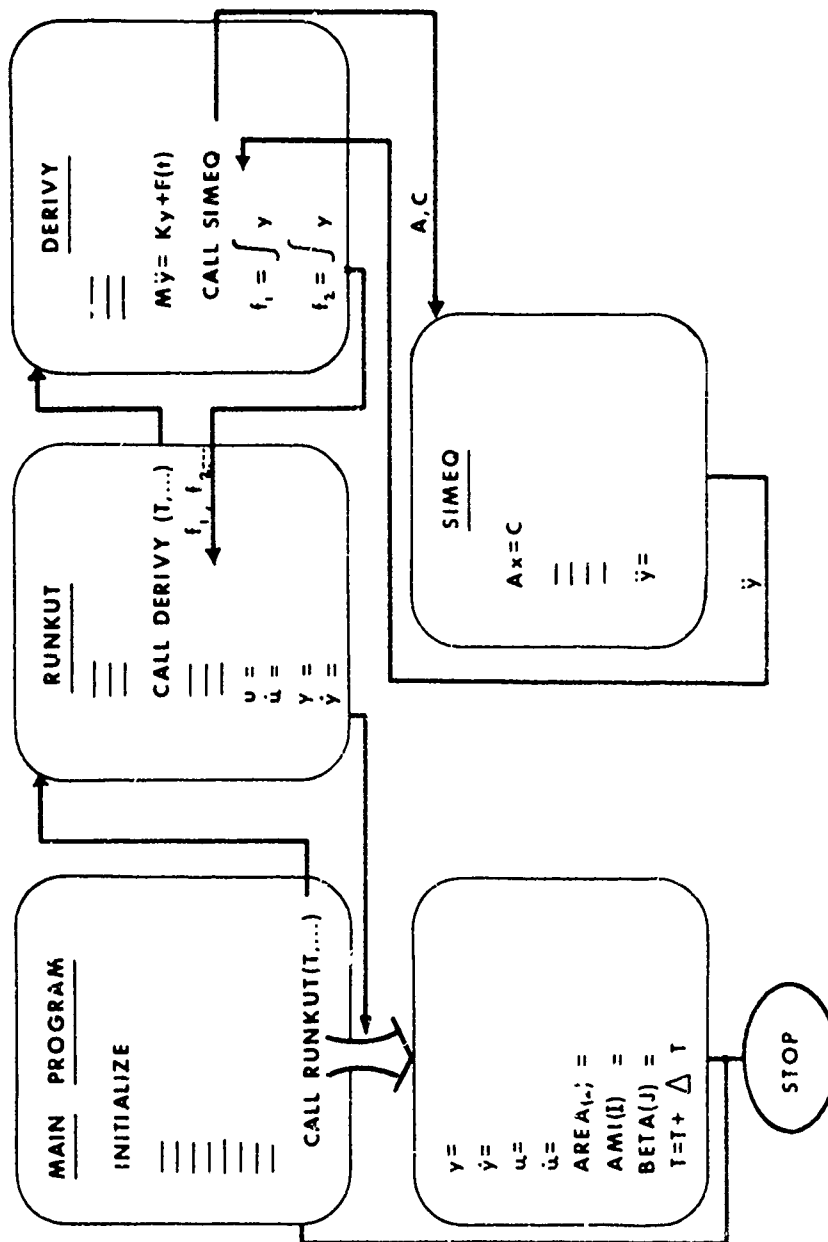
Figure 32. Computer Program Flow for Finite Difference Technique.

72

(SIMEQ) which solves a linear system of equations for the $\{\ddot{y}\}$ vector and passes the solution components back to DERIVY. DERIVY then determines the remaining derivatives and passes the derivative vector to RUNKUT. RUNKUT, in turn, passes the displacement and velocity vectors for each nodal point back to the main program.

The second part of the main program receives the displacement and velocity vectors for the discrete time interval $t + \Delta t$ and computes strains, stresses, slopes of the stress-strain curve, areas, and moments of inertia for each nodal point. If desired, an output subroutine is called and the required information is printed for the time interval. A typical output is shown in Table II for a 6-inch rod for two discrete time intervals of 5 and 15 microseconds. If output is not desired, another increment of time is added, and the program cycles through the process until the impact duration time is reached.

2. ALGORITHM FOR GALERKIN'S METHOD

The algorithm for the Galerkin method is similar to the finite difference algorithm as previously described. Here, RUNKUT is called upon to provide the values of the undetermined functions $f_k(t)$, $g_k(t)$, $\dot{f}_k(t)$, and $\dot{g}_k(t)$ at discrete times. Once these values are determined, the displacements, strains, and strain rates may be determined. A typical output for the Galerkin method is given in Table III for one discrete time during the impact. Note the propagation of the wave motion for the Galerkin method is not as well defined as for the finite difference method. The propagation of the elastic waves are masked by the "noise" of the technique and hence would not be suitable for elastic wave propagation problems.

73

TABLE II. FINITE DIFFERENCE OUTPUT

IMPACT VELOCITY '00. IMPACT DURATION 75. IMPACT ANGLE .0000210   1.00   ROD LENGTH 6.   DX .250000
ROD DIAMETER .250000   INTEGRATION STEP SIZE .0000210   FORCING FUNCTION 3

TIME	NODE NO.	AXIAL DISP	LATERAL DISP	STRAIN	STRESS	AXIAL VEL	LATERAL VEL	RADIUS
.000005	1	.003382	.000769	-.005444	-45767.	1036.	441.	.125342
.000005	2	.002021	.000089	-.004964	-49642.	1036.	72.	.125000
.000005	3	.000899	.000014	-.003516	-35157.	709.	-15.	.125000
.000005	4	.000263	-.000004	-.001707	-17067.	317.	-5.	.125000
.000005	5	.000046	-.000000	-.000516	-5160.	81.	-0.	.125000
.000005	6	.000005	-.000000	-.000092	-918.	12.	0.	.125000
.000005	7	.000000	-.000000	-.000009	-93.	1.	-0.	.125000
.000005	8	.000000	-.000000	-.000000	-5.	1.	0.	.125000
.000005	9	.000000	-.000000	-.000000	-0.	0.	-0.	.125000
.000005	10	0.000000	-.000000	-.000000	-0.	0.	-0.	.125000
.000005	11	0.000000	-.000000	0.000000	0.	0.	-0.	.125000
.000005	12	0.000000	-.000000	0.000000	0.	0.	-0.	.125000
.000005	13	0.000000	-.000000	0.000000	0.	0.		.125000
.000005	14	0.000000	-.000000	0.000000	0.	0.	0.	.125000
.000005	15	0.000000	-.000000	0.000000	0.	0.	0.	.125000
.000005	16	0.000000	-.000000	0.000000	0.	0.	0.	.125000
.000005	17	0.000000	-.000000	0.000000	0.	0.	0.	.125000
.000005	18	0.000000	-.000000	0.000000	0.	0.	0.	.125000
.000005	19	0.000000	-.000000	0.000000	0.	0.	0.	.125000
.000005	20	0.000000	-.000000	0.000000	0.	0.		.125000
.000005	21	0.000000	-.000000	0.000000	0.	0.	-0.	.125000
.000005	22	0.000000	-.000000	0.000000	0.	0.	-0.	.125000
.000005	23	0.000000	-.000000	0.000000	0.	0.	-0.	.125000
.000005	24	0.000000	-.000000	0.000000	0.	0.	-0.	.125000
.000005	25	0.000000	-.000000	0.000000	0.	0.	-0.	.125000

74

TABLE II. CONCLUDED

TIME	NODE NO.	AXIAL DISP	LATERAL DISP	STRAIN	STRESS	AXIAL VEL	LATERAL VEL	RADIUS
.000015	1	.259634	.008174	-.338234	-110147.	17812.	984.	.153659
.000015	2	.175076	.002099	-.420132	-126526.	17812.	329.	.164152
.000015	3	.049568	-.000150	-.314531	-105406.	9498.	9.	.150979
.000015	4	.017810	-.000275	-.077299	-57960.	2694.	-38.	.130131
.000015	5	.010919	-.000070	-.018301	-46160.	1505.	-14.	.126160
.000015	6	.008659	.000018	-.008439	-47563.	1284.	2.	.125531
.000015	7	.006699	.000018	-.006875	-46625.	1211.	4.	.125432
.000015	8	.005222	.000005	-.006107	-46164.	1209.	2.	.125383
.000015	9	.003646	-.000001	-.006159	-46195.	1186.	-0.	.125367
.000015	10	.002142	-.000001	-.005338	-45703.	1108.	-0.	.125335
.000015	11	.000977	-.000000	-.003584	-35841.	710.	-0.	.125000
.000015	12	.000350	-.000000	-.001751	-17511.	325.	0.	.125000
.000015	13	.000101	-.000000	-.000654	-6535.	114.	0.	.125000
.000015	14	.000024	-.000000	-.000193	-1930.	31.	0.	.125000
.000015	15	.000004	-.000000	-.000046	-459.	1.	-0.	.125000
.000015	16	.000001	-.000000	-.000009	-88.	0.	-0.	.125000
.000015	17	.000000	-.000000	-.000001	-14.	0.	0.	.125000
.000015	18	.000000	.000000	-.000000	-2.	0.	0.	.125000
.000015	19	.000000	-.000000	-.000000	-0.	0.	-0.	.125000
.000015	20	.000000	-.000000	-.000000	-0.	0.	0.	.125000
.000015	21	.000000	-.000000	.000000	-0.	0.	-0.	.125000
.000015	22	.000000	-.000000	-.000000	-0.	0.	0.	.125000
.000015	23	.000000	.000000	-.000000	-0.	0.	0.	.125000
.000015	24	.000000	.000000	-.000000	-0.	0.	-0.	.125000
.000015	25	.000000	.000000	0.000000	0.	0.	0.	.125000

TABLE III

OUTPUT FROM GALERKIN'S METHOD

IMPACT VELOCITY 850. IMPACT DURATION .000075 IMPACT ANGLE .52 ROD LENGTH 6. ROD RAD .125000

INTEGRATION STEP SIZE .0000010 NO. TERMS IN GALERKINS SOLUTION 25

TIME	X	AXIAL DISP	LATERAL DISP	STRAIN	AXIAL VEL	STRAIN RATE	LATERAL VEL
.0000100	0.0000000	.1363280	-.0080350	.2155471	-10367.9648159	-65820.8553614	-1484.9653348
.0000100	.1250000	.1042869	-.0172472	.3280790	-16874.8479586	-26381.4908044	-3009.9485399
.0000100	.2500000	.0542896	-.0165314	.4389402	-15557.9089102	45537.4782625	-3171.5314631
.0000100	.3750000	.0069334	-.0090654	.2715486	-7521.3737755	71349.4786285	-2137.4759802
.0000100	.5000000	.0085022	-.0043067	-.0114869	-345.3832171	36830.8392133	-1109.4525638
.0000100	.6250000	-.0004436	-.0042733	.0853105	1417.3905362	-4742.9664659	-749.7161777
.0000100	.7500000	-.0049373	-.0043249	.0209495	-1.3278021	-11061.6440299	-745.5079399
.0000100	.8750000	-.0012295	-.0028382	.0520272	-652.3642686	1936.8466061	-664.4200802
.0000100	1.0000000	-.0033602	-.0021579	.0217840	33.5510286	6198.7688686	-520.4063392
.0000100	1.1250000	-.0014449	-.0026399	.0362827	383.5463431	-1160.3205270	-462.0010310
.0000100	1.2500000	-.0024418	-.0024234	.0216607	-37.2285104	-3890.1877674	-446.5270089
.0000100	1.3750000	-.0015144	-.0015666	.0265912	-256.0007858	830.6911427	-391.5925697
.0000100	1.5000000	-.0018211	-.0015043	.0212683	35.9965553	2705.2467865	-335.3926833
.0000100	1.6250000	-.0015264	-.0016814	.0197868	185.0334603	-657.2643039	-319.5255742
.0000100	1.7500000	-.0013621	-.0015501	.0207154	-33.9465999	-2812.1336479	-304.9795320
.0000100	1.8750000	-.0015088	-.0010247	.0146174	-141.3533823	553.4605093	-268.4792783
.0000100	2.0000000	-.0010019	-.0011888	.0200503	31.9832773	1570.3562929	-242.8847146
.0000100	2.1250000	-.0014728	-.0014150	.0104829	112.5142862	-485.8053875	-237.0428325
.0000100	2.2500000	-.0007077	-.0010375	.0192900	-30.2974711	-1271.0696678	-222.1344669
.0000100	2.3750000	-.0014237	-.0007420	.0070587	-92.4715688	436.9501982	-197.2151392
.0000100	2.5000000	-.0004605	-.0009921	.0184439	28.8919313	1058.9532920	-185.3660962
.0000100	2.6250000	-.0013644	-.0010741	.0041540	77.9956227	-484.9296178	-181.3115605
.0000100	2.7500000	-.0002489	-.0007002	.0175193	-27.7230233	-903.4609660	-166.5854248
.0000100	2.8750000	-.0012968	-.0005804	.0016500	-67.2405687	379.1812070	-149.8435036
.0000100	3.0000000	-.0006654	-.0008420	.0165223	26.7383390	786.6701419	-144.5602078
.0000100	3.1250000	-.0012221	-.0007999	.0005309	59.0950025	-356.8478226	-139.6946418
.0000100	3.2500000	-.0000950	-.0004666	.0154591	-25.0831828	-697.6578247	-125.9594442
.0000100	3.3750000	-.0011413	-.0004817	.0024409	-52.0731385	341.9580006	-115.2450997
.0000100	3.5000000	-.0002357	-.0007082	.0143364	25.1034520	629.5039523	-112.7606021
.0000100	3.6250000	-.0010553	-.0005681	.0041164	48.1489183	-326.9720004	-106.4098028
.0000100	3.7500000	-.0003591	-.0003026	.0131616	-24.3414405	-578.2960584	-94.3682978
.0000100	3.8750000	-.0009650	-.0004151	.0055831	-44.6782358	312.4512844	-88.0262963
.0000100	4.0000000	-.0004670	-.0005765	.0119433	23.5212959	541.5419644	-86.1477923
.0000100	4.1250000	-.0008711	-.0003684	.0068596	42.3584040	-296.7168761	-78.4516113
.0000100	4.2500000	-.0005607	-.0001884	.0106925	-22.5325087	-516.7264613	-68.5641168
.0000100	4.37 0000	-.0007748	-.0003617	.0079601	-41.2361375	277.2908664	-65.1827343
.0000100	4.50 0000	-.0006413	-.0004405	.0094240	21.1763349	511.0185861	-62.6153168
.0000100	4.6250000	-.0006777	-.0001967	.0088961	41.5578012	-249.6264635	-54.0908347

SECTION VI

ANALYTICAL RESULTS

Analytical results have been obtained for the approximate solutions
to the equations of motion and material behavior using the two numerical
techniques discussed previously. In this section, the analytical results
are presented for both the elastic and plastic response of the rod, along
with the comparisons with the experimental work where appropriate. In
addition, the analytical work of this effort is compared with the work
of others when possible.

1. ELASTIC FLEXURAL WAVES

The problem of the elastic flexural wave propagation along a rod has
been solved by a number of investigators. The best surveys on the subject
are given by Kolsky in Reference 2 and by Abramson, Plass, and Ripperger
in Reference 1, which gives the phase velocity for flexural elastic waves
in a solid circular cylinder of radius r as a function of the wavelength λ.
These results are given for three theories and are repeated in Figure 33
with the results of this analysis (Valentine) being presented as a compar-
ison. The elementary theory presented shows that the phase velocity in-
creases without bound as the flexure wave length λ approaches zero.
Basically, the phase velocity is given by the following relation:

$$C = C_o \, 2\pi \left(\sqrt{\tfrac{I}{A}} \, \lambda \right) \tag{90}$$

Where C_o is the bar velocity and I and A are the moments of inertia and
areas of the cross section, respectively. A somewhat disconcerting fact
is that the phase velocity tends to infinity for the very short wave
lengths; however, if a term is added for rotary inertia, as was done in
this work, the condition of infinite flexure wave speed is avoided.

77
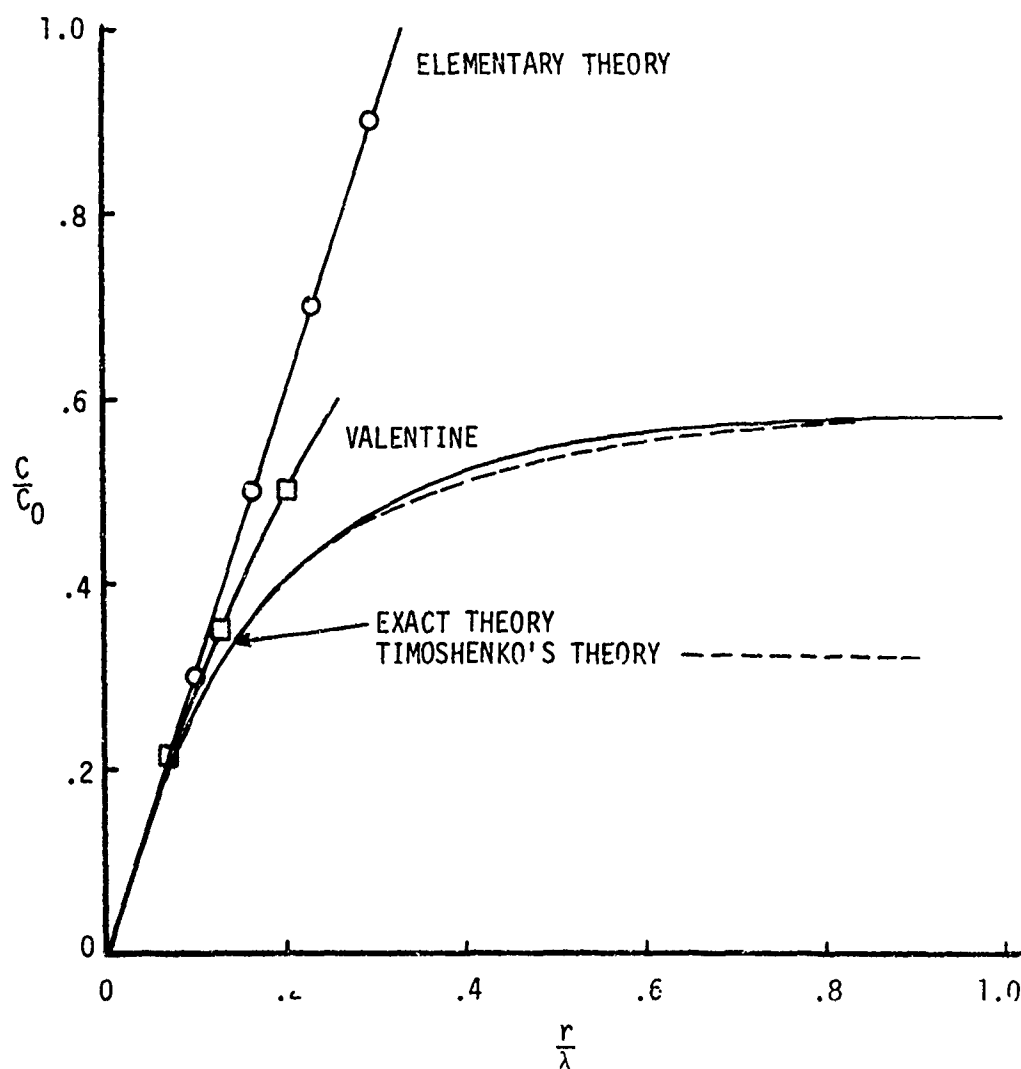
Figure 33. Phase Velocity Comparisons for Flexural Elastic Waves
in a Solid Circular Cylinder of Radius r.

78

Timoshenko (Reference 9) further added a term for transverse shear which agrees with the exact three-dimensional solution of Pochhammer and Love for the first mode, but a wide discrepancy occurs in the second mode. Referring to Figure 33, the comparison of this work for the flexure wave velocity C is given for the several theories with the exact theory being shown for a Poisson's ratio of 0.29 and for the first mode only. The effects of rotary inertia and shear are unimportant if the wavelength of the vibration mode is large compared with the cross sectional dimensions of the rod. But the effects of rotary inertia and shear become more important with a decrease in wavelength. The results obtained from Timoshenko's theory show the advantage of including the transverse shear in the equations of motion or elastic flexural waves for the short wavelengths. The results of this analysis include rotary inertia but not transverse shear and are shown in Figure 33 for an impulsively applied load for the aluminum rods.

2. PLASTIC FLEXURE WAVES--COMPARISON WITH WORK OF ABRAHAMSON AND GOODIER

Although Abrahamson and Goodier made no attempt to predict the buckling mode shapes, considerable work is reported in Reference 3 for the prediction of the plastic wavelength of the flexure wave arising primarily from initial transverse perturbational velocity, such as an oblique impact. A Fourier integral transform was used to solve the lateral equation of motion:

$$\frac{\partial^4 \omega}{\partial x^4} + \frac{\partial^2 \omega}{\partial x^2} + \frac{\partial^2 \omega}{\partial \tau^2} = - \frac{\partial^2 \omega_0}{\partial \tau^2} \qquad (91)$$

Where τ is the dimensionless variable containing time and ω is the dimensionless variable y/k, with y being the lateral deflection and k the radius of gyration of the rod. Abrahamson and Goodier reported their results in

79

terms of half wavelength but these terms have been converted to wavelengths to simplify the comparison with the results of this work. The results of Abrahamson and Goodier yield the following relation for the wavelength:

$$\lambda = 2\pi\sqrt{\frac{I}{A}} \ (\beta/\sigma)^{1/2} \tag{92}$$

Where λ is the wavelength, β is the plastic modulus, and σ is the stress in the rod. Abrahamson and Goodier assumed the stress in the rod was constant, thus yielding:

$$\lambda = 17.7\sqrt{\frac{I}{A}} \tag{93}$$

Now, it is possible to compare the results of Abrahamson and Goodier with the results of this work (Valentine). In addition, both analytical results may be compared to the experimental results of this work. Since Equation (93) was derived for 18 inch rods, the results of the firings for the 1/4 inch diameter rods of 18 inches in length (Table IV) are used as a basis for comparison.

TABLE IV

WAVELENGTHS FOR 18 INCH 6061-T6 ALUMINUM RODS (1/4 INCH DIAMETER)

Shot No.	Impact Velocity (fps)	Average Wavelength, Inches		
		Observed from Experiments	Predicted Valentine	Predicted Abrahamson
9	649	1.4	0.88	1.1
	602	1.15	0.94	1.1
11	540	1.06	0.95	1.1
	412	1.15	1.22	1.1
	252	1.50	1.64	1.1
2i	228	1.675	1.80	1.1
11	222	1.875	1.80	1.1

80

While the analytical work of Abrahamson and Goodier predicts a constant wavelength, it may be observed from Table IV that the analytical work reported herein predicts a wavelength as a function of the impact velocity. The constant wavelength theory of Abrahamson is attributed to the assumption of a constant compressive force P in the rod, whereas the wavelengths determined by this analysis use the actual state of stress and strain experienced at each nodal point. Hence, the slope of the stress-strain curve is easily determined. In addition, the axial displacements contribute toward decreasing the wavelengths. When the flexure wave initially forms, the wavelength is longer than the final wavelength. The axial displacements, due to the axial force, tend to compress the wavelengths, thus accounting for the shorter wavelengths at the higher impact velocities.

An indication of the accuracy of this analysis may be obtained by referring to the predicted and observed wavelengths of Table IV. Note that the theory of Abrahamson and Goodier is in good agreement with experimental results at the higher impact velocities, but does not predict the wavelengths as accurately as the theory developed in this work for the lower impact velocities.

3. STRESS AND STRAIN PROFILES

Stress and strain profiles have been determined for several impact conditions for the 6, 12, and 18 inch rods for the forcing functions considered in this work. Typically, the stress profiles are represented by those of Figures 34 and 35 where a bilinear stress-strain relationship is used. Note that the elastic wave front builds to the yield stress as it propagates toward the free end. The stress remains at yield for some distance along the rod until the plastic wave front builds near the

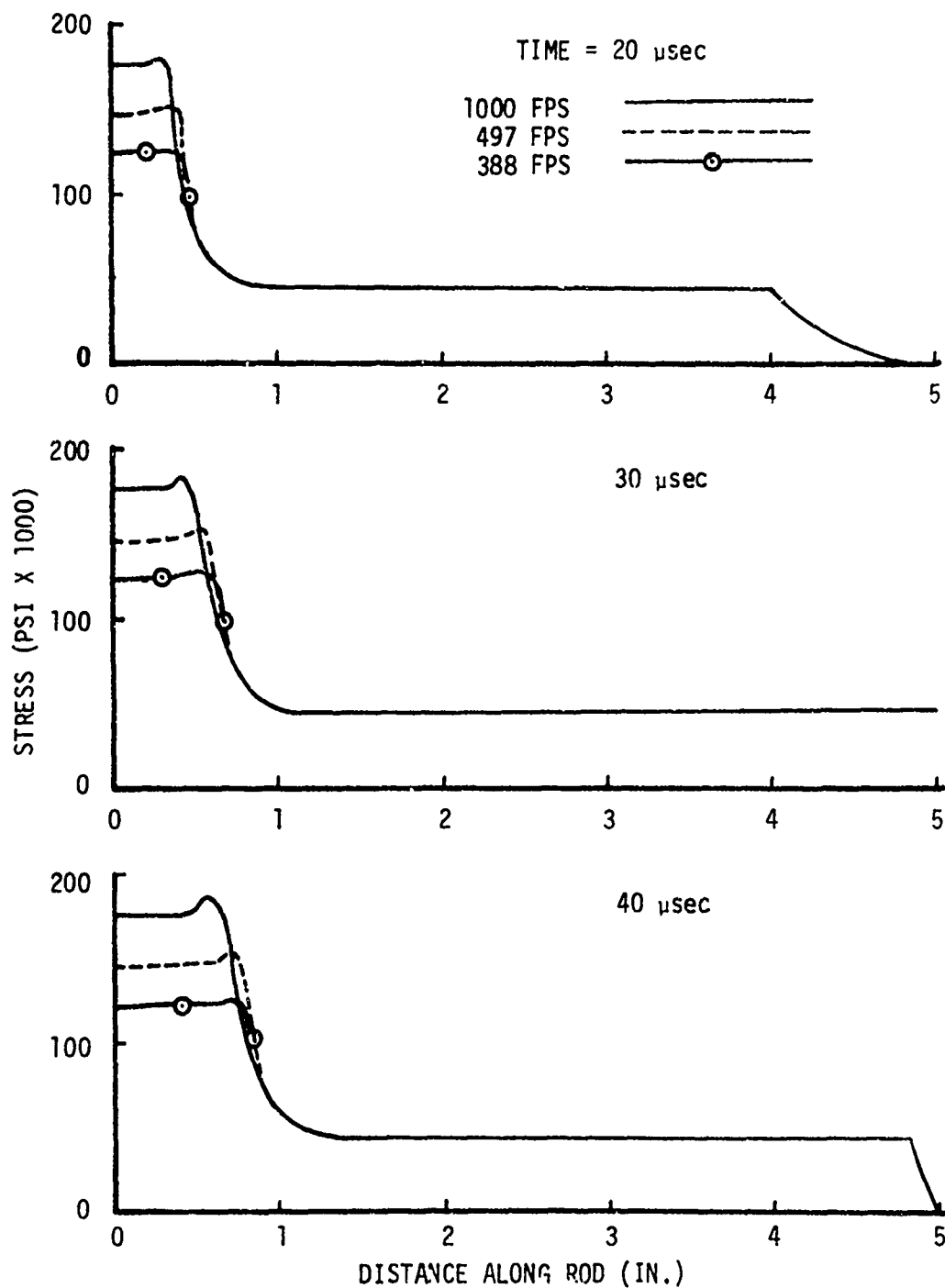Figure 34. The Distribution of Stress Along the Rod at Three Distinct
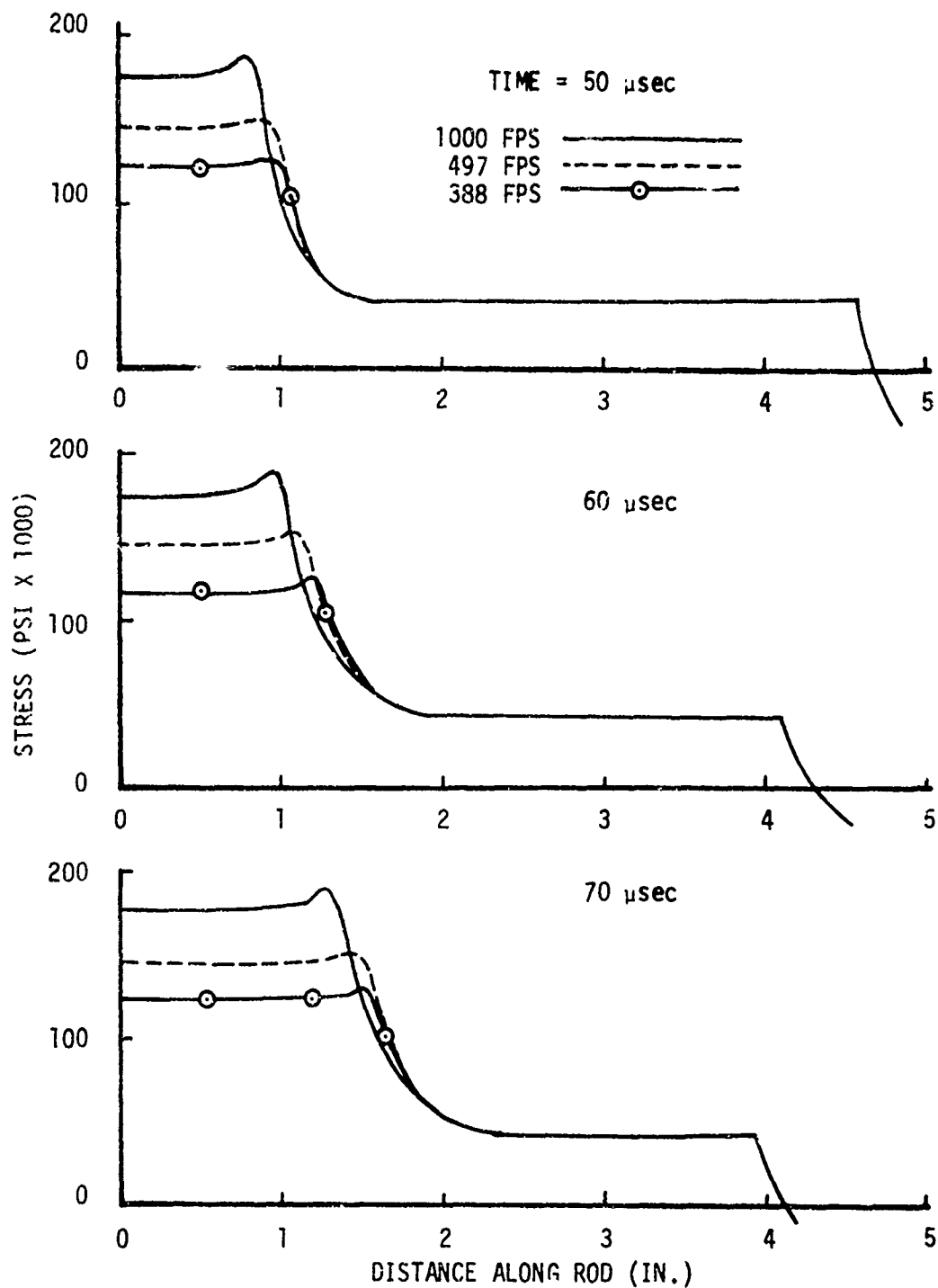Time Intervals of 20, 30, and 40 μsec. for 6 Inch Rod
Impacts.

82

Figure 35. The Distribution of Stress Along the Rod at Time Intervals of 50, 60 and 70 μsec. for 6 Inch Rod Impacts.

impacted end. The region between the elastic wave front and the plastic wave front is extremely steep as would be expected from a bilinear stress-strain relation. As may be seen from Figure 34, the plastic wave front moves much slower than the elastic wave front. During the first time interval of 20 μsec after impact, the elastic wave front is 4 inches down the rod, and at 33 μsec, the elastic wave front reaches the free end and reflects back as a tensile wave. The later time sequences show that the compressive stress vanishes near the free end as the tensile wave travels toward the impacted end. Also, the effect of impact velocity on the stress profile essentially changes the magnitude of the stresses.

Strain profiles are similar to the stress profiles and are presented to show the magnitude of the strains that may be expected for various impact velocities. Since the stresses and strains are determined at a point, they are presented at the neutral axis. Figures 36 and 37 show the distribution of strain along the rod at distinct time intervals of 20, 30, 40, 50, 60, and 70 microseconds. The plastic strains are shown; however, there is also an elastic strain similar to the previously illustrated elastic stress, but the magnitude is such that it cannot be illustrated on the same scale of Figures 36 and 37.

Figure 38 shows the final axial plastic strain distribution along the rod obtained from the analytical results computed using a rectangular forcing function and compared to the experimental results. As shown, the results for the strain profiles are not in good agreement with the experimental results. Other forcing functions were investigated to provide better agreement between the analytical and experimental strain profiles. Figure 39 illustrates the dependence of the strain

Figure 36. The Distribution of Strain Along the Rod at
Three Time Intervals of 20, 30, and 40 µsec.
for 6 Inch Rod Impacts.

85
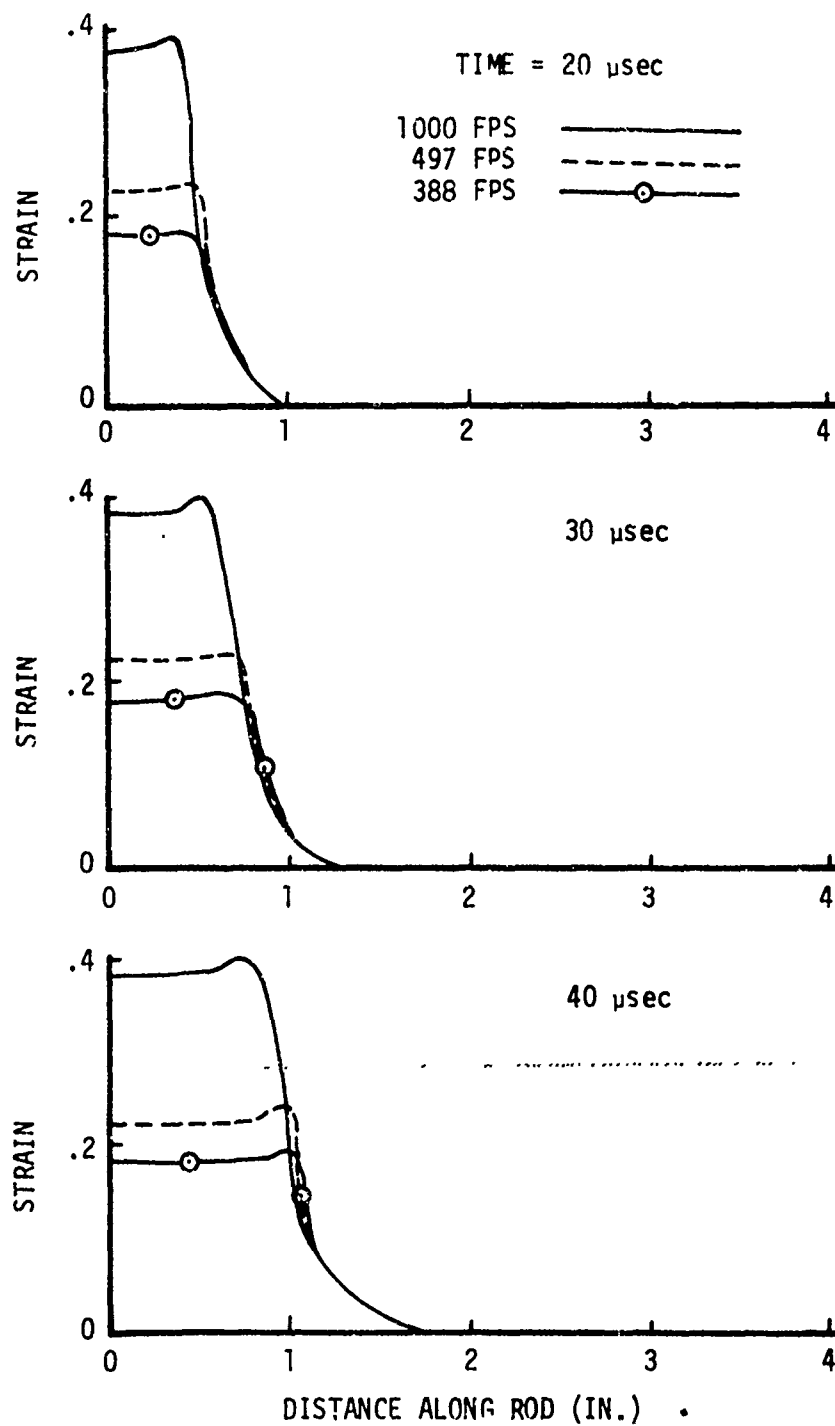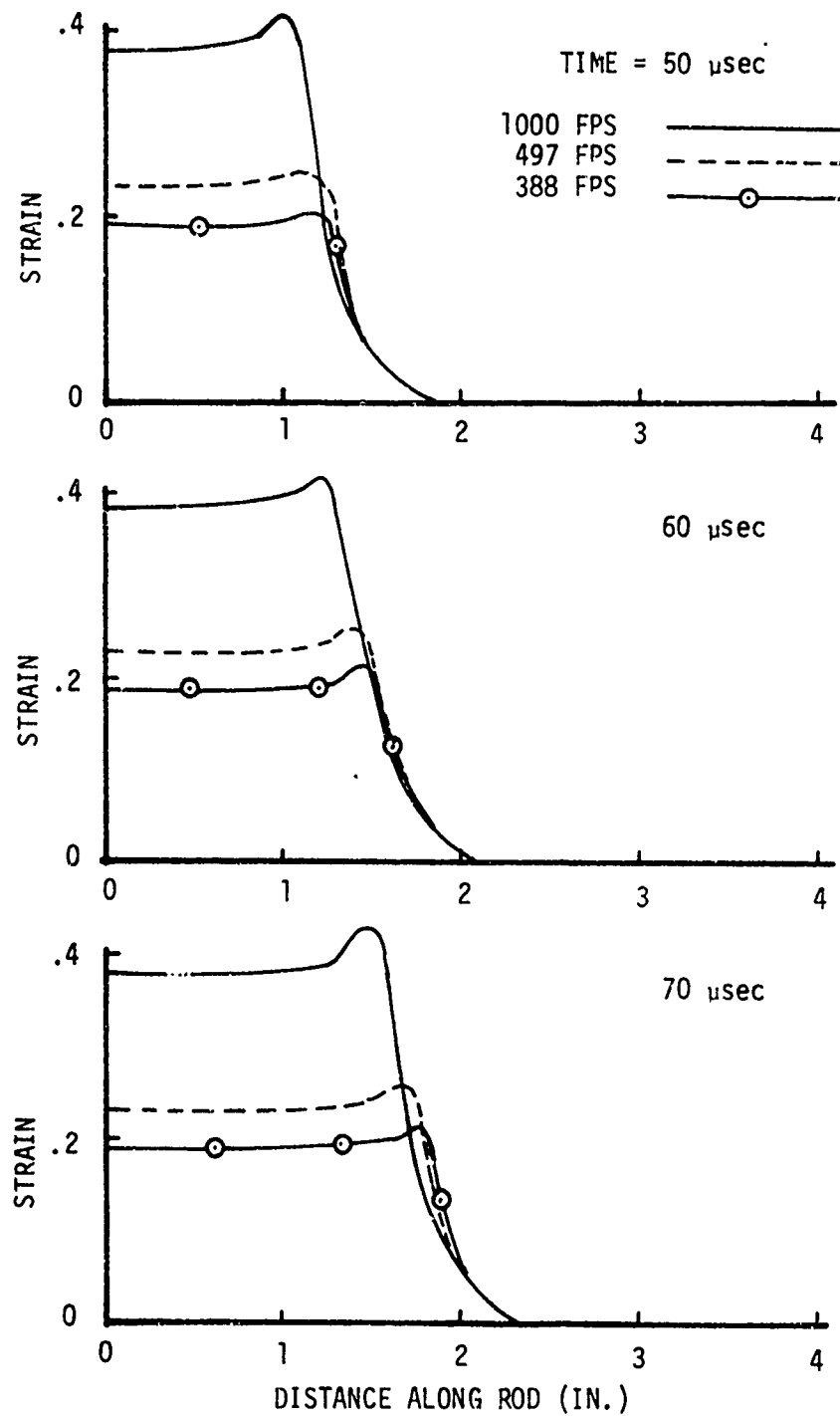
Figure 37. The Distribution of Strain Along the Rod at Three Time Intervals of 50, 60, and 70 μsec. for 6 Inch Rod Impacts.
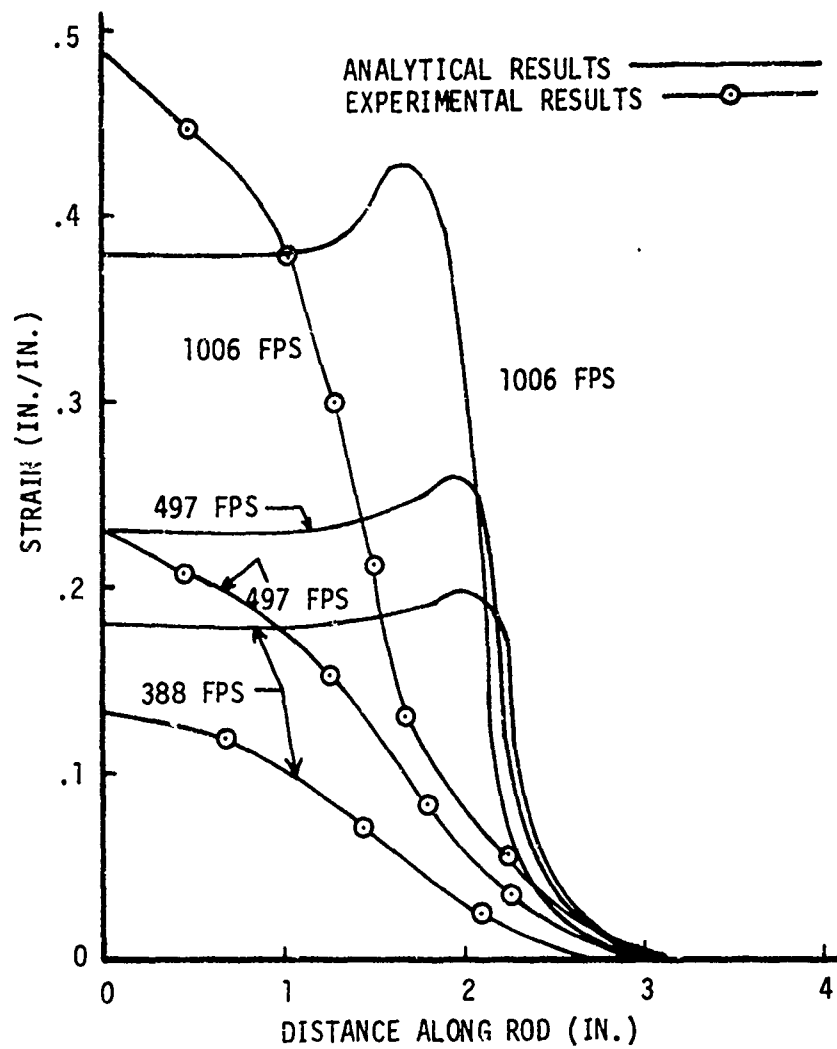
Figure 38.   A comparison of the Distribution of Plastic
Strains for 6 Inch Rod for Rectangular
Forcing Functions.

87
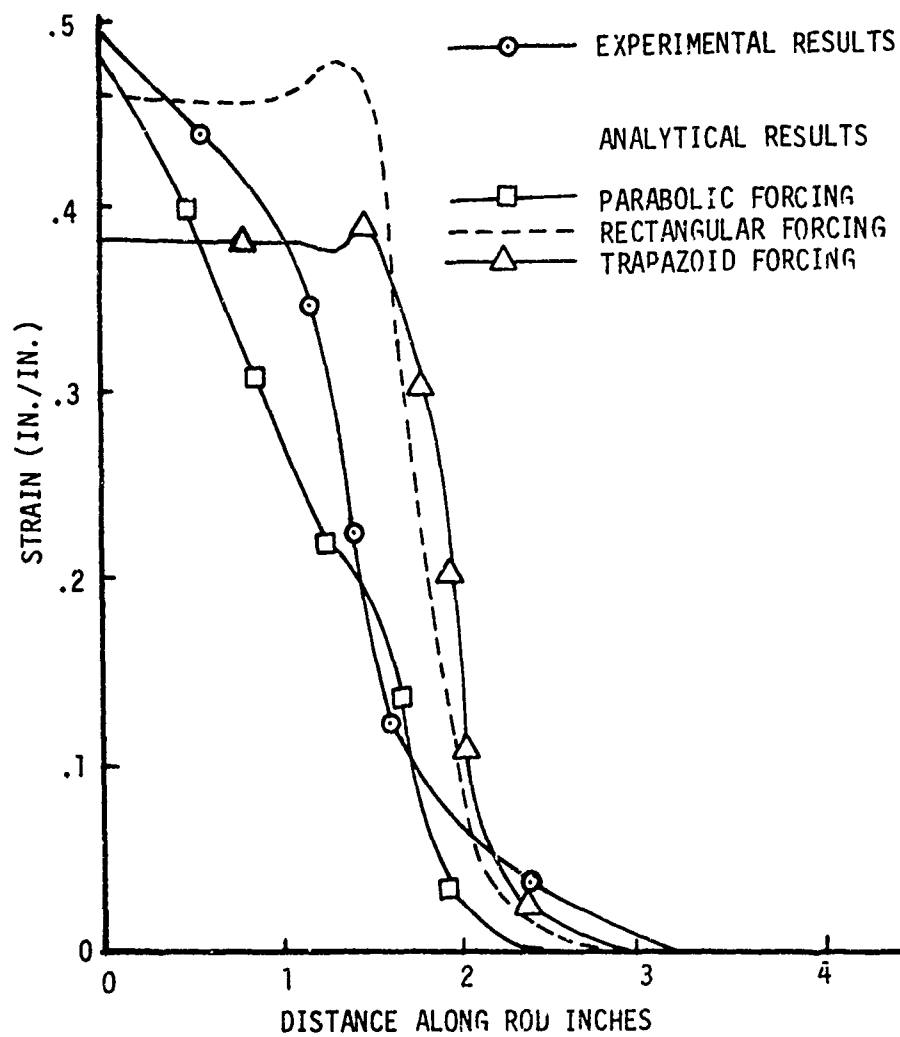
Figure 39. A Comparison of Various Forcing Functions for Impact of 1006 fps for 6 Inch Rod.

distributions on the type of forcing function used, thus a pure impact solution is desirable with a two-body problem being formulated.

4. AXIAL DEFORMATION

In determining the amount of axial deformation, the length of the rod was obtained as a function of time by tracking the free end of the rod during the impact process. Comparisons with the experimental results for several impact velocities are presented in Figures 40 through 42 for 6, 12, and 18 inch long rods of 1/4 inch diameter. Good agreement is obtained when comparing the analytical and experimental results for the instantaneous rod lengths. These results were obtained using a trapazoid forcing function and using the finite difference technique. Figures 40 through 42 show that the analytical model tends to overpredict the axial deformation. This fact was observed in all of the analytical results obtained except for the one impact velocity that occurred at 1217 fps, where the method underpredicts the axial deformation. For the high impact velocity of 1217 fps, considerable material loss occurred near the impacted end due to fracture at high stresses and high loading rates. The theory developed herein does not consider fracture, internal friction, or the energy absorbed by the rod in elevating its temperature during the impact.

Figure 40.   A Comparison of the Instantaneous Rod Lengths
for 6 Inch Rods of 1/4 Inch.
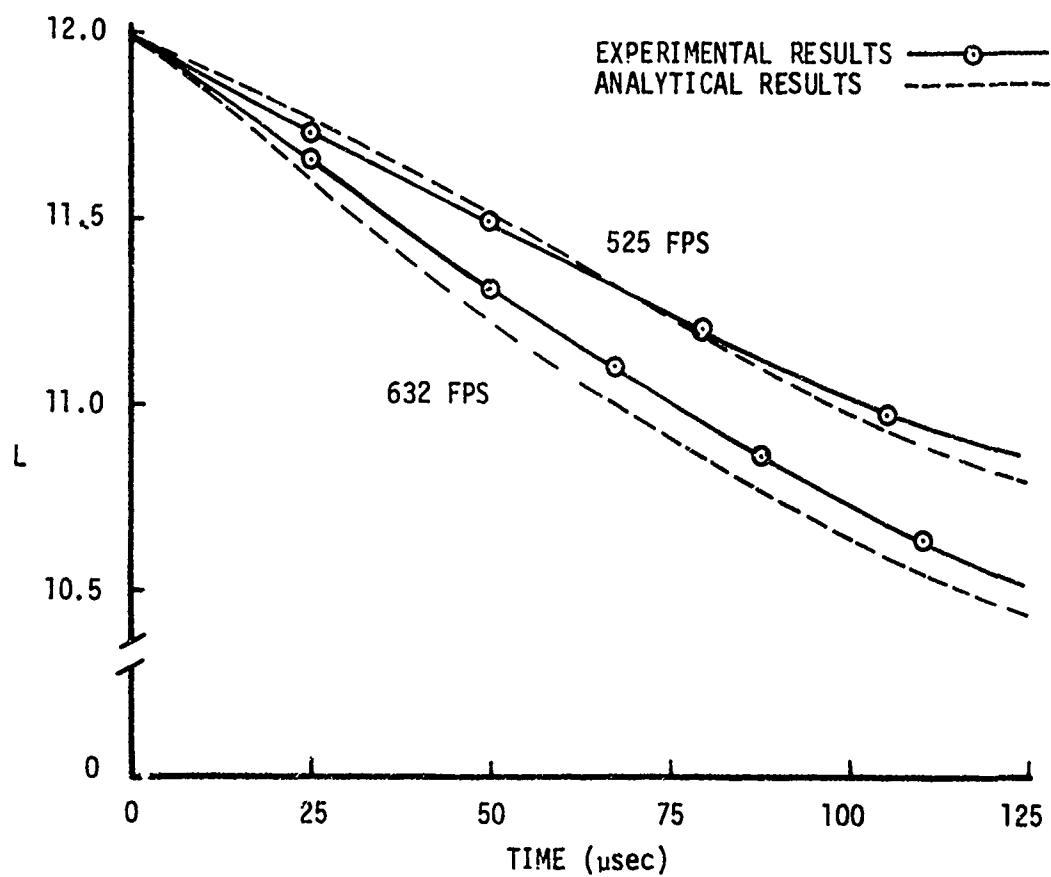
Figure 41. A Comparison of the Instantaneous Rod Lengths for 12 Inch
Rods of 1/4 Inch Diameter.
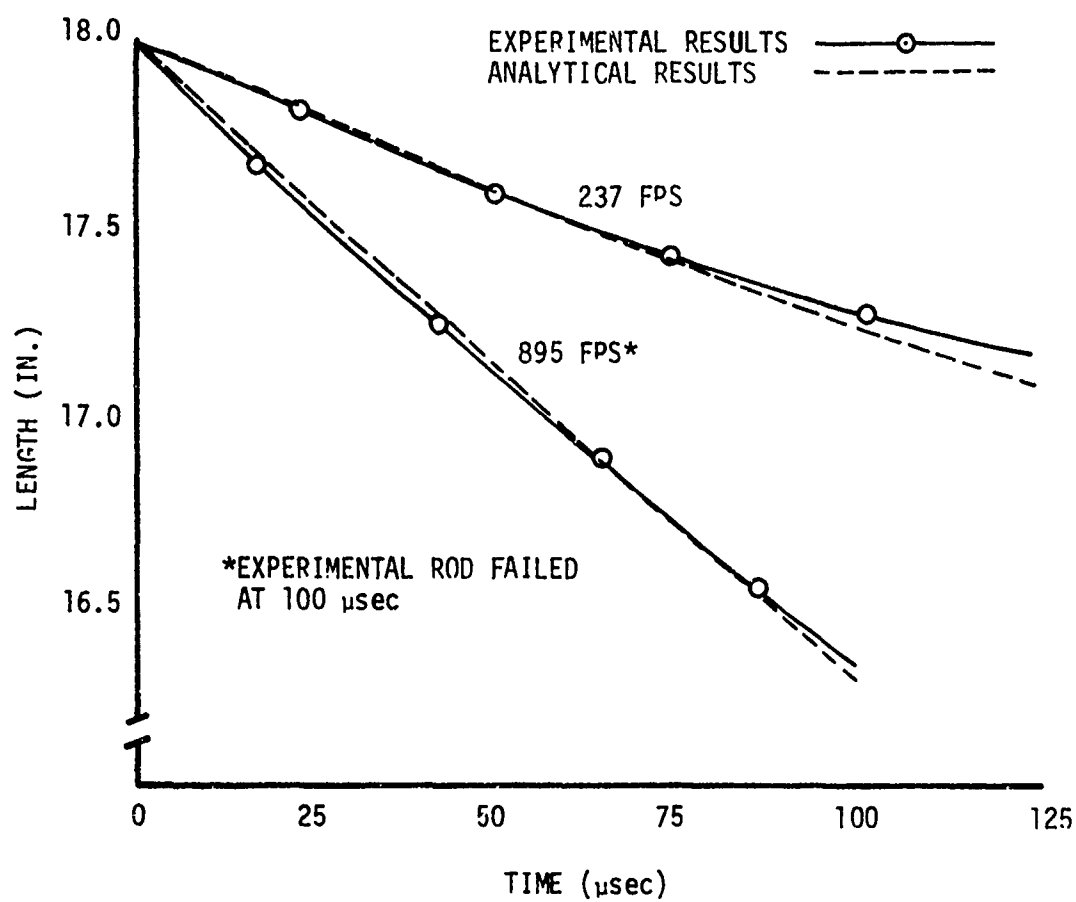
Figure 42. A Comparison of the Instantaneous Rod Lengths for 18 Inch
Rods of 1/4 Inch Diameter.

5. LATERAL DEFORMATION PROFILES

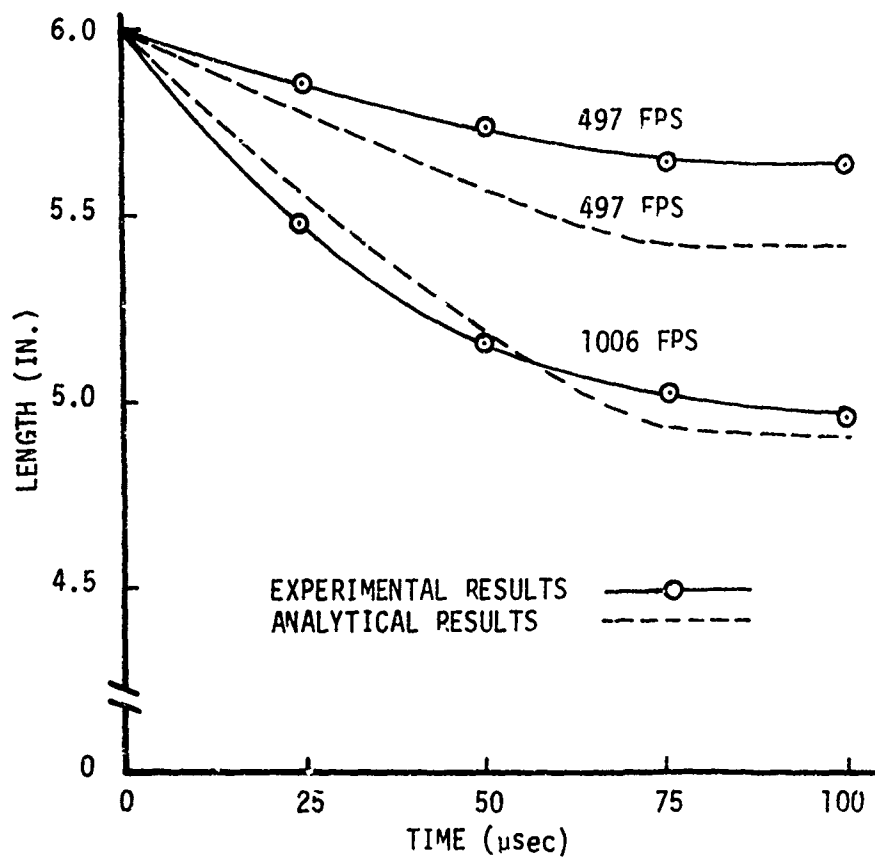A Lagrangian formulation of the problem has been developed, and a particle on the rod can now be followed through the time response. Thus, the axial and lateral displacements, u and y, of any nodal point can be followed at any time. Since it is assumed that the material flow occurs radially, the displacement of the neutral axis is also the displacement of the gravity axis. Also the radial material flow allows the determination of the area profile at any nodal point by the application of a fundamental law of plasticity stating there is no change in plastic volume.

Figures 43 through 50 show the essential analytical results of this work, using the method of finite differences for several times during the impact process. The last view on each figure is the final mode shape obtained and is compared directly with the experimental rod under the same conditions of impact geometry and velocity.

In general, the agreement between the experimental and analytical results is good. Most of the deviation between the experimental and analytical results occurs for the near orthogonal impacts. Note from Figure 43 that the analytical and experimental results are not in good agreement near the impacted end. The experimental results on Figure 43 are for an orthogonal impact with no lateral deformation at the impacted end. The analytical profiles shown in Figure 43 were determined with a forcing function being applied at the impacted end. In order to initiate lateral motion, a component of the forcing function was applied in the lateral direction as follows:

$$F_y(t) = F_x(t) \sin \theta \qquad (95)$$

Where θ is the obliquity angle and $F_x(t)$ is the forcing function in the

93

TIME = 20 μsec

40 μsec

60 μsec

FINAL PROFILE 75 μsec

EXPERIMENTAL RESULTS 1006 fps

Figure 43. A Sequence of Analytical Profiles for Various Time-Increments with the Last Analytical Profile being Compared to the Experimental Results for Same Conditions. Impact Velocity is 1006 fps for a 6 Inch Rod.

TIME = 20 μsec

40 μsec

60 μsec

FINAL PROFILE   75 μsec

EXPERIMENTAL RESULTS   850 fps

Figure 44.   A Sequence of Analytical Profiles for Various Time Increments with the Last Analytical Profile being Compared to the Experimental Results for Impact of 850 fps.

TIME = 20 ..sec

40 ..sec

60 ..sec

FINAL PROFILE 75 ..sec

EXPERIMENTAL RESULTS 497 fps

Figure 45.   A Sequence of Analytical Profiles for Various Time Increments with the Last Analytical Profile Being Compared to the Experimental Results for Impact Velocity of 497 fps for a 6 Inch Rod.

96

TIME = 25 μsec

50 μsec

75 μsec

100 μsec

FINAL PROFILE 125 μsec

EXPERIMENTAL RESULTS 500 fps

Figure 46. A Sequence of Analytical Profiles for Various Time Increments
with the Last Analytical Profile Being Compared to the Exper-
imental Results for an Impact Velocity of 500 fps and Obli-
quity of 2 Degrees for 12 Inch Rod.

97

TIME = 25 μsec

50 μsec

75 μsec

100 μsec

FINAL PROFILE   125 μsec

EXPERIMENTAL RESULTS   374 fps

Figure 47.   A Sequence of Analytical Profiles for Various Time Incre-
ments with the Last Analytical Profile being Compared
with the Experimental Results for Impact Velocity of 374
fps and Obliquity of 2 Degrees for 12 Inch Rod.

98

Figure 48. A Sequence of Analytical Profiles for Various Time Increments with the Last Analytical Profile being Compared with the Experimental Results for Impact Velocity of 387 fps and Obliquity of 0.5 Degrees for 12 Inch Rod.

99

TIME = 50 ˊsec

75 ˊsec

100 ˊsec

125 ˊsec

FINAL PROFILE   150 ˊsec

EXPERIMENTAL RESULTS   602 fps

Figure 49.   A Sequence of Analytical Profiles for Various Time Increments with the Last Analytical Profile being Compared with the Experimental Results for Impact Velocity of 602 and Obliquity Near 2 Degrees for 18 Inch Rod.
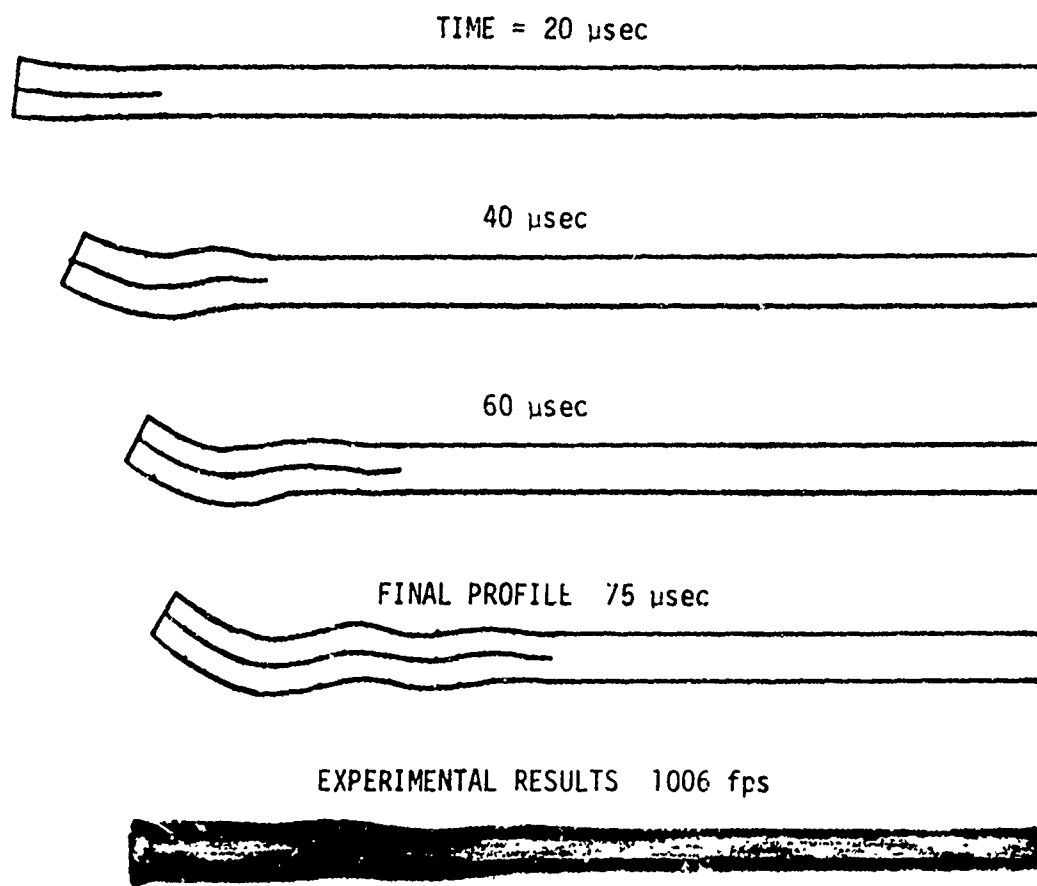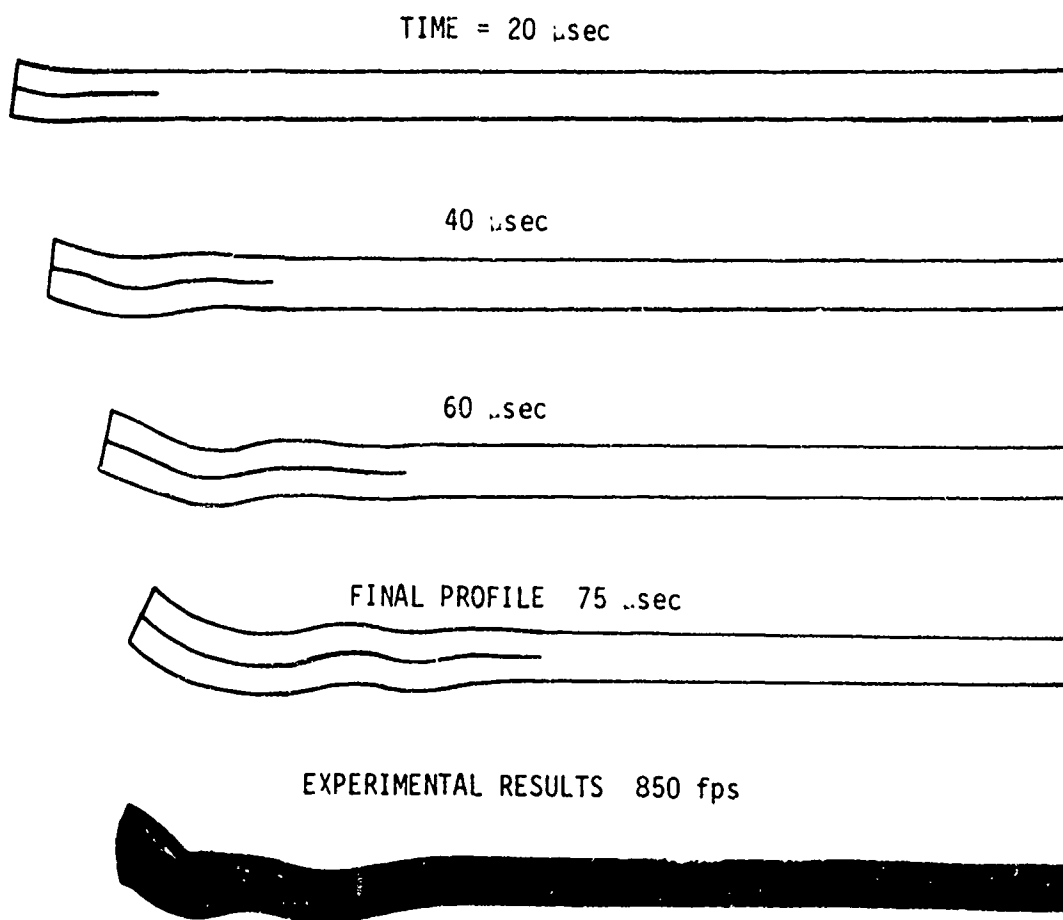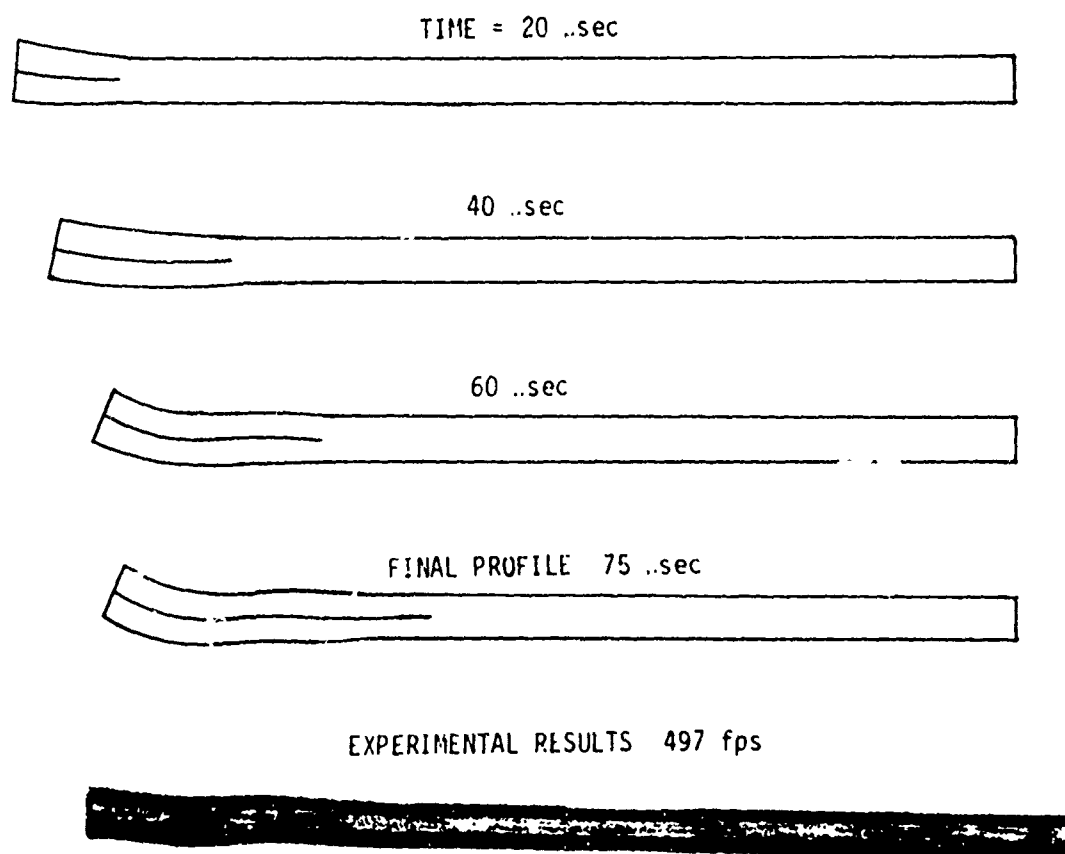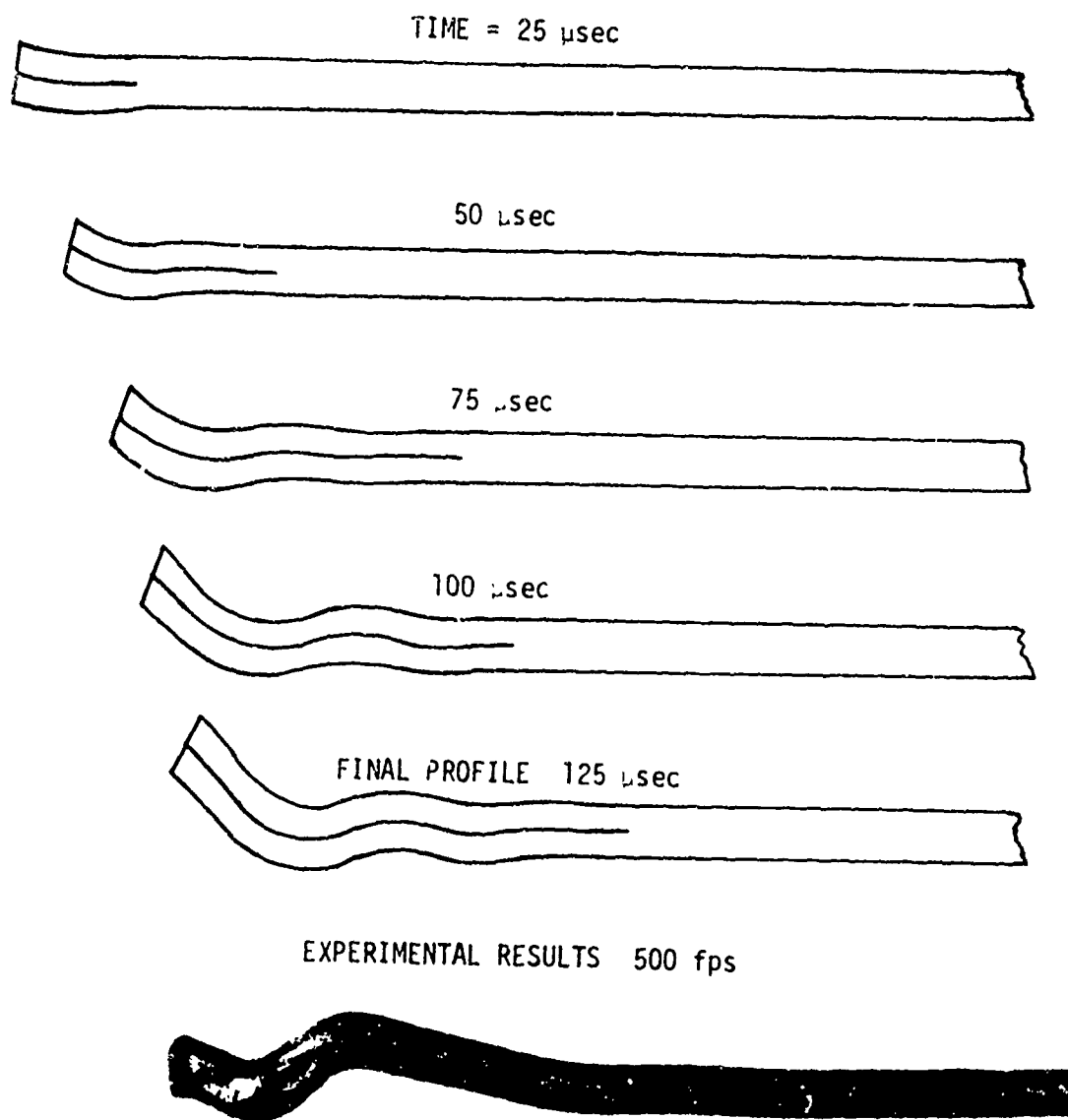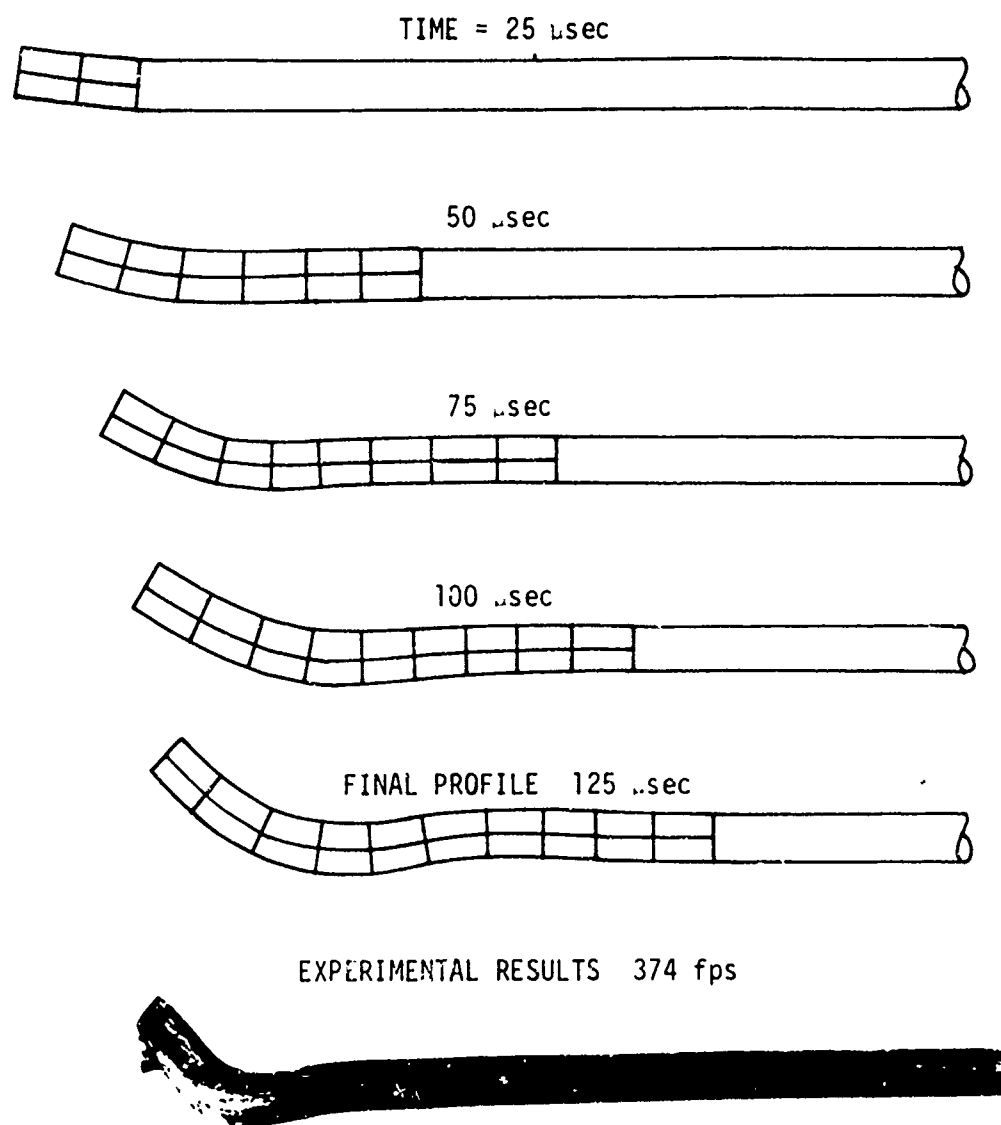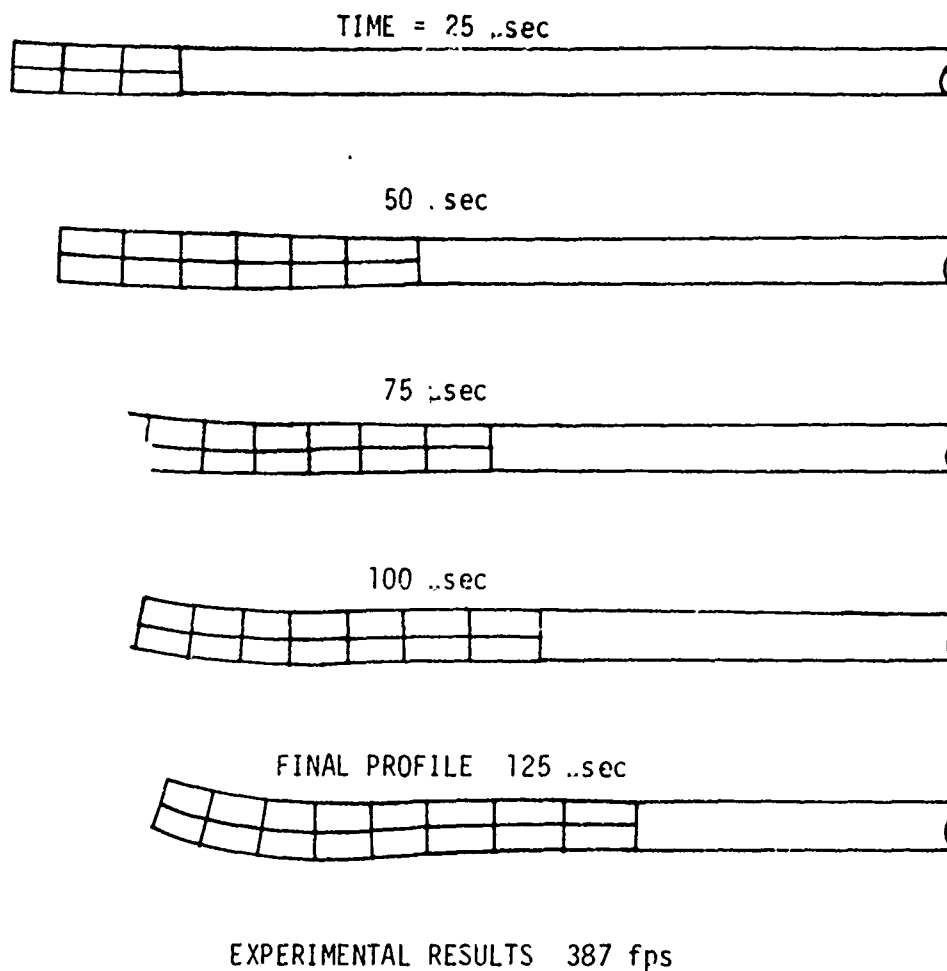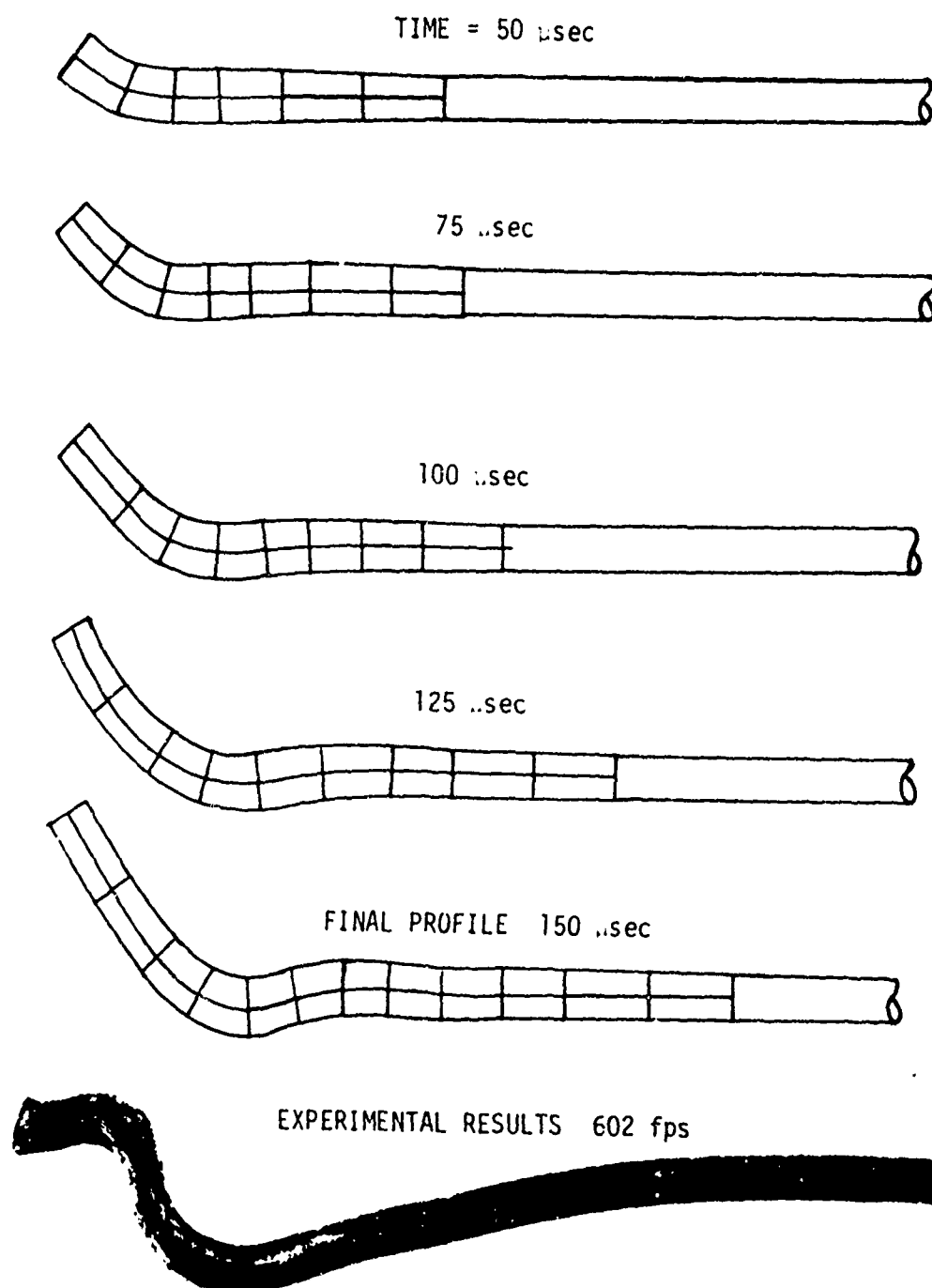
100
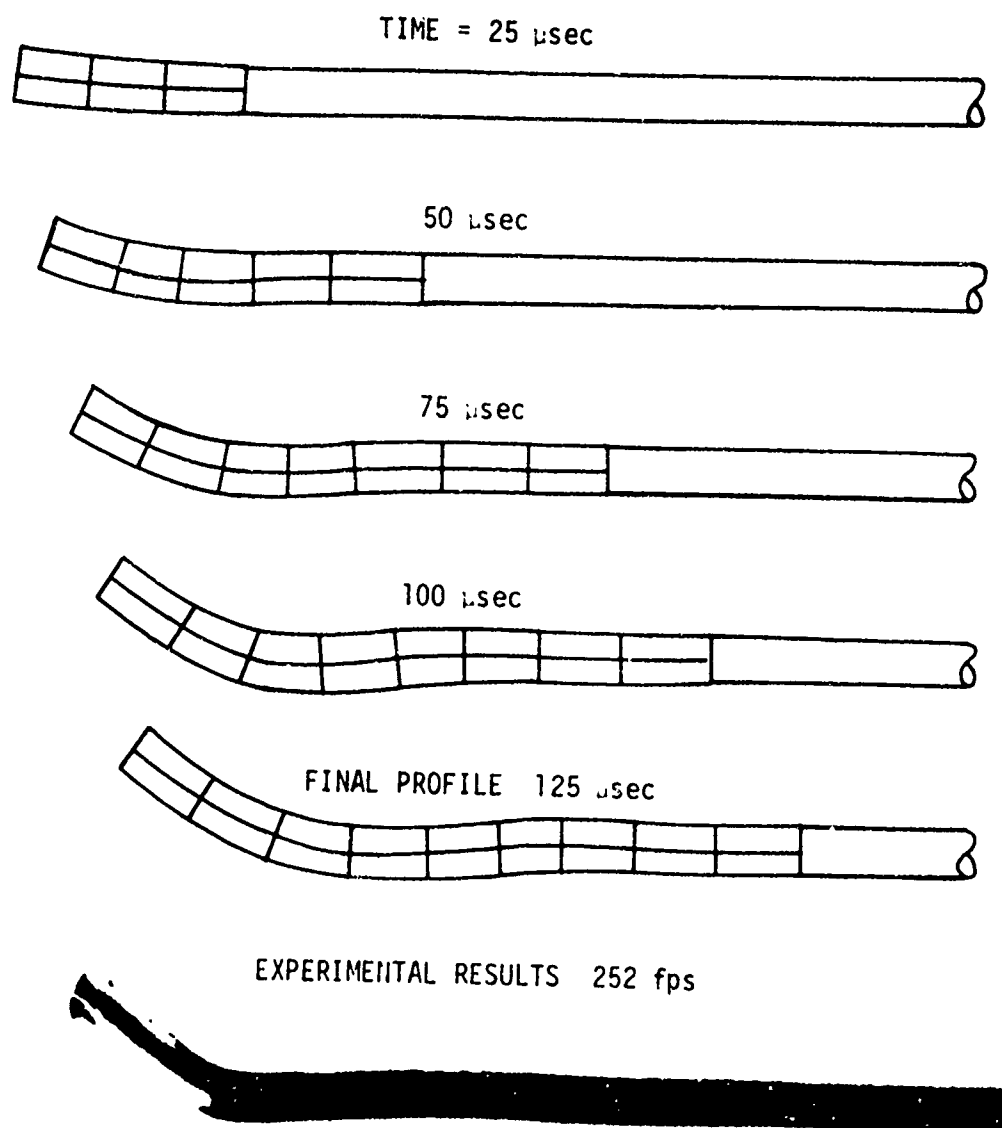
Figure 50. A Sequence of Analytical Profiles for Various Time Increments with the Last Analytical Profile being Compared with the Experimental Results for Impact Velocity of 252 fps for 18 Inch Rod at 2 Degree Obliquity.

axial direction. A small obliquity angle of 1 degree was used to initiate the lateral motion for analytical profiles (Figure 43). Except for the variance near the impacted end, agreement with the experimental results is good.

During impact, the mode shape assumed by the rod is attributed to the transverse perturbating conditions. Once a force is applied in the lateral direction, the rod is committed to failure with the magnitude of the lateral deflection being proportional to the lateral forcing function.

Figures 44 through 50 show analytical profiles for various impact conditions. These figures show that agreement with the experimental results is better near the impacted end than as shown previously in Figure 43. The agreement is attributed to the slightly oblique impact angles experienced by the rods. Some of the profiles shown do not match the experimental plastic wavelengths exactly. For the 6 inch rod impacts, the experimental wavelengths tend to be shorter than those predicted by the analysis. For example, from Figure 44 the average predicted wavelengths are about 20 percent longer than those shown by the experimental result. An attempt was made to present as many types of mode shapes as possible giving some of the profiles in good agreement as well as profiles not in good agreement. For instance, Figure 49 shows a profile where the analytical solution deviates from the experimental results near the impacted end.

Figure 51 illustrates an excellent example of the analytical and experimental results compared frame-by-frame at increments of 25 micro-seconds for a 7/16 inch rod impacting at 500 fps and at an obliquity angle of approximately 1 degree. The upper frame on Figure 51 shows the rod approximately 3 microseconds after impact. Directly below this first frame is the analytical result corresponding to the next increment of time
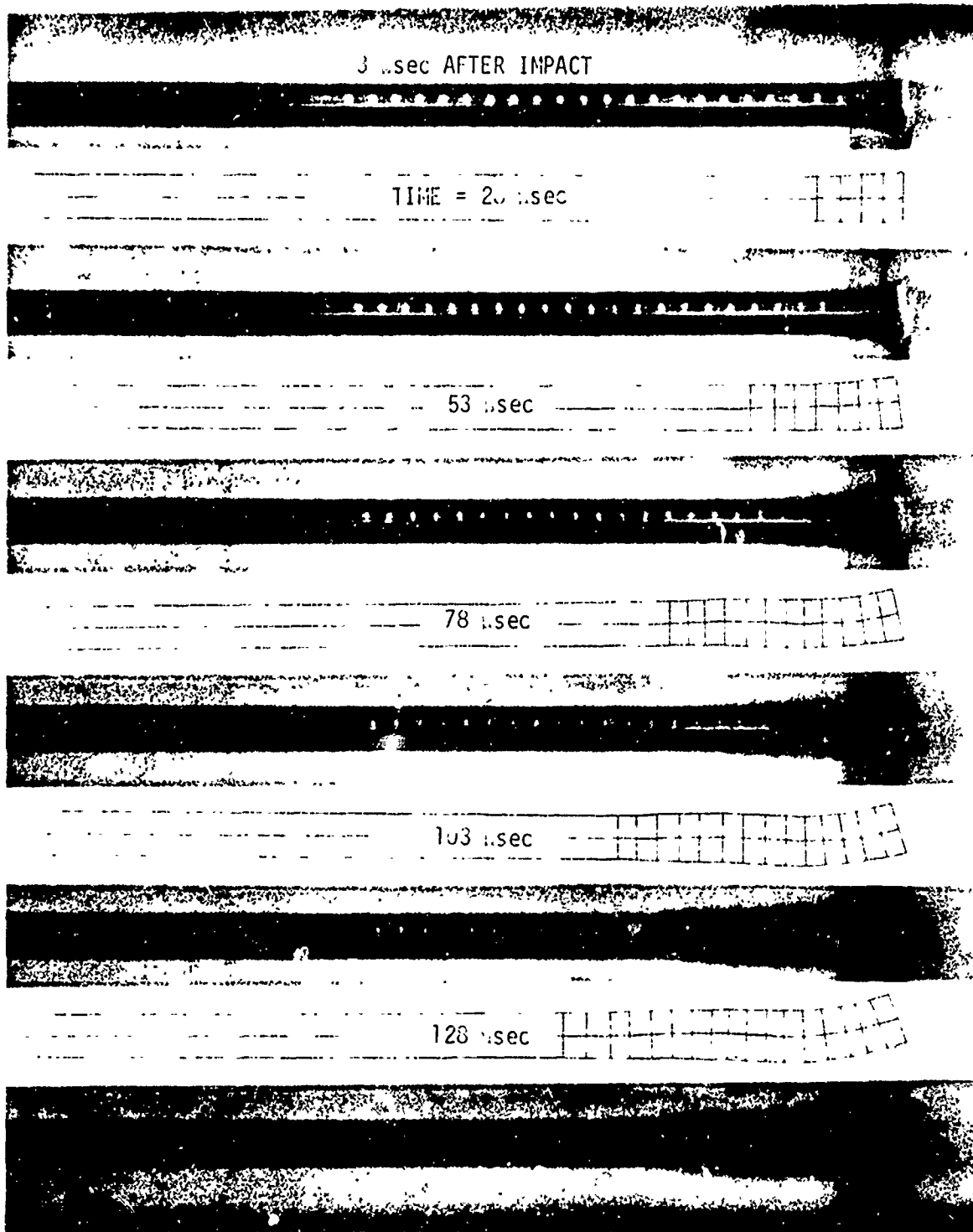
Figure 51. A Comparison of the Analytical and Experimental Results on a Frame-by-Frame Basis. Impact Velocity is Near 500 fps for 7/16 Inch Rod of 12 Inches in Length

103

some 25 microseconds later. The corresponding experimental profiles are shown directly below each appropriate analytical profile to provide a frame-by-frame comparison. Notice that the agreement between the experimental and analytical results is excellent. In the analytical profiles, cells are shown corresponding to the finite difference cells at increments of 1/4 inch. The plastic deformation of the cell is also shown in the analytical solutions, but the finite difference cells that are ahead of the plastic deformation are not shown. It is interesting to observe the plastic wave propagations for both the analytical and experimental results.

Figure 51 also shows the longitudinal plastic wave leading the flexural wave. Note the radial expansion of the rod prior to any bending. Since the camera was positioned normal to one of the axial marks scribed on the rod, the lateral displacement may be easily seen from the motion picture frames.

The analytical results are drawn to the same scale as the frames, and the following procedure was utilized in presenting the results shown on Figure 51. First the impact frames from a 16mm movie film were enlarged to the maximum extent but not to exceed an 8 by 10 inch print. Since the rod had rings machined at specified intervals, a scale could be established from the print. Thus it was determined that the print was 62% of the actual size. The analytical results were then drawn to actual size and reduced by a photo reduction process to 62% of actual size and compared to the analytical results.

6. COMPARISON OF GALERKIN AND FINITE DIFFERENCE TECHNIQUES

Comparisons will be made between the finite difference technique and the Galerkin method for final profiles with both of the techniques also being compared to the experimental results. Figures 52 through 54 show the final profiles obtained for the Galerkin and finite difference techniques along with a final profile obtained from the experimental results. One of the obvious features to observe from the Galerkin technique is the single wavelength obtained from the solution, with the single wavelength also being small in amplitude. Solutions from the finite difference technique are in better agreement with the experimental results as illustrated in Figures 52 through 54.

The single wavelength for the Galerkin technique is attributed to the assumed solution of the displacement function given as follows:

$$\gamma_k(x) = 1 - y_1\left(\frac{x}{L}\right) + y_0 \sin\left(\frac{k\pi x}{L}\right) \tag{95}$$

Other displacement functions were used with varying degrees of success but were found to predict some unacceptable displacements at the free end. As mentioned previously, the displacement function

$$\gamma_k(x) = y_0 \sin\left(\frac{2k-1}{2L}\right) \sin x\pi x \tag{96}$$

gave results that were acceptable about two diameters from the free end, but the function is a violation of the free boundary condition at the free end. The function as given by Equation (96) gives a number of wavelengths per rod and perhaps would be an acceptable displacement function for an orthogonal impact where the impacted end does not move laterally.

The Galerkin technique, as used in this work, also overpredicts the axial displacement. This fact was also observed with the finite difference

GALERKIN SOLUTION
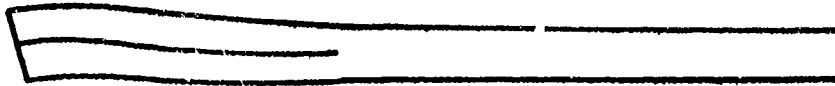
FINITE DIFFERENCE SOLUTION
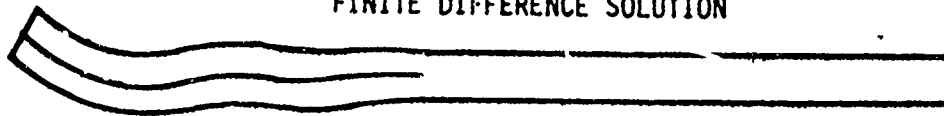
EXPERIMENTAL RESULTS   697 fps

Figure 52.   A Comparison of the Final Profiles for the Galerkin
             and Finite Difference Techniques for a 6 Inch Rod
             Having Impacted at 697 fps.

106

GALERKIN SOLUTION

FINITE DIFFERENCE SOLUTION

EXPERIMENTAL RESULTS   388 fps
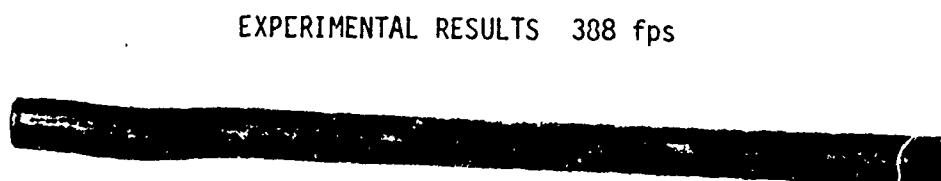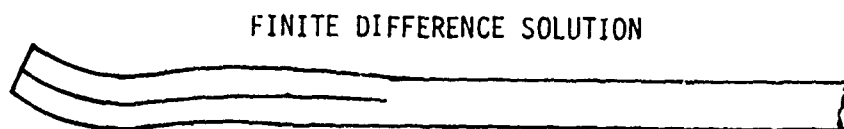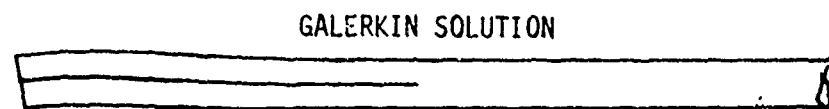
Figure 53. A Comparison of the Final Profiles Near the Impacted
            End for the Galerkin and Finite Difference Techniques
            for a 6 Inch Rod Having Impacted at 388 fps.

107

GALERKIN SOLUTION

FINITE DIFFERENCE SOLUTION
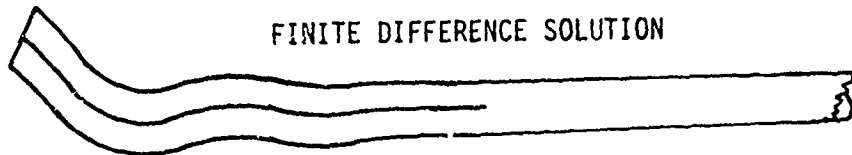
EXPERIMENTAL RESULTS   500 fps   12 INCH ROD

Figures 54.   A Comparison of the Final Profiles Near the Impacted
End for the Galerkin and Finite Difference Techniques
for a 12 Inch Rod Having Impacted at 500 fps.

108

technique, but to a lesser extent. The excessive displacement for the Galerkin technique can be attributed to the fact that the nonlinearity in geometry was not considered, i.e., the change in area along the rod due to material flow was not introduced between each discrete time interval during the solutions. While the displacements for the neutral axis was determined for small intervals of time, the rod profile was not determined until after the final displacements were computed. The "continuous" nature of the Galerkin solution in the displacement domain posed a difficult situation with regard to determining a continuous area function along the rod during the impact process. However, the discrete nodal point method of the finite difference technique allows the nonlinearity of the material properties and geometry to be determined easily. In addition, the Galerkin technique, as used in this work, applies only to a linear strain hardened material and not for an elastic-plastic material as used in the finite difference technique.

Mentioned was the fact that the finite difference technique overpredicts the axial deformation. This is true for impact velocities less than about 850 fps. But for impact velocities around 1000 fps, the method is in better agreement with the experimental results. As the impact velocity increases to greater than 1000 fps, the method tends to underpredict the axial deformation slightly. However, it should be restated that displacement and strain profiles may be predicted quite accurately by choosing the proper combinations of impact duration, forcing function, and material properties. As an example, a change in the plastic modulus β for the material gives a final length of 5.30 inches for $\beta = 120,000$ psi and a final length of 5.51 inches for $\beta = 200,000$ for a 6 inch rod of 1/4 inch diameter impacting at 388 fps.

This sensitivity to the changes in the properties of the stress-strain relation leads to interesting speculations as to the influence of a rate sensitive material. While type 6061 T-6 aluminum is insensitive, for rates up to 10^3, some of the strain rates achieved were higher. The other two variables of the problem, the impact duration and forcing function type, could be eliminated by solving the problem as a pure impact problem. Hence, a recommendation is made to this effect, thus establishing the material properties as the only controls for the sensitivity of solution.

SECTION VI

CONCLUSIONS AND RECOMMENDATIONS

1. CONCLUSIONS

The results of the experimental work have yielded the following observations:

a. The deformation mode shapes are sensitive to the impact geometry. An orthogonal impact with impact velocity greater than approximately 600 fps yields a helical mode shape. If there is a slight obliquity of 1 to 3 degrees at impact, the lateral deformation is confined to a single plane resulting in a sinusoidal mode shape. For oblique impacts on the order of 3 to 6 degrees, a spiral mode shape can occur for high length-to-diameter ratio rods and velocities greater than approximately 500 fps.

b. Ultra high speed photography is a valuable aid in studying the transient mode shapes of the impacting rods.

The analytical results achieved by using the finite difference technique have been shown to be in good agreement with the experimental results obtained in this work. The finite difference technique yielded better results than did the Galerkin technique. The Galerkin technique provided acceptable results only for the large plastic axial deformations.

It has been determined that the deflections, stresses, and strains within the impacting rod are sensitive to the forcing functions types used. In general, the trapezoid forcing function was found to give the best results for determining the deflection profiles. The parabolic forcing function yielded good results when determining the strains for high impact velocities on the order of 1000 fps.

111

As well as being sensitive to the forcing functions, the analytical solutions are sensitive to the material properties and impact durations. By a proper combination of forcing functions, impact durations, and slope of the stress-strain curve in the plastic region, results may be obtained that agree quite well with the experimental results. However, it has been found that these three combinations of parameters do not remain consistent over the entire impact velocity spectrum. This condition poses a problem in the combination.

In summary, this study has made a significant contribution for predicting the dynamic response of slender rods subjected to impulsive type loading as may occur during impact. The analytical technique developed is simple and easy to apply. A complicated coupling problem between two differential equations of motion and the material behavior has been solved by merely observing experimentally the wave propagations and then allowing the dominate equation of motion to determine the slope of the stress-strain relation. In addition, the solution presented herein greatly greatly simplifies the nonlinearity of the problem and reduces a complicated plasticity problem to an easily determined state of stress and strain.

A contribution has also been made in the experimental work presented herein. The fact that a helical mode shape was obtained for the orthogonal impact leads to interesting speculations as to why this mode shape is obtained. No previous mention of this phenomenon has been found in the literature investigated.

2. Recommendations

Two recommendations involving additional work are worthy of mentioning. The first involves determining the effect of adding transverse

112

shear in the lateral equation of motion. While the addition of shear presents no particular problem in the equations of motion, the plasticity problem will be complicated. Since the total accumulated plastic strain involves a uni-axial strain ϵ_x^p and a shear strain ϵ_{xy}^p, an equivalent plastic strain must be determined from the plastic strain increments through use of the Prandtl-Reuss relations.

The second recommendation, the one most easily solved, involves considering the problem as pure impact without using forcing functions. The plate would be included in the problem, thus giving a two-body problem with the contact boundary of the plate and rod deserving special attention. The plate could be modeled as a thin plate by using the plate equations or as a thick plate by using the equilibrium equations. To start the problem, the initial velocity of the plate would remain at zero, but at each nodal point of the rod, the initial velocity would equal the impact velocity.

REFERENCES

1. Abramson, H. N., Plass, H. J., and Ripperger, E. A., "Stress Wave Propagations in Rods and Beams," _Advances in Applied Mechanics_, Vol 5, 1958.

2. Kolsky, H., "Stress Waves in Solids," Dover Publications, 1963.

3. Abrahamson, G. R. and J. N. Goodier, "Dynamic Flexural Buckling of Rods Within an Axial Plastic Compression Wave," ASME _Journal of Applied Mechanics_, June 1966.

4. Grabarek, Chester L. and A. J. Ricchiazzi, "Long Rod Impacts on Finite Targets," Proceedings of the Army Symposium on Solid Mechanics, September 1968.

5. Wilkins, M. L., "Calculation of Elastic-Plastic Flow," Lawrence Radiation Laboratory Report UCRL-7322, Rev 1, January 24, 1969.

6. Sedgwick R. T., "Theoretical Investigation of Metallic Perforation by Kinetic Energy Projectiles," Air Force Armament Laboratory Report AFATL-TR-69-54, April 1969.

7. Sedgwick, R. T., "Theoretical Terminal Ballistic Investigation and Studies of Impact of Low and Very High Velocities," Air Force Armament Laboratory Report AFATL-TR-68-61, May 1968.

8. Bell, James F., "The Physics of Large Deformation of Crystalline Solids," Springer-Verlag, 1968.

9. Timoshenko, S. P. and Goodier, J. N., "Theory of Elasticity," McGraw-Hill, Third Edition, 1970.

BIBLIOGRAPHY

Bert, C. W., "Buckling of Slender Prismatic Rod at High Impact Velocity," *Journal of Spacecraft*, Vol 1, No. 5, May 1964.

Clifton, R. J. and S. R. Bodner, "An Analysis of Longitudinal Elastic-Plastic Pulse Propagation, " ASME *Journal of Applied Mechanics*, June 1966.

Cristescu, N.,"Dynamic Plasticity," American Elsevier, 1967.

Hanagud, S., Ross, B. and G. Sidhu, "Elastic-Plastic Impact of Plates," *Israel Journal of Technology*, Vol 7, February 1969.

Hoffman, O. and G. Sachs, "Introduction to the Theory of Plasticity for Engineers," McGraw-Hill, 1953.

Langhaar, H. L., "Energy Methods in Applied Mechanics," Wiley, 1962.

Marcal, P. V., "A Comparative Study of Numerical Methods of Elastic-Plastic Analysis, *AIAA Journal*, Vol 6, No. 1, January 1968.

Marcal, P. V., "A Stiffness Method for Elastic-Plastic Problems," *International Journal of Mechanical Sciences*, Vol 7, 1965.

Marcal, P. V. and I. P. King, "Elastic-Plastic Analysis of Two-Dimensional Stress Systems by the Finite Element Method, "*International Journal of Mechanical Sciences*, Vol 7, 1965.

Prager, William and P. G. Hodge, "Theory of Perfectly Plastic Solids," Wiley, 1951.

Raftopoulos, D. and N. Dávids, "Elastoplastic Impact on Rigid Targets," *AIAA Journal*, Vol 5, No. 12, 1967.

Recht, R. F. and I. W. Ipson, "Ballistic Perforation Dynamics," ASME *Journal of Applied Mechanics*, September 1968.

Valentine, M. B. and Whitehouse, G. D., "Transient Deformation of Slender Rods Impacting Rigid Plates," ASME Publication 71-Vibr-93, September 1971.

Zienkiewicz, O. C. and Y. K. Cheung, "The Finite Element Method in Structural and Continuum Mechanics," McGraw-Hill, 1968.

APPENDIX

The listing of the finite difference computer program utilized in solving the problem of the elastic-plastic response of a slender rod impacting a rigid plate is given in this appendix. The computer listing as given is compatible with the CDC 6600 computer at Eglin. Listed first is the main program followed by the subprograms.

117

```
      PROGRAM INTG (INPUT,OUTPUT,TAPE5=INPUT,TAPE6=OUTPUT)
C
C     FINITE DIFFERENCE METHOD FOR COMPUTING
C     LATERAL AND AXIAL DEFLECTIONS
C
C
C
      COMMON/ACON/B(4,4),THETA(4)
      COMMON/NAME/L
      COMMON/OUT/PI,AL,TMAX,OMEGA,DX,RHO,FX,FY
      DIMENSION Y(240),F(240)
      DIMENSION UX(60),S(60)
      COMMON AREA(60),AMI(60),BETA(60),R(60)
C
C     DEFINE CONSTANTS
C
      PI=3.1415926536
      G=32.1725*12.
      RHO=.0975/G
      EPSI=0.0045
C
C     INITIALIZE VARIABLES
C
      DO 9 I=1,4
    9 READ(5,10) (B(I,J),J=1,4)
      READ(5,10) (THETA(J,,J=1,4)
    2 READ(5,103)VI,TMAX,OMEGA,AL,DX,D,H,IFORCE
      DMV = PI*(D**2)*AL*VI*RHO*3.0
      H=H*1.E-06
      IF(TMAX.LT.1.0)GO TO 8
C
      L=IFIX(AL/DX)+1
C
      DO 1 J=1,L
      R(J)=D/2.
      AMI(J)=PI*(R(J)**4)/4.
      AREA(J)=PI*(R(J)**2)
      BETA(J)=1.E07
      UX(J)=0.0
    1 S(J)=0.0
C
      LL=4*L
      DO 3 J=1,LL
      F(J) = 0.0
    3 Y(J)=0.0
      WRITE(6,100)VI,TMAX,OMEGA,AL,DX
      WRITE(6,101)D,H,IFORCE
      OMEGA=OMEGA*PI/180.
      TMAX=TMAX*1.0E-06
      T=0.0
      XMAX = H
      C1 = PI*(D**2)/4.
      ICOUNT=0
      IPRINT =  5
C
```

118

```
       IF(IFORCE .NE. 0) GO TO 12
16     MM=10
       L = MM+L
       DO 17 J=1,MM
       R(J) = 20.
       AMI(J) = PI*40000.
       AREA(J) = PI*(R(J)**2)
17     BETA(J) = 4.E07
       DO 18 J= MM,L
       Y(J) = -VI*12.0
       Y(L+L+J) = Y(J)*SIN(OMEGA)
       Y(L+L+L+J) = 0.0
       Y(L+J) =0.0
       AMI(J) = PI*(D**4)/64.
       AREA(J) = PI*(D**2)/4.
       BETA(J) = 1.E07
       UX(J) =0.0
       R(J) = D/2.
18     S(J) = 0.0
       FX =0.0
       FY = 0.0
       LL = 4*L
       DO 21 J = 1,LL
21     F(J) = 0.0
       GO TO 19
12     IF (IFORCE .EQ. 3) GO TO 13
       IF (IFORCE .EQ. 1) FX=DMV/TMAX
       IF (IFORCE .EQ. 2) FX = 3.0*DMV*(T**2)/(TMAX**3)
       GO TO 14
 13    T2=TMAX/10.
       IF(T .LT. T2) GO TO 15
       FX = DMV/(0.95*TMAX)
       GO TO 14
15     FX = DMV*T/(0.095*TMAX**2)
14     FY = FX*SIN(OMEGA)
C
19     CALL RUNKUT(LL,H,T,Y,F,XMAX,IPRINT)
C
       LM1=L-1
C
       Y(1) = Y(2)
       Y(L+1) = Y(L+2) + DX*FX/(AREA(1)*BETA(1))
       Y(L+L) =Y(L+LM1)
       Y(L) = Y(L-1)
       ICOUNT=ICOUNT+1
       XMAX=XMAX+H
       IF(XMAX.GT.TMAX)GO TO 20
       UX(1)=(Y(L+2)-Y(L+1))/DX
       UX(L)=(Y(L+L)-Y(L+LM1))/DX
       DO 4 J=2,LM1
4      UX(J) = (Y(L+J+1) -Y(LM1+J))/(2.*DX)
       DO 6 J=1,L
  6 S(J)=BETA(J)*UX(J)
       DO 5 J=1,L
       IF (ABS(UX(J)) .LT. EPSI + 0.0005) GO TO 5
```

119

```
      BETA(J) = 2.0 E 05
      IF (ABS(UX(J)) .GT. EPSI .AND. ABS(UX(J)) .LT. 0.01) BETA(J)=6.E05
      AREA(J) = C1/(1.+UX(J))
      IF(IFORCE .EQ. 0 .AND. J .LE. MM) AREA(J)=PI*(R(J)**2)/(1.+UX(J))
      AREA(J)=ABS(AREA(J))
      R(J)=SQRT(AREA(J)/PI)
      AMI(J)=PI*(R(J)**4)/4.+ AREA(J) *(R(J)**2)
      S(J) = BETA(J)*UX(J) - 42500.
    5 CONTINUE
      IF(ICOUNT.EQ.IPRINT)CALL OUTPUT(T,Y,UX,S,ICOUNT)
      GO TO 12
 10   FORMAT (4F20.0)
100 FORMAT(1H1,5X,*IMPACT VELOCITY*,F10.0,
   15X,*IMPACT DURATION*,F10.0,5X,*IMPACT ANGLE*,
   2F10.2,5X,*ROD LENGTH*,F10.0,5X,*DX*,F10.6)
101 FORMAT(15X,*ROD DIAMETER*,F10.6,
   110X,*INTEGRATION STEP SIZE*,F10.7,10X,*FORCING FUNCTION*,I3//)
103 FORMAT (7F10.0,I5)
 20   CALL OUTPUT (T,Y,UX,S,ICOUNT)
      GO TO 2
 8    CONTINUE
      STOP
      END
```

```fortran
      SUBROUTINE RUNKUT(N,H,T,Y,F,XMAX,IPRINT)
      COMMON/ACON/B(4,4),THETA(4)
      DIMENSION YKEEP(240),Y(240),F(240)
      DIMENSION AK(240,4)
C
C
10    DO 16 J=1,N
16    YKEEP(J) = Y(J)
      X1 = T
      DO 15 K=1,4
      CALL DERIVY (T,Y,AK(1,K))
      DO 25 I=1,N
      SUM = 0.0
      DO 25 J=1,K
      SUM = SUM+H*B(K,J)*AK(I,J)
25    Y(I) = YKEEP(I) + SUM
15    T = X1 + THETA(K)*H
      IF (T .LT. XMAX) GO TO 10
      RETURN
      END
```

```fortran
      SUBROUTINE DERIVY(T,Y,F)
      COMMON/NAME/L
      COMMON/OUT/PI,AL,TMAX,OMEGA,DX,RHO,FX,FY
      DIMENSION A(60,60),C(60),KP(60),Y(240),F(240),Z(60)
      COMMON AREA(60),AMI(60),BETA(60),R(60)
C
C
      DO 10 I=1,L
      DO 10 J=1,L
   10 A(I,J) = 0.0
      DO 11 I=1,L
   11 C(I) = 0.0
    5 LM1=L-1
      LM2=L-2
      M=L+L+L
      LP1 =L+1
      C1=(DX*FX)/(AREA(1)*BETA(1))
      C2=RHO*(DX**2)
      F(1) =0.0
      F(1+L) = Y(1)
      F(2)=(C1-Y(2+L)+Y(3+L))*(BETA(2)/C2)
      F(2+L)=Y(2)
      DO 1 I=3,LM2
      F(I)=(Y(I-1+L)-2.*Y(I+L)+Y(I+1+L))*(BETA(I)/C2)
    1 F(I+L)=Y(I)
      F(LM1)=(BETA(LM1)/C2)*(Y(L+LM2)-Y(L+LM1))
      F(LM1+L)=Y(LM1)
      F(L) = 0.0
      F(L+L) = Y(L)
C
      A(1,1) = -C2
      A(1,2) =C2
      C(1) = -FY*(DX**3)/AMI(1)+.5*BETA(1)*(Y(1+M)-2.*Y(2+M)+Y(3+M))
      C3=-AMI(2)/(AREA(2)*(DX**2))
      A(2,1)=C3
      A(2,2)=-2.*C3+1.
      A(2,3)=C3
      C4=-(BETA(2)*AMI(2))/(RHO*AREA(2)*(DX**4))
      C(2) = C4*(-2.*Y(1+M)+5.*Y(2+M)-4.*Y(3+M)+Y(4+M))
      DO 2 I=3,LM2
      C5=AMI(I)/(AREA(I)*DX**2)
      IP1=I+1
      IM1=I-1
      A(I,IM1)=C5
      A(I,I)=-2.*C5-1.
      A(I,IP1)=C5
      C6=BETA(I)*AMI(I)/(RHO*AREA(I)*(DX**4))
    2 C(I)=C6*(Y(I-2+M)-4.*Y(IM1+M)+6.*Y(I+M)-4.*Y(IP1+M)+Y(I+2+M))
      C7=AMI(LM1)/(AREA(LM1)*(DX**2))
      A(LM1,LM2)=C7
      A(LM1,LM1)=-C7*2.-1.
      A(LM1,L) = C7
      C8=BETA(LM1)*AMI(LM1)/(RHO*AREA(LM1)*(DX**4))
      C(LM1)=C8*(Y(L-3+M)-4.*Y(LM2+M)+5.*Y(LM1+M))
      A(L,LM1) = -C2
```

122

```
A(L,L) = C2
C(L) = (-3.*Y(LM1+M) + 3.*Y(LM2+M)-Y(L-3+M))*BETA(L)
CALL REDSOL (A,Z,C,NER,KP,L,DT)
DO 4 I=1,L
F(I+L+L) = Z(I)
4 F(I+M)=Y(I+L+L)
RETURN
END
```

```fortran
      SUBROUTINE OUTPUT(T,Y,UX,S,ICOUNT)
      COMMON/NAME/L
      COMMON AREA(60),AMI(60),BETA(60),R(60)
      DIMENSION Y(240),UX(60),S(60)
C
C
      ICOUNT=0
      M=L+L+L
      WRITE (6,102)
      DO 4 I=1,L
  4   WRITE(6,101)T,I,Y(I+L),Y(I+M),UX(I),S(I),Y(I),Y(I+L+L),R(I)
 101  FORMAT (F15.6,8X,I2,5X,3F15.6,3F12.0,4X,F10.6)
 102  FORMAT(1H0,8X,*TIME*,9X,*NODE NO.*,6X,
     1*AXIAL DISP*,5X,*LATERAL DISP*,6X,*STRAIN*,
     26X,*STRESS*,4X,*AXIAL VEL *,3X,
     3*LATERAL VEL*,2X,*RADIUS*//)
      RETURN
      END
```

```
        SUBROUTINE REDSOL (A,X,C,NER,KP,N,DT)
        DIMENSION A(60,60),X(60),C(60),KP(60)
        LOGICAL RED,SOL,DET
        RED=.TRUE.
        SOL=.TRUE.
        DET=.FALSE.
        IF ( N .EQ. 1 ) GO TO 90
        GO TO 5
        ENTRY REDUCE
        RED=.TRUE.
        SOL=.FALSE.
        DET=.FALSE.
        GO TO 5
        ENTRY SOLVE
        RED=.FALSE.
        SOL=.TRUE.
        DET=.FALSE.
        GO TO 5
        ENTRY DETERM
        RED=.FALSE.
        SOL=.FALSE.
        DET=.TRUE.
    5   IF (RED.OR. DET) GO TO 6
        GO TO 60
    6   NMI=N-1
        IF(.NOT. DET) GO TO 10
        NER = 0
        DT=1.
        GO TO 15
C
C       SET KEEPER VECTOR
C
   10   DO 12 I=1,N
   12   KP(I)=I
C
C           START DO LOOP ON L, THE REDUCTION PROCESS
C
   15   DO 50 L=1,NMI
        LP1=L+1
        IMX=L
C
C   FIND ABSOLUTE VALUE OF LARGEST COEFFICIENT
C
   20   DO 21 I=LP1,N
        IF(ABS(A(IMX,L)).LT. ABS(A(I,L)))      IMX=I
   21   CONTINUE
C
   25   IF (IMX.EQ. L) GO TO 35
        J1=1
        IF(DET)   J1=L
C
C   NOW TO INTERCHANGE ROWS
C
        DO 30 J=J1,N
        DUM=A(IMX,J)
```

125

```
          A(IMX,J)=A(L,J)
   30     A(L,J) = DUM
C
          IF (.NOT. DET) GO TO 31
          DT=-DT
          GO TO 35
   31     IDUM=KP(IMX)
          KP(IMX)=KP(L)
          KP(L) = IDUM
C         TEST TO SEE IF A(I,I) =0
C
   35     IF(ABS(A(L,L)) .LT. 1.E-25) GO TO 32
          GO TO 40
   32      DO 33 I=L,N
   33     A(I,L) = 1.0E-7
C
   40     DO 50 I=LP1,N
          PI = A(I,L)/A(L,L)
          IF(.NOT. DET)  A(I,L) = PI
          DO 50 J=LP1,N
   50     A(I,J) = A(I,J)- PI*A(L,J)
          CONTINUE
C
          IF (.NOT.(DET .OR.SOL)) GO TO 901
          IF(.NOT. DET)  GO TO 60
          DO 55 I=1,N
          DT = DT * A(I,I)
          IF (ABS(DT) .LT. 1.0 E-20) GO TO 51
          GO TO 55
   51     DT= SIGN(1.0E-20,DT)
          NER=1
   55     CONTINUE
          IF(NER .EQ. 1) RETURN
          GO TO 901
C
C           SORT AND STORE C     ,
C
   60     DO 65 I=1,N
          K=KP(I)
   65     X(I)= C(K)
   66      CONTINUE
C
C         REDUCE THE VECTOR X
C
   70     DO 75 L=1,NMI
          LP1=L+1
          DO 75 J=LP1,N
   75     X(J)=X(J)-A(J,L)*X(L)
C
   76     CONTINUE
C
C     THE BACK SUBSTITUTION PROCESSS
C
          IF (A(N,N) .EQ. 0.)    A(N,N)= 1.0E-08
   80     X(N)= X(N)/A(N,N)
```

126

```
 81    DO 85 K=1,NMI
       L=N-K
       LP1=L+1
       DO 84 J=LP1,N
 84    X(L)=X(L)-A(L,J)*X(J)
 85    X(L)=X(L)/A(L,L)
       GO TO 901
901    NER=0
       RETURN
 90    X(1) = C(1)/A(1,1)
       RETURN
       END
```